Catalytic Self-Phoretic Active Colloids

Richard Archer

The department of Chemical and Biological Engineering

The University of Sheffield

A thesis submitted to the University of Sheffield for the degree of
Doctor of Philosophy

March 2017

Abstract

Active Janus colloids are nano to micron sized colloids, capable of propelling themselves through fluidic environments. Localised, asymmetric catalytic reactions on the colloidal bodies are used to decompose a dissolved 'fuel' to produce motion. Active Janus colloids have been proposed for applications in microfluidic transport. Currently active Janus colloids are restricted in their practical applications due to the randomised nature of their trajectories over time and their low yielding production methods.

This thesis is focused on active Janus colloids prepared by physical vapour deposition, which utilise hemispherically coated platinum as a catalyst to decompose aqueous hydrogen peroxide. Many theories and mathematical models have been reported and are discussed in this thesis as to the precise nature of the mechanism of motion. To contribute to this discussion, active colloids were prepared with different surface functionalities on the non-catalytic section of the Janus colloids. The results indicated that the hydrophobicity of the non-catalytic face influenced the propulsive velocity of the active colloid which informs on the relationship between the fluid and the phoretic body.

In an effort to produce active colloids with non-random, prescribed trajectories, the symmetry of the catalytically active layer was incrementally broken and found to introduce an additional angular velocity. The magnitude of angular velocity was controllable through production parameters.

An alternative, more scalable fabrication method was developed during the course of this work. A solution based fabrication method was found to successfully produce active colloids in high concentrations which were phoretically analogous to those previously fabricated.

Finally, an investigation into the effect of the active cap shape and surface coverage was conducted. Significantly, this study found that symmetrically active colloids displayed propulsive behaviour. The suggestion that asymmetry is not required for producing enhanced motion can be used to inform and simplify future fabrication methods.

Acknowledgements

Firstly, I would like give thanks to my supervisor Dr. Stephen Ebbens who has been extremely supportive throughout my PhD in providing help when it was needed as well as encouraging independence and personal development. My gratitude also extends to the Ebbens group members, Dr. Andrew Campbell who was of enormous assistance, especially in the mathematical side of the work and Dr. David Gregory who provided many useful discussions.

A special thank you goes to Dr. Daniel Wesley with whom I have spent many hours taking apart and reassembling our temperamental e-beam evaporator.

Furthermore, I would like to thank Dr. Daniel Toolan for all the advice and help he has given over the last few years and Kimberley Anderson for her support and encouragement, especially during the last few months of thesis writing.

Huge thanks goes to Jacob Lane and Emma Chandler for their help in proof reading this thesis. I would also like to thank members of my office group, Richard Hodgkinson, Dr. Samuel Darby, Dr. Lauren Platts, and Dr. Jordan Bye for all the encouragement, the useful discussions and for creating a friendly environment in which to conduct my work.

Finally, I would like to express my gratitude to my parents, Sharon and Keith Archer, without whose support I would not be here.

This work was funded by the EPSRC CAF Fellowship (EP/J002492/1)

Publications

- *"Glancing angle metal evaporation synthesis of catalytic swimming Janus colloids with well defined angular velocity"*

  Archer, RJ., Campbell, AI., & Ebbens, SJ. SOFT MATTER, 11(34), 6872-6880 2015
- *"Preparation and 3D tracking of Catalytic Swimming Devices"*

  Campbell, AI. Archer, RJ. Ebbens, SJ. JOURNAL OF VISUALIZED EXPERIMENTS 113, 2016
- *"A Pickering emulsion Emulsion Route to Swimming Active Janus colloids"*

  Archer, RJ. Parnell, AJ. Howse, JR. Ebbens, SJ. LANGMUIR. In press.

Conference presentations

- *Advances in Functional Materials, Stony Brook University, June 2015*
  - Oral presentation "Active Colloids for Enhanced Analyte Transport in Biosensors"
  - Oral presentation "Microspinners: Controlling Rotational Frequency in Self-Phoretic Janus Devices"
- *Materials Research Society, San Francisco, April 2015*
  - Oral presentation "Realising Autonomous Transport for Janus Particle Catalytic Swimming Devices to Enable Biosensing"
- *4th Annual Postgraduate Symposium on Nanotechnology, December 2014*
  - Presentation "Nanoswimmers"
  - Additional poster presentation (awarded best poster prize)

- *Sheffield Festival of Science and Engineering*
    - Outreach presentation to general public.

Poster presentations

- *University of Sheffield departmental symposium 2014*
    - Poster Presentation (awarded best poster prize)
- *Materials Research Society, San Francisco, April 2015*
    - Poster presentation Microspinners: Controlling Rotational Frequency in Self-Phoretic Janus Devices”

Chapter 1: Introduction

Chapter 2: Methods

Chapter 3: Influence of the inactive hemisphere on the velocity of active Janus colloids.

Chapter 4: Glancing angle deposition to control active layer shape

Chapter 5: Solution based synthesis of active Janus colloids

Chapter 6: Influence of the active layer shape and coverage on the motion of active Janus colloids.

Chapter 7: Conclusions and future work

Chapter 1:

Introduction

1.1 Overview

This thesis sets out to investigate the properties of self-propulsive active colloids. Presented here in chapter 1 is an introduction, designed to lay out the fundamental information on active colloids including the challenges of producing motion for small scale particles (section 1.2), what active colloids are (section 1.3), how they produce their motion (section 1.4), the motivation for studying self-propulsive active colloids (section 1.6), existing research into expanding the utility of self-propulsive active matter (section 1.7) and the synthetic procedures required to fabricate these devices (section 1.8).

1.2 Motion at low Reynolds numbers

In the discussion of active propulsion of small scale colloids it is important to discuss what is meant by propulsive motion. Small scale objects can be observed to move randomly when suspended in a fluid environment, without any input of energy from external forces.

This motion is caused by transfer of thermal energy from the environment. Thermal energy at its simplest can be considered as the average molecular kinetic energy of a system. Thermal equilibrium in a system is primarily achieved through transfer of kinetic energy via molecular collisions. The transfer of this kinetic energy with bodies of mass in contact with the media is experienced differently depending on the mass of the body. Larger sized objects require more work (energy) to accelerate as described by classical mechanics. As a consequence the kinetic energy transferred to bodies of large size produce negligible acceleration, however to bodies of small mass, collective molecular kinetic energy transfer is sufficient to measurably accelerate the body. These collisions are random therefore the direction and rate of direction change of acceleration is also random, though statistically predictable over long enough time periods, described as a stochastic process. This random movement of colloidal particles due to the thermal energy of the environment is known as

Brownian motion[1]. Propulsive motion is that which exceeds naturally occurring Brownian motion.

Secondly we consider small scale bodies in motion which experience resistance to their motion from the fluid's resistance to deformation, known as the viscous forces. The significance of the viscous force comes down simply to the size of the inertial forces of the moving mass in comparison to the viscosity of the media, mathematically given as the Reynolds number (Equation 1.1) [2]. Where R is the Reynolds number, L is the dimension of the moving object, V is the velocity of the moving object, ρ is the fluid density and μ is the dynamic fluid viscosity.

$$R = \frac{LV\rho}{\mu}$$

Equation 1.1

The dynamic viscosity of water at 20°C is approximately $1\text{x}10^{-3}$ Kg m^{-1} s^{-1}, it can therefore be easily seen that for macroscale bodies, the inertial forces (LVρ) dominate over the viscous forces (μ) giving a large Reynolds number, however for small scale bodies the Reynolds number is small and the viscous forces dominate. An important consequence of this is the resulting insignificance of momentum for small scale bodies. Unlike larger bodies of mass which continue to move through the media after acceleration by an unbalanced force, due to momentum, small bodies stop moving immediately after application of force has ended. In short this means for colloids at low Reynolds numbers, continuous force generation is needed to generate thrust. This presents an interesting problem as it therefore limits any motion driving action to non-reciprocal motions. In a system without momentum, time-reversible back and forth motions utilised by macroscale organisms in high Reynold number environments, such as the scallop, simply create opposing forces which cancel out resulting in no net motion[3].

Microorganisms which propel themselves through low Reynolds environments utilise non-time reversible actions such as asymmetrically beating cilia which give an 'effective' and 'recovery' stroke. By changing motion to maximise resistance and force produced on the effective stroke and conversely, minimising the resistance on the recovery stroke (figure 1.1a)[4] Chlamidions such as *C. reinhardtii* utilise this method for motion[5].

In contrast, *Escherichia coli* uses rotational flagella, which employs a propeller type motion using a helical tail to generate a constant force which drives the organism forward (figure 1.1b)[6].

These non-time reversible actions involve extremely intricate chemical and physical processes which at present cannot be fully replicated synthetically. There are however, several reports of utilising the existing biological mechanisms to drive artificial systems such as micron scale gears and motors, where bacteria have been selectively attached to create unbalanced forces as they swim collectively[7][8].

A number of publications have been produced using bacteria tethered to non-biological materials such as liposomes, polystyrene colloids and nanoparticles to provide thrust and produce enhanced displacement to these non-active materials[9][10][11]. The inherent problem with biological motors however is the difficulty in maintaining and controlling the populations as well as selectively binding to desired materials which currently need to be pre-decorated in specific antibodies to tether to bacterial species whose surface cannot be modified [10].

Theoretical systems which allow a connected three component body to move in a way that is not time reversible has also been described by Najafi and Golestanian [12]. In this system the three components of the body must move independently and in a periodic fashion to achieve net translational motion (figure 1.1c) which is claimed could potentially be generated by functional molecular systems such as rotaxanes [13].

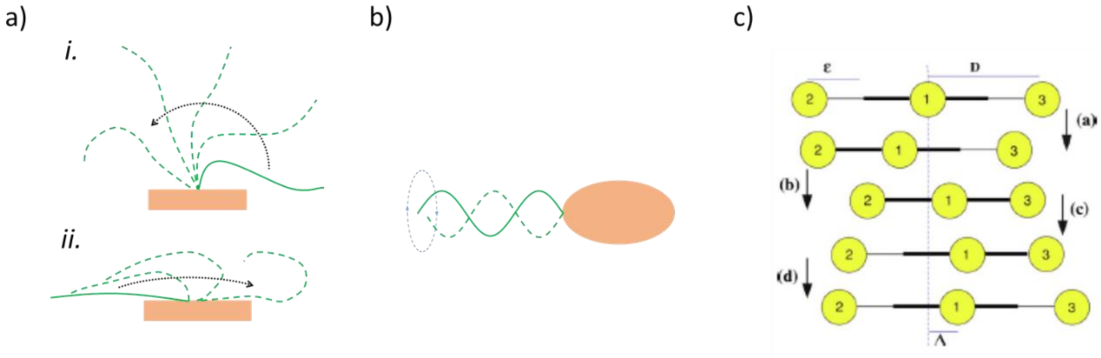

Figure 1.1 a) Cilia deformations representing i. the effective stroke and ii. the recovery stroke. b) Representation of rotating helical flagellum. c) Three body molecular swimmer undergoing a set of deformations (steps a through d) to give net motion taken from [13].

1.3 Self-motile colloids

It is a desirable goal to create synthetically produced bodies with autonomous self-phoretic motility. Several such self-phoretic colloids have been reported, all of which rely on chemical reactions to provide thrust and thus meet the requirement of non-reciprocal motion, as previously outlined, without the complexity of physical deformations required for non-reciprocal motion. To date, the most commonly utilised reaction to generate thrust is the catalytic decomposition of hydrogen peroxide.

The first reported self-motile colloid was synthesised by Paxton *et al*. in 2004 which was comprised of a bimetallic gold-platinum segmented nano-dimensioned rod and displayed enhanced motion in solutions of dilute hydrogen peroxide (2-3 wt %) to the order of 8 µms^{-1} [14]. In this system the platinum segment catalytically decomposes the hydrogen peroxide (Equation 1.2) while the gold segment is relatively inert to hydrogen peroxide, serving to break the symmetry. A full description of the relationship between such chemical reactions and motive force is described in section 1.5.

$$H_2O_2 \xrightarrow{Pt} \frac{1}{2}O_2 + H_2O$$

Equation 1.2

Since this initial report, many subsequent studies have reported similar systems relying on the catalytic decomposition of hydrogen peroxide by platinum such as the polymeric spherical colloids reported by Howse *et al.* [15].

Interestingly, for the same reaction an entirely different driving force, distinct from the aforementioned self-phoresis, can arise. When the hydrogen peroxide decomposition occurs rapidly, the local oxygen concentration reaches saturation point and nucleates into a bubble. The ejection of the bubble from the catalytic surface provides a recoil effect which generates a force in the opposing direction to the detachment[16]. With sufficient bubble generation and detachment the bubbling can provide a motive force known as ‘bubble propulsion’.

Examples of the bubble propulsion system include tubular ‘microrockets’ which consists of an interior platinum wall and an inert exterior. The dilute hydrogen peroxide solutions are decomposed within the tubular cavity and the gaseous product is ejected as a bubble which produces recoil and generates the thrust[17]. A requirement for this method is the addition of surfactant to sufficiently break the surface tension of water to allow it to penetrate the micron scale cavity of the catalytic tube.

Spherical motors with sufficient reaction rate also show bubble propulsion. An important stipulation for this appears to be the size of the active colloid. Small spherical colloids move via phoresis as the localised oxygen concentration never reaches saturation point, however for larger colloids in the order of 30 µm, the reaction rate is sufficient to cross the saturation threshold and generate bubbles[18]. In this system, as the catalyst is fully exposed to the environment containing the reactive species, no surfactant is needed.

Platinum catalyst is widely used to drive motion due to its high reactivity with hydrogen peroxide and resistance to permanent oxidation, which make it an attractive choice for academic study. However, platinum is an expensive material and as a heavy metal it is a potential environmental pollutant. As such, alternative catalyst systems have been explored.

For example, Gao *et al*. investigated the use of Janus colloids coated with an iridium catalyst to catalytically react with dissolved hydrazine, producing nitrogen, hydrogen and ammonia[19] (Equation 1.3).

$$N_2H_2 \xrightarrow{Ir} N_2 + H_2 + NH_3$$

Equation 1.3

While hydrazine itself is extremely toxic, the efficiency of the hydrazine/iridium system is reported to be 10,000 fold greater, requiring only a hydrazine content of 0.001% to display a high level phoretic motion (approximately 20 µm s^{-1}). Interestingly Gao *et al*, found that hydrazine concentrations above 0.001% became counter-productive, lowering the velocity. The authors speculate that this is due to the hydrazine increasing the pH of solution or the generation of ionic NH^{4+} species changing the ionic strength of the solution which disrupts the phoretic mechanisms discussed in greater detail later.

An alternative approach to the immobilised catalyst and dissolved fuel approach are body reactive systems. These are colloids whose bulk are comprised of chemicals which react non-catalytically with their environment. The symmetry is broken through the asymmetric deposition of an inert impermeable barrier.

Wei Gao *et al*. produced both zinc and aluminium based systems which react with acidic or both acidic and alkaline pH's respectively[20][21] (Equation 1.4, Equation 1.5, Equation 1.6). The asymmetric evolution of hydrogen gas drives the propulsion via bubble release.

$$Zn + 2H^{+} \longrightarrow H_2 + Zn^{+}$$

Equation 1.4

$$Al + 2H^{+} \longrightarrow H_2 + Al^{+}$$

Equation 1.5

$$2Al + 2OH^{-} + 2H_2O \longrightarrow 2AlO_2^{-} + 3H_2$$

Equation 1.6

To negate the necessity for extreme pH conditions to drive the reaction and the leeching of toxic Al^{+} and Zn^{+} ions, Gao *et al*. also produced magnesium based reactive colloids which operate under neutral conditions in the presence of sodium chloride[22] (Equation 1.7).

$$Mg + \ 2H_2O \ \longrightarrow Mg(OH_2) + \ H_2$$

Equation 1.7

The formation of low solubility magnesium hydroxide in pure H_2O dampens the reaction by acting as a low permeability barrier thus Gao *et al*, resolved this issue with the addition of

NaCl to the solution where the chloride anion penetrated the passivated $Mg(OH_2)$ layer through pitting corrosion and therefore facilitated the Mg dissolution and the continuation of the reaction.

While body reactive motors can offer advantages in the relatively mild environmental conditions required for operation, a major drawback is the inherent limit on the operational lifetime. Given that the reactive ‘fuel’ is depleted over time, their lifetime is therefore relative to the mass of their reactive body.

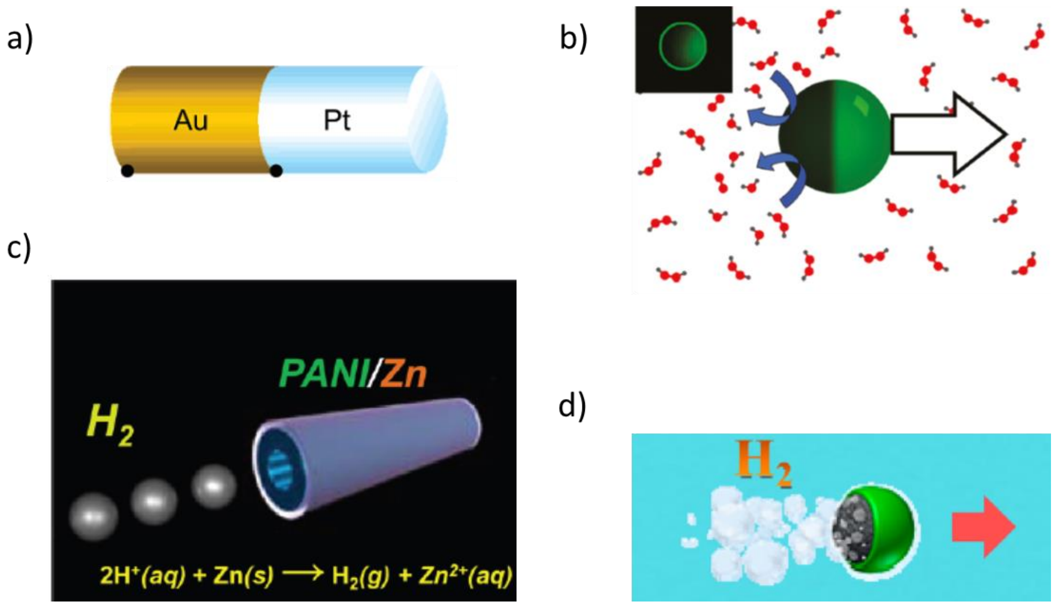

Figure 1.2 a) Bimetallic rod b) Hemispherically coated catalytic spherical colloid c) Bubble propelled microtubular ‘rocket’ d) Body reactive colloid with hemispherically coated barrier. Taken from [14][23][20][24] *respectively.*

1.4 Mechanism.

The precise mechanism of propulsion for the nanoscale self-phoresis is currently in dispute with several proposed mechanisms published and no consensus yet reached as of the date of this thesis. Developing an understanding of the phoretic mechanism is important for the future design and fabrication of active-colloids through the co-existence of mathematical modelling and experimental outcomes.

1.4.1 Surface tension

The first proposed driving mechanism for the self-generated phoresis came from Paxton *et al*. who proposed a hypothesis that for the aforementioned gold-platinum bimetallic rods a self-generated surface tension gradient across the body of the motile colloid was being generated by the production of oxygen from the decomposition of hydrogen peroxide which lowers the surface tension[14]. The asymmetric distribution of oxygen would therefore lead to an asymmetric gradient of surface tension capable of producing motion. This proposal was analogous to macroscale Marangoni powered “soap boats” which employ hydrogen bond disrupting chemicals to lower the surface tension of water at one end of the boat to produce motion by a generated surface tension gradient[25].

In support of this argument Paxton *et al*. calculated the expected velocity in relation to the volume of oxygen produced by the catalytic reaction and found the experimental velocity matched the volume of oxygen produced for the reaction rate. In addition, Paxton *et al*. found the volume fraction of ethanol in the bulk phase decreased the velocity, suggested to be due to a lowering of the surface tension differential from the colloid surface to the bulk phase.

The directionality of the bimetallic rod however was found to be problematic as the rod moved towards the catalytic, oxygen producing platinum. This is counterintuitive to the surface tension argument. As way of explanation, Paxton *et al*. suggested that the dissolved oxygen may preferentially nucleate to bubbles on the gold section. Atomic Force Microscopy (AFM) detection of nanoscale surface features, which were present only when the rod is submerged in the hydrogen peroxide solution supported this idea.

1.4.2 Nanobubbles

A proposed mechanism by Gibbs and Zhao states that the driving force for single metal, platinum coated insulators, is generated by the formation and detachment of oxygen bubbles from the catalyst surface. Through classical mechanics they state the forward thrust (F_{drive}) is generated by the recoil of a gaseous bubble detaching from the surface and that the motile particle velocity (v) is a product of the detaching bubbles mass (m), detachment velocity (v_0) and number of ejected bubbles (N) given mathematically in Equation 1.8 [16]. This theory also allows for the relation between surface tension and the motile colloid velocity due to the effect of surface tension on the bubble formation and detachment.

$$F_{drive} = N\frac{\Delta m}{\Delta t}(v_0 - v)$$

Equation 1.8

While no such bubbles have been observed by optical microscopy for many small propulsive colloids, it does not preclude the possibility of, to date, undetected nanobubble formation.

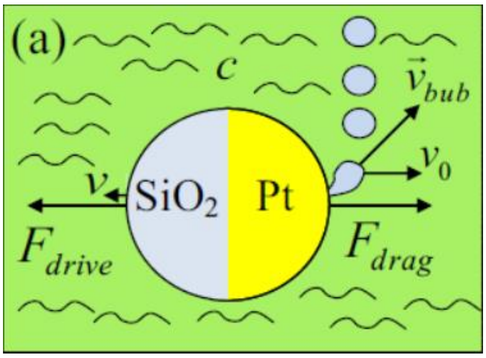

Figure 1.3. Spherical Janus colloid generating bubbles at the catalyticaly active site. The generated bubbles detatch and in doing so transfer momentum to the body.

1.4.3 Electrophoresis

After the original hypothesis of surface tension driven motion, Paxton *et al*. described an alternative theory to the motion of the bimetallic rods which would better account for the observed direction of the platinum section leading the direction. The revised theory, dubbed "electrophoresis" states that the two metals act cooperatively as redox half cells, with the platinum as the oxidation half-cell and the gold as the reduction half-cell. The resulting flow of electrons across the platinum gold junction creates a directional electric field, which in turn creates a flow of positively charged species across the surface, depicted graphically in Figure 1.4a. This flow field is suspected to be what gives the motility to the bimetallic rods[26].

In support of this Wang *et al*. created a series of bimetallic rods of different metals and predicted that the leading end of each bi-metallic rod would be the metal with the lowest redox potential (i.e the location of the oxidising half reaction). This was experimentally confirmed with the platinum metal able to both lead and trail depending on the metal it was coupled with. For example when platinum is coupled with rhodium, platinum is the trailing end due to rhodium having a lower redox potential. Importantly, Wang found that the velocity of the bimetallic rods strongly correlated to the potential difference between the two metals (Figure 1.4b). In essence stronger redox reactions produce greater electron flows and therefore generate stronger electric fields which drive the motion[27].

Moran *et al*, expanded on this description by including, not only the effects of the electric field generated by internal electron flow but also the effects of charge separation and asymmetry caused by the physical separation of the redox reactions producing a self-generated dipole in turn also creating an electric field. The electric field interacts with the charged species produced from the reaction to produce fluid motion which drives the self-electrophoresis (Figure 1.4c) [28].

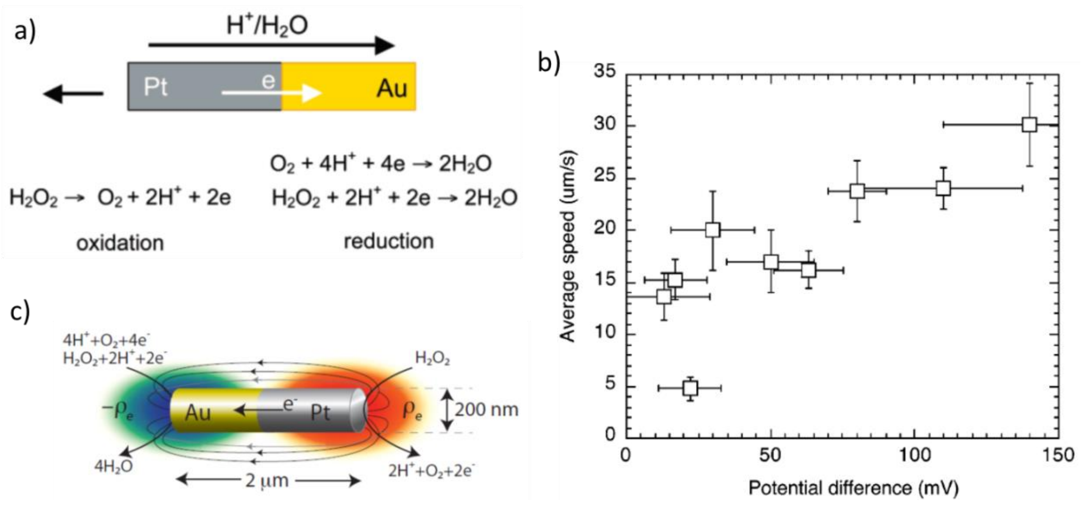

Figure 1.4 a) Redox reaction on a gold-platinum bi-metallic rod generating an internal election flow b) Potential difference vs velocity for a series of bi-metallic rods with different combinations of metals c) Spatial charge seperation on a gold-platinum bi-metallic rod giving a self-generated dipole [26][27][28].

A prevalent issue with electrophoretic motors however is their intolerance to salt. Charged ionic species are known to strongly reduce the self-phoretic motion even in low concentrations. This is thought to be primarily caused by an electric screening effect, reducing the permittivity of the solution as the conductivity increases and therefore dramatically weakening the self-generated electric field. Although the increased ionic strength is also predicted to have minor secondary effects. These effects include a small reduction in the reactivity and dampening of the charge separation potential. The combination of these factor results in high sensitivity and a dramatic loss of velocity in the presence of ionic salt species in the solution [29] . Such sensitivity to salt is a large problem to the practical use of self-electrophoretic devices in certain key applications, such as biological environments, as discussed in section 1.6 Applications.

While electrophoresis became the dominant explanation for phoretic motion in bi-metallic cells, the single metal, hemispherically coated Janus colloids offer a more challenging explanation. Initially thought as purely self-diffusiophoretic in nature, these Janus colloids also exhibit a high intolerance for salt, with associated rapid drops in velocity. Ebbens *et al.* [30]. hypothesised that the single metal Janus colloids must therefore also be primarily self-electrophoretic in nature and that the single metal cap is in fact capable of generating an electric field due to an inherent thickness gradient in the catalytic cap.

The thickness gradient occurs as an inherent attribute of Physical Vapour Deposition, which is used to synthesise asymmetrical colloids as discussed later in section 1.8 Synthesis. In physical vapour deposition the catalyst is deposited by line of sight, on the curved colloidal surface, the pole (parallel to the direction of the incoming deposition material) receives greater deposition than the sloping equator leading to a thickness maximum at the pole, gradually thinning to the equator. Coupled with the reaction rate dependency on the thickness of the catalyst, this creates an uneven reaction rate across the surface (Figure 1.5a). Since the decomposition of hydrogen peroxide by platinum involves electron transfer, the uneven reaction rate leads to an uneven electron distribution and an internal electron flow which results in a self-generated electric field. This creates the proton rich flow field in the same manner as the bi-metallic rods (Figure 1.5b) [30].

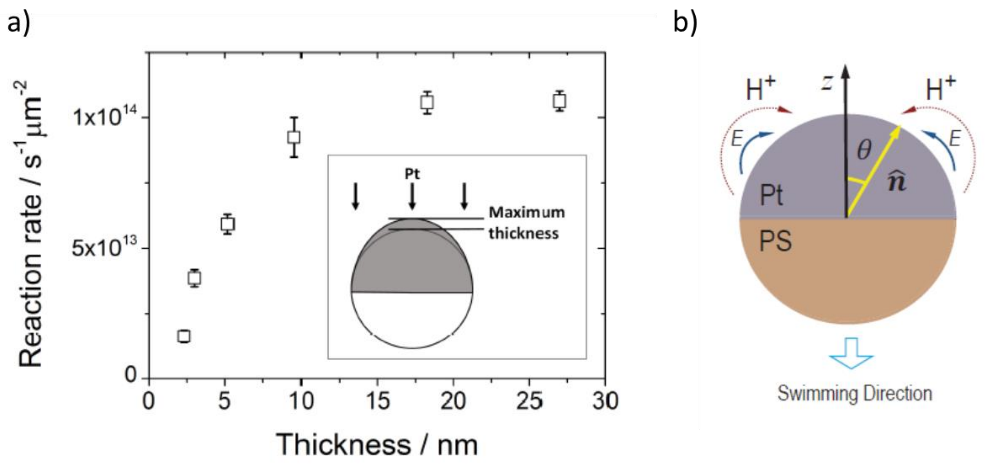

Figure 1.*5* a) Hydrogen peroxide decomposition rate dependency on the thickness of platinum. Insert shows the thickness variation of platinum deposited on a spherical colloid b) Dep*i*ction of electron flow in the catalytic hemisphere *[30]*

1.4.4 Diffusiophoresis

Another early proposal to the mechanism of phoretic motion came simply from the observation that the reactions involved in chemical powered active colloids involved producing more molecules of product than reactant. Importantly, for the diffusiophoretic model the reaction follows that of Equation 1.2 in which the products are non-charged neutral, negating the influence of any electrostatic interactions.

Many publications have been produced on describing the nature of diffusiophoresis through mathematical modelling. Typically these models can be described as either discrete colloidal interactions between a large phoretic body and many small solute products which follows as an extension of Brownian motion with asymmetry creating an imbalanced force or it can be modelled as a continuum in which hydrodynamic flow near the surface of the phoretic body causes motion[31].

Golestanian *et al*. modelled the diffusiophoretic mechanism, suggesting for an impermeable sphere with a localised reactive site, the simultaneous depletion of reactants and generation of products creates diffusion gradients across the surface of the body. In this model, as the reactants are depleted at the catalytic site, the reactants from the bulk diffuse in from the non-catalytic surface. This creates a lateral slip in the fluid across the surface of the body generating the motion (Figure 1.6). The velocity (v) is dependent on the temperature (T), the fluid viscosity (η) the radius of the colloidal body (R), the interaction range of the product (λ) and the product particle distribution around the colloidal body (P_1) Equation 1.9 [32].

$$v = -\frac{k_b T}{\eta}\frac{\lambda^2}{R}\rho_1$$

Equation 1.9

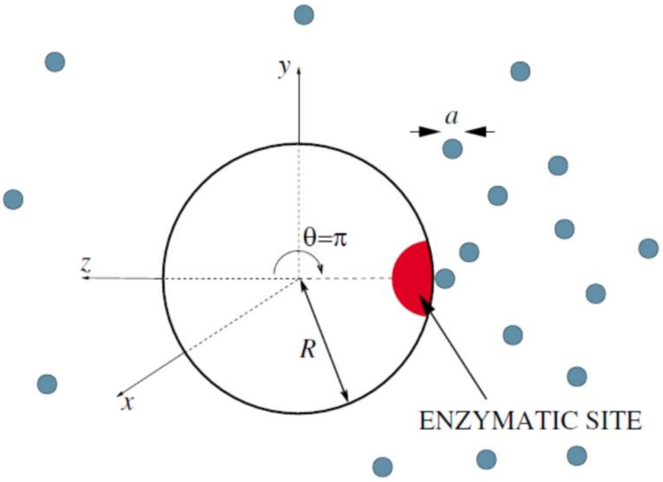

Figure 1.*6 A* simplistic model for a phoretic motor powered by assymetric generation of interacting particles *[32]*

Figueroa and Brady described a simplistic alternative model where a sphere generates particles at a localised surface site, which can be considered as the solute. The self-generated asymmetric distribution of solute particles produces an osmotic pressure (Π) (a phenomena known to apply force on semi-permeable membranes). The osmotic flow to the catalytic site applies a pressure against the impermeable body which is dependent on the number density of particles produced (n_b), and the thermal energy (kT)[33].

$$\Pi = n_b kT$$

Equation 1.10

The reliance on n_b fits with the previous reports of the higher efficiency for the hydrazine powered motors in comparison to hydrogen peroxide powered motors due to the higher number of moles produced in the decomposition of hydrazine (Equation 1.3).

Jülicher and Prost however disagreed that an osmotic force could explain the self-phoretic mechanism, arguing that it violates conservation of momentum. They described mathematically that in fact no net force would be expected over a colloidal body in a concentration gradient, self-generated or otherwise, but the colloidal body would still move relative to the fluid velocity on condition of fluid slip at the solid-liquid interface (Figure 1.7) [34].

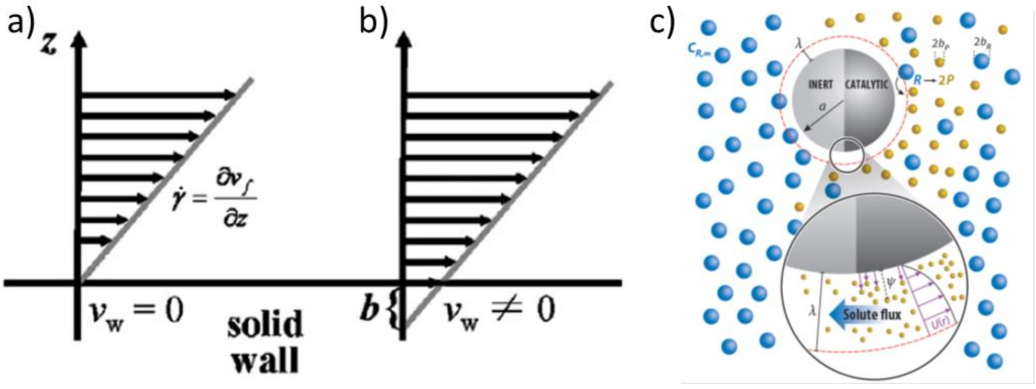

Figure 1.7 Depiction of fluid velocity at an interface for a) No slip condition where the fluid is non-mobile at the interface b) Slip condition where the fluid at the interface has a non-zero velocity c)

*D*epiction of solute moving across a spherical Janus colloid with interaction length between the body and solute of λ *[35][36].*

While the mathematical models proposed account for the diffusion of reactants, solutes and solvent, the contribution of advection, the transport of the reactants and solutes due to flow in the fluid is not considered. Fluid flow, whether considered to be the phoretic mechanism or not, is able to distort the concentration of products with respect their arrangement to the surface. Michelin and Lauga described the effects of this distortion by calculating the effects of the Péclet number, the ratio between diffusion and advection (Equation 1.11) on phoretic colloids[37].

$$Pe = \frac{Advection}{Diffusion}$$

Equation 1.11

Michelin and Lauga calculated that an increasing Péclet number would in nearly all cases have a detrimental effect on the velocity as the increasing advection decreases the concentration gradient. A notable exception however is for intermediate Péclet numbers in the case of attractive forces.

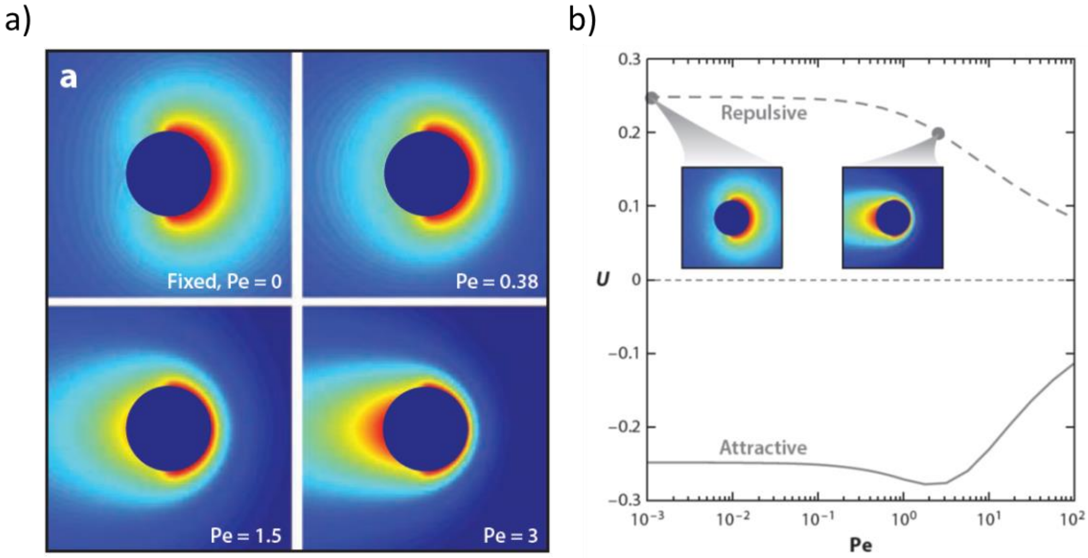

Figure 1.8 The effect of the Peclet number on the concentration field

These Péclet number models show the importance of the reaction type, specifically in the diffusion rate of the reactants and products. It is therefore suggested from this work that greater propulsion velocity can be generated by selecting reactions involving reactants and products with higher diffusivity.

1.5 Operating conditions

When considering the utility of active colloids it is important to discuss the key facets to their phoretic motion. Their velocity, fuel type, quantity dependency and environmental tolerances all inform their practical limitations regarding how they can be practically utilised.

Ebbens *et al*. described a formula for small spherical active-colloids which includes temperature (T), the bulk concentration of fuels (C_∞), the viscosity of the media (η) and the size of the colloidal body (R) (Equation 1.12) [38].

$$v \cong 0.3 \frac{k_B T \lambda_{eff}^2 C_\infty}{\eta R}$$

Equation 1.12

Ebbens *et al*. experimentally confirmed the high reliance of phoretic velocity on the size of the colloidal body to be logarithmic in nature, (Figure 1.9). While it may be initially thought that this means smaller is better, the rotational diffusion of colloids (τ_R) is also an important factor which is also inherently linked to the colloid size (R), the viscosity of the media (η) and the thermal energy ($K_B T$), which for a simple spherical active-colloid is given by Equation 1.13. The rotational diffusion time is the time taken for colloids to rotate, with smaller times representing faster turning of the colloid. This becomes an important feature given that direction of motion is related to the orientation of the colloid and therefore with lower rotational diffusion time the direction of motion changes more frequently, reducing the persistence of motion and thus the area the active colloid can explore [23]. The area in which an active colloid can explore in a given time frame subsequently becomes an interplay between velocity and rotational diffusion.

$$\tau_R = \frac{8\pi\eta R^3}{K_B T}$$

Equation 1.13

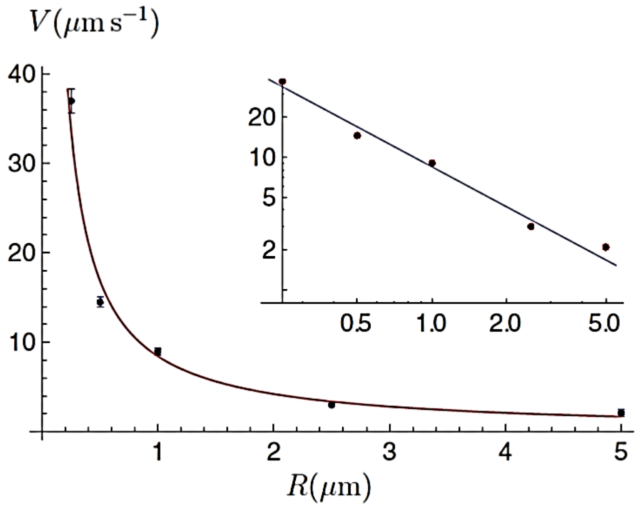

Figure 1.*9* Relationship between radius and velocity for phoretic Janus colloids powered by the decomposition of hydrogen peroxide. Insert gives logarithmic scale. *[38]*

The velocity dependency on the bulk fuel concentration (C_∞) is initially linear in nature but diminishes as the velocity plateaus. For hydrogen peroxide based fuel systems the velocity greatly varies depending on the type of active-colloid.

2μm long, bimetallic rods vary in velocity from ~ 5 to 30 μm s^{-1} at 5 wt % aqueous H_2O_2 depending on the metal composition with Nickel-Gold and Platinum-Ruthenium producing the slowest and fastest velocities respectively. The commonly reported Platinum-Gold bimetallic rods produce velocities of ~ 20 μm s^{-1}. This is in contrast to the platinum coated insulator, spherical colloids, initial reports put velocities of Janus colloids at only ~ 3.5 to 6 μm s^{-1} at 10 wt % aqueous H_2O_2. (Figure 1.10) [15][30][16]. However later reports have shown velocities as high as 10-12 μm s^{-1} at 10 wt % aqueous H_2O_2 for colloids of 2 μm in diameter [39].

As previously stated, phoretic motors based upon the decomposition of hydrazine show much higher efficiency with reported velocities of 20 at 0.001 wt % N_2H_2 aqueous solution

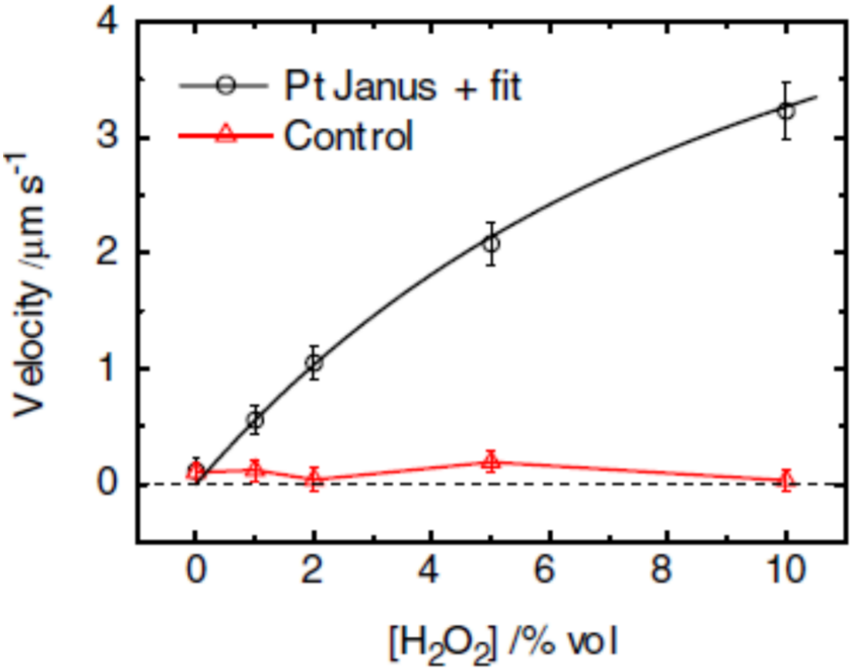

Figure 1.10 Relationship between hydrogen peroxide concentration and velocity for non-reactive colloids (red) and reactive Janus colloids (black). [15]

As discussed in section 1.4 Mechanism. It is widely reported that non-bubbling phoretic motors are sensitive to dissolved salts [30][40]. Ebbens *et al*. showed that this sensitivity is so prevalent that even at concentrations as low as 0.1 mM KNO_3, no enhanced motion is detectable (Figure 1.11a). While the exact cause of the velocity reduction due to salt species is in debate, it is shown that the velocity is inversely proportional to the conductivity of the solution (Figure 1.11b) [40].

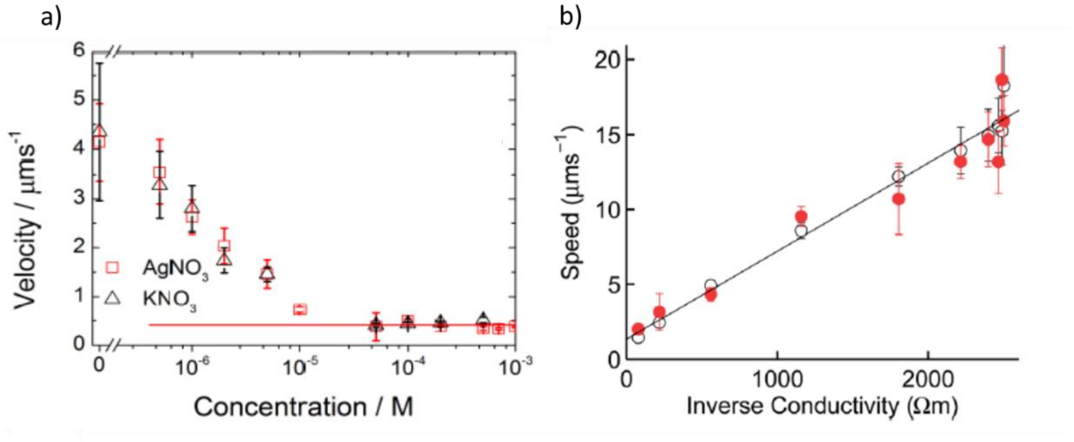

Figure 1.11 *a) Velocity dependance on dissolved salt concentration b) Velocity dependance on solution conductivity.* [30][40]

The velocity of active colloids is also sensitive to the surface tension of the media at the active colloid interface. Paxton's initial report described the inverse relationship of surface tension to velocity in the bi-metallic rods, he noted the decrease in velocity with increasing concentrations of ethanol [41]. Surface tension can also be affected by other soluble organic species including surfactants. While common ionic surfactant would be expected to play a similar role to salts, non-ionic surfactants also result in a reduction in velocity for bi-metallic rods and spherical Janus particles.

An exception to this however is the tubular micro-rockets which in fact require the surfactant as the natural surface tension of water-hydrogen peroxide is too high and prevents penetration of the bulk solution into the reactive cavity of the tube[42].

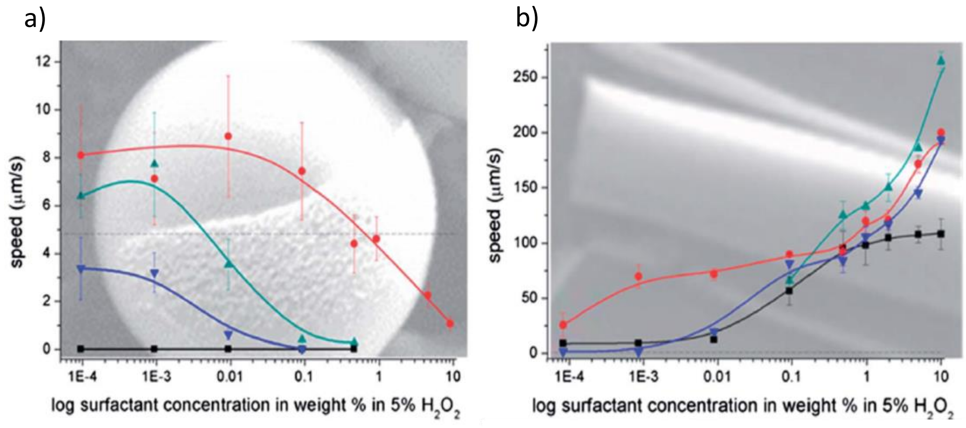

Figure 1.*12* Velocity dependance on concentration of non-ionic surfactant for a) *N*on-bubbling spherical Janus colloids b) *B*ubbling tubular micro-rocket.

1.6 Applications

It is important at this stage to discuss the applications of active colloids to understand the motivation for this work. The enhanced motion of active colloids has been proposed and demonstrated to be useful in several situations that require the autonomous interaction of colloids with the environment. Several key applications are discussed below.

1.6.1 Environmental

Several reports have been published on active colloids for the removal of oil contaminants in water. With the outside ‘inert’ surface of the colloids modified by thiolisation to be hydrophobic, they show affinity for any hydrophobic contaminants in aqueous fluid. The enhanced motion of the colloids then provides greater speed and efficiency in ‘capture’ of the contaminants which are then transported away as was first shown by bubble propelled, hydrogen peroxide reactive micro-rockets[43]. The necessity for hydrogen peroxide to be added in a system for environmental clean-up however could be seen as counter intuitive. To address this Gao *et al*. used a system which worked on the same principle of hydrophobic modified gold as the functional component, on a body reactive, magnesium based water driven motor such as those discussed in section 1.3 Self-motile colloids (Figure 1.13) [44].

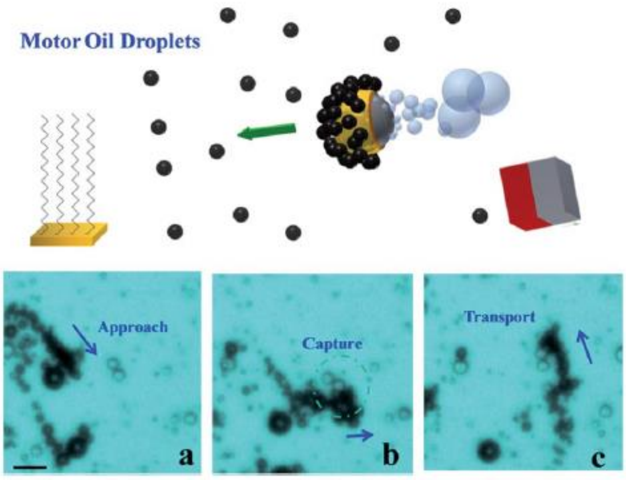

Figure 1.13 Body reactive motor with hydrophobised gold cap. Microscopy shows motors ability to 'capture' and transport hydrophobic components in an aqueous environment.

1.6.2 Cargo transport

As discussed in section 1.2, biological motile species have been examined for their ability to move and transport material in microfluidic environments. Several drawbacks of using biological motors, including the difficulty of storing stable populations, have resulted in interest in using the synthetic, active colloids to move and transport material in microfluidic environments. Non biological motors which can be chemically modified to suit the application offer a more versatile approach.

The transporting of targeted materials on the nano to micron scale by motile species is an attractive prospect which would offer the ability to work against thermodynamically driven diffusion, eventually allowing for the selective retrieval of species from multi-component systems either for purification or analysis. If used in conjunction with a method for controlling the location; accumulating to known, defined locations would allow the species to also accumulate and therefore actively concentrate a species. For example in an analytical scenario this could allow for easier detection at low solution concentrations. Efforts toward adding autonomous control to the trajectories of the colloids is an active area of research and is discussed further in section 1.7. Motion Control.

Balasubramanian *et al*. proved that the concept of tethering cells to non-biological micro-rockets is also valid, with the rockets able to selectively bind to the required cells in a multi-component system and ferry the desired targets across microfluidic channels allowing specific targeted cells to be concentrated into defined regions allowing for diagnostic testing at extremely low concentrations [45]. In addition to this Campuzano *et al*. reported the use of hydrogen peroxide powered micro-rockets for the selective binding and ferrying of of E. Coli bacterium (Figure 1.14) [46]. In this procedure Campuzano *et al*. took a further step and successfully showed the subsequent autonomous release of the bacterium in response to a chemical (low pH) signal.

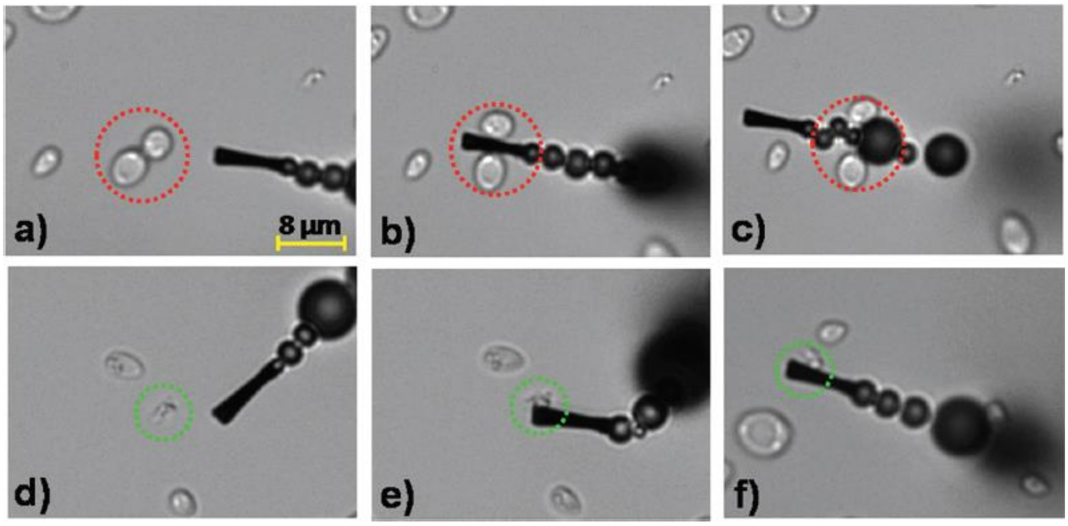

Figure 1.14: Micro-rockets decorated with lectin bioreceptor specific to E. coli. No binding occurs as the micro-rocket comes into contact with S. cerevisiae highlighted in red a-c. Conversely, binding and subsequent transport occurs as the micro-rocket comes into contact with E. Coli, highlighted in green, d-f. [46]

1.6.3 Drug delivery

The use of nanotechnology acting autonomously for *in vivo* medical purposes has long been proposed. Ma *et al*. have shown that the use of mesoporous silica for the body of Janus colloids allows for the uptake and release of molecular species [47].

While preliminary investigations have shown the nano to micron scale active colloids are themselves non-toxic[48], a major hurdle in applying current active colloids to the task of delivering drugs *in vivo* is the reliance on chemical reactions to produce motion which produce gaseous products potentially leading to air embolisms[49].

An important step towards the utility of active colloids *in vivo* circumvents the problem of gaseous production by utilising the colloids in the non-confined space of the stomach. Gao *et al*. used zinc based micro-rockets which reacted with stomach acid to produce enhanced motion by bubble propulsion. These micro-rockets were loaded with gold nanoparticles to demonstrate their ability to deliver a target material to the cells of the stomach. This was confirmed in biopsy where the concentration of gold nanoparticles in the cells of the stomach lining was significantly higher when the gold nanoparticles were delivered by the micro-rockets, as opposed to gold nanoparticles administered with no transport agent. Microscopy of the stomach lining revealed that this is likely to do with the ability of the fast moving micro-rockets to penetrate the protective mucosal membrane lining the stomach allowing greater delivery of the payload (Figure 1.15) [50].

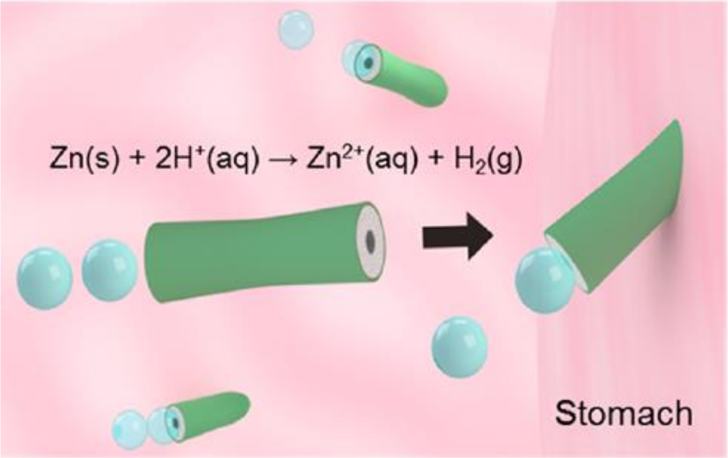

Figure 1.15 Depiction of bubble propelled zinc reactive micro-rockets embedding into the stomach lining due to their enhanced motion

1.7. Motion Control

For non-active colloids, Brownian motion causes the colloid to diffuse from its point of origin over time through random translational motion. For active colloids the propulsion is far greater than the random translational steps. For non-active colloids Brownian rotation does not need to be considered as the symmetrical surface makes orientation irrelevant. For asymmetrical surfaces the orientation becomes important.

Ebbens *et al*. directly observed the motion of active colloids is relative to the catalytically active region, with propulsion produced away from the active site[23]. For active colloids, Brownian rotation turns the colloid orientation randomly over time and therefore randomising the colloid trajectory with it. This inherent random rotation subsequently severely limits any potential applications which are locality dependant such as for mass transport or drug delivery as is discussed in section 1.6. A variety of solutions have been published in order to bias their motion in order to facilitate useful function, some key examples are discussed below.

1.7.1 Boundary.

One example of reducing the randomisation and producing a longer lasting directionality in the trajectories of active colloids exploits an interesting phenomena where self-motile devices interact with their physical environment. Das *et al*. showed that active Janus colloids at the liquid solid phase boundary have a far greater persistence in the direction parallel to the solid boundary[51]. It was hypothesised that this was due to a quenching in the Brownian rotation perpendicular to the boundary restricting the rotational freedom as depicted in Figure 1.16. Further to this they predicted that a grooved track with dimensions of width and depth only slightly larger than the diameter of the active colloid would allow the phase boundary to encompass the body and quench rotation in all directions while still allowing a translational vectoral thrust, in effect creating a rail system within which the confined enhanced displacement could occur while enabling predictable motion.

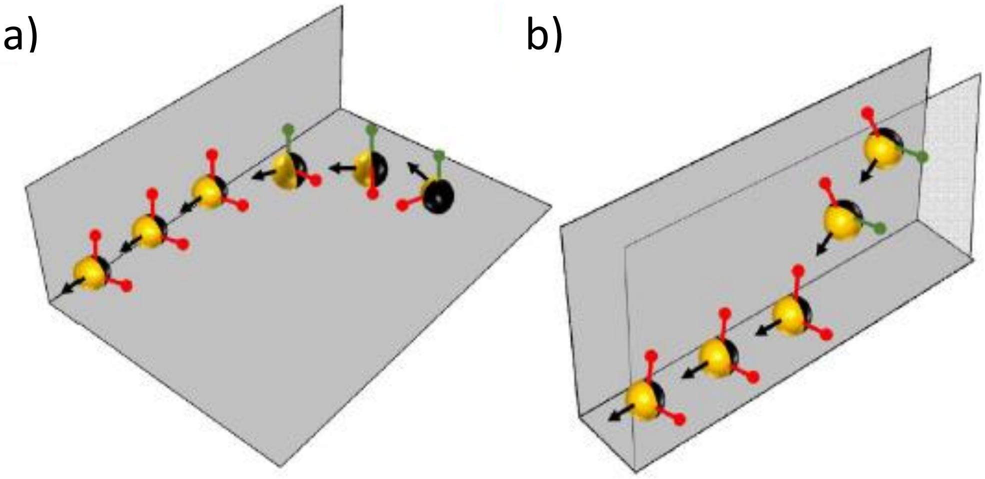

Figure 1.16 free degrees of motion (green arrow) are diminished as the phoretic colloid interacts with a second interface b) three interfaces quench all but one degrees of freedom, locking the colloid in to a set trajectory. Taken from [51]

In a similar vein, boundaries can be used to steer micro rocket devices by simple shape. Perez *et al*. showed that a heart shaped cell designed to maximise rocket deflection into a singular point, caused micro rockets to autonomously accumulate at the apex of the heart where they cannot turn or escape once entered[52].

1.7.2 Magnetic field

Quenching of Brownian rotation to reduce the randomisation of active colloid trajectories has also been shown to occur through application of weak magnetic fields on magnetically responsive materials.

Kline *et al*. have shown this by depositing a magnetically responsive nickel section into the phoretic metallic rods, to create a three component system, which then orientate themselves with a uniform, directional magnetic field produced from Helmholtz coils[53]. The rotational lock allowed not only for persistence of direction but also directed manipulation of direction through control of the magnetic field orientation. This is demonstrated in Figure 1.17 where the phoretic rods are directed to trace out “PSU” under magnetic manipulation of their trajectories.

While such high level of control may be desirable, the implementation of magnetic fields raises the necessity for user directed control. This removes the appeal of low maintenance autonomous systems.

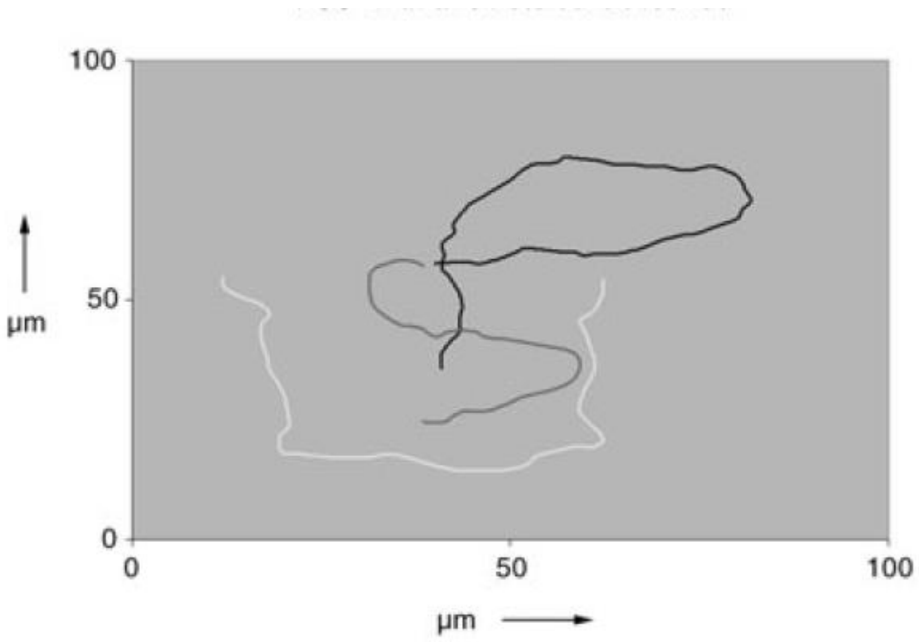

Figure 1.17 Three trajectory traces of magnetically steered active colloids, directed by manipulatiion of magnetic fields to trace out “P” ”S” and “U”, top to bottom respectively.

1.7.3 Gravitaxis

The exploitation of naturally occurring fields to control motion is observed in nature. Bacterial and algal species such as Chlamydomonas can purposely swim against gravity to overcome natural sedimentation. Such motion directed by gravity is known as gravitaxis [54].

Campbell and Ebbens have reported an inherent gravitatic component to the spherical active Janus colloids which, while negligibly small for colloids around 1 micron in diameter, becomes progressively more influential with increasing diameter as the heavy platinum catalyst used in the spherical motors moves further away from the centroid of volume. The result is a change to the centre of mass from the geometric centre as a function of the radius [55]. When the geometric and mass centre are spatially separated the colloids align themselves with the field of gravity and provides an energy barrier proportional to the degree of separation between the mass and volume centre, against Brownian rotation which biases the platinum cap towards facing down. Importantly, the downward facing cap then generates a vectoral thrust against gravity through the chemical decomposition of hydrogen peroxide and results in motion against the direction of gravity, dubbed ‘negative gravitaxis’. Figure 1.18 depicts the effects of the gravitactic directional biasing for colloids of 0.95, 1.55 and 2.4 µm diameter.

While such inherent effects bias motion without the input of external energy and requires no specialist equipment, the field of gravity cannot be changed, nor can the centre of gravity be dynamically changed and therefore this provides one set route of motion which limits the range of their potential applications.

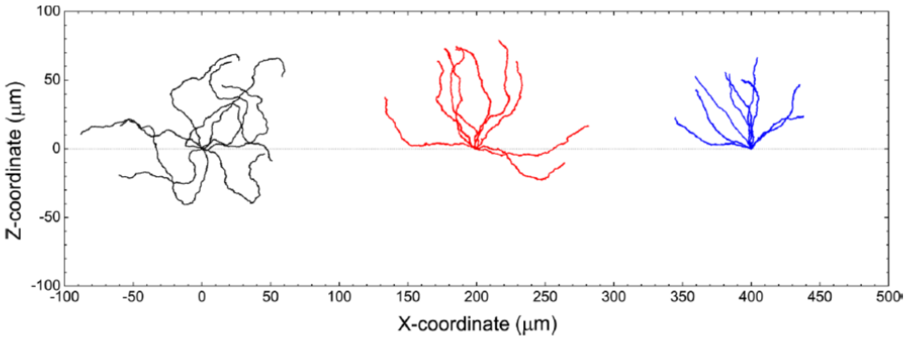

Figure 1.18 Trajectory bias in the z axis for 0.95 µm (black), 1.55 µm (red), 2.4 µm (blue) diameter colloids.[55]

1.7.4 Chemotaxis

Chemotaxis is the motion of a body in relation to a chemical gradient. It is a well reported phenomena as it is extensively employed by biological organisms to navigate their environment in which they can change from running to tumbling behaviour in response to chemical stimuli, which changes their direction persistence and therefore their displacement, allowing a longer dwell time in favoured environments[56].

Such a response to environmental conditions could prove to be useful for autonomous functionality.

It has been reported by Hong *et al*. that without modification, self-phoretic bimetallic rods are inherently chemotactic in nature with their motion biased to moving towards higher concentrations of hydrogen peroxide[57]. This was experimentally shown by introducing a gel soaked in high concentrations of aqueous hydrogen peroxide to a solution of low concentration aqueous hydrogen peroxide. A concentration gradient is established as the hydrogen peroxide diffuses from the gel to bulk solution. The average distance of self-phoretic bimetallic rods to the surface of gel diminished over time (up to 110 hours) showing a net migration of the phoretic motors towards the hydrogen peroxide gradient (Figure 1.19).

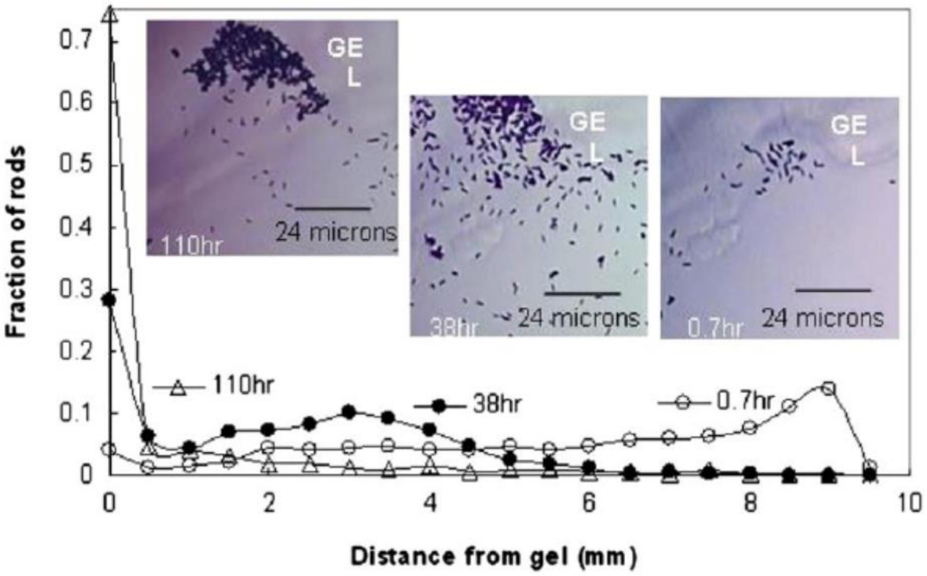

Figure 1.19 Accumulation of phoretic rods towards a hydrogen peroxide gradient at a gel interface at 0.7, 38 and 110 hours [57].

1.8 Synthesis

There are a large variety of synthetic methods published for the synthesis of Janus colloids based on polymers or chemical surface modification such as co-jetting, microfluidics preparations, Pickering emulsions and phase separation[58][59][60][61].

Currently however, most active Janus particles are based on metallic active sites and as a result the synthetic techniques revolve around the ability to pattern metal on to surfaces. One of the most common methods to achieve this is physical vapour deposition (PVD), where a metal is evaporated by an energy source in a high vacuum environment due to its highly directional coatings which allows greater control over patterning.

Paxton's original bi-metallic metallic motile rods were synthesised in a procedure based on a porous sacrificial template method by Martin *et al*. [62]. Physical vapour deposition is used to lay metals on top of a template material followed by subsequent electroplating of the deposited metal to mobilise it into the pores. Once the metal is electroplated into the pores the process is repeated with an additional metal to create the secondary segment.

Once both segments have been created, the excess metals on the template surface are removed by an acid wash and finally the template is removed by a strong base wash (Figure 1.20a). The resulting rods take the diameter and shape from the template which leads to a versatility in shape and size control through selection of the template.

Spherical active colloids are also typically prepared by PVD. The hemispherical coating is made possible by the highly directional, line of sight nature of high vacuum metal coatings. This offers a single step production method with no templating or additional steps required so therefore offering a simple fabrication method, though the high energy requirement for metal evaporation remains.

Through work presented in this thesis in Chapter 4 we can also exploit this line of sight coating by shadowing colloids to change the shape of the active site to observe the resulting changes in phoretic motion[39]. Figure 1.20b shows a simplified schematic for the PVD of platinum on a colloid to create a hemispherical active site.

The tubular micro rockets are also prepared using PVD by building layers of metals on top of a photoresist which is slowly etched away. As the photoresist is etched the metals curl due to in-built strain, caused by the different thermal expansion coefficients of the metal layers or by the grain size of the different metal layers which is controlled through deposition rate. When the strain induced curling is sufficiently high the end structure is tubular with the top layer forming the inside layer and the bottom layer forming the outside diameter. Micro rockets are purposely formed with the top layer being the catalytically active site and the bottom layer being inert to restrict the reaction to the internal cavity allowing for the bubble ejection driving force[17][63] (Figure 1.20c).

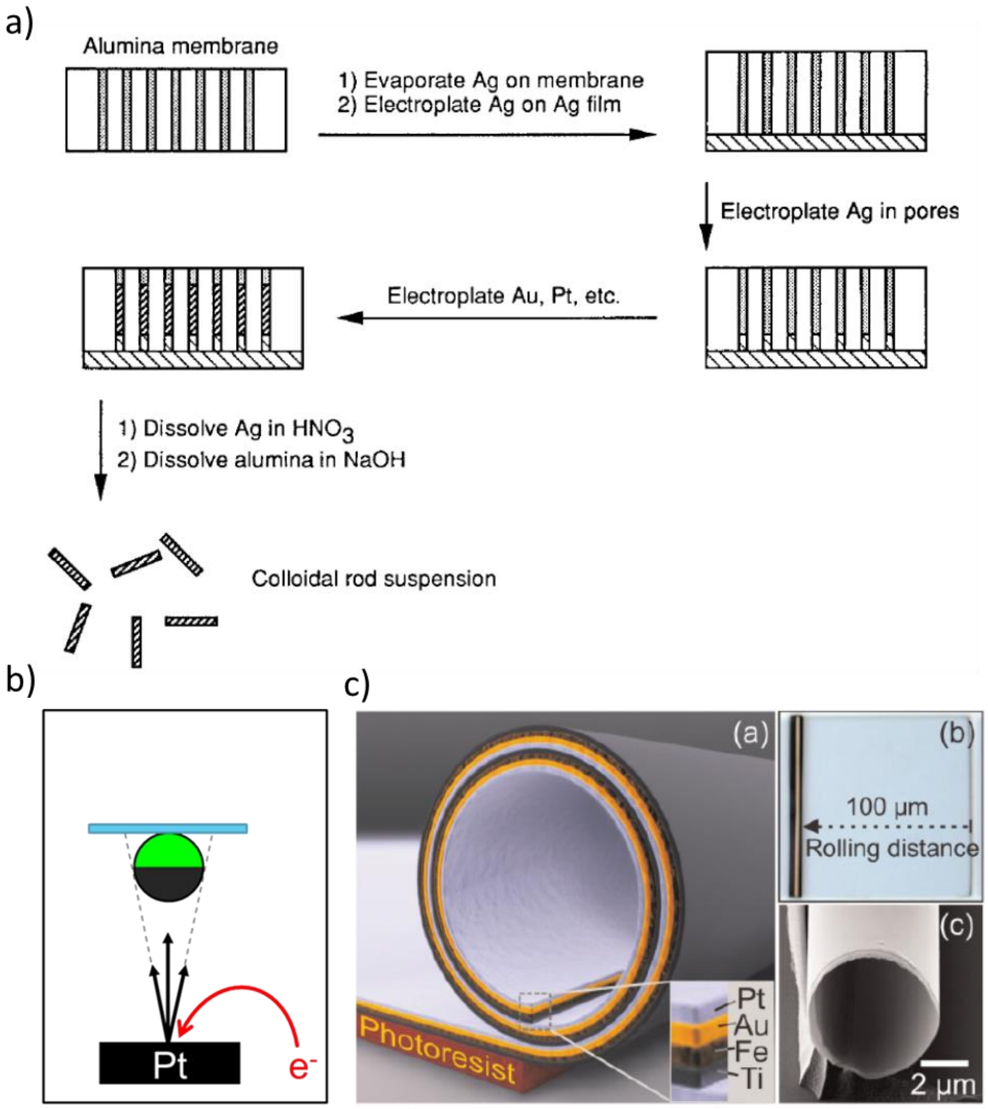

Figure 1.20 a) Schematic for fabrication of bi-metallic rods b) Schematic for fabrication of Janus colloids c) Schematic for fabrication of tubular micro-rockets.

1.9 Thesis outline

The work presented henceforth in this thesis concerns itself with spherical active Janus colloids which use the catalytic decomposition of hydrogen peroxide by surface bound platinum as discussed in section 1.3.

Chapter 2 introduces the techniques and methods which have been utilised throughout this study, providing a framework for how the work was conducted.

Chapter 3 presents results on how the hydrophobicity of the non-catalytic face of the Janus colloid influence the velocity of active motile colloids. Evidence of interaction of the non-catalytic face feeds into the discussion of the phoretic mechanisms given in section 1.4.

Chapter 4 presents results on the effect of shape of the catalytically active layer on the motion of active colloids. Through directed control of the active layer shape, the nature of the trajectories are changed. This work contributes to the study of motion control discussed in section 1.7.

Chapter 5 presents an alternative fabrication method for active Janus colloids, to the methods discussed in section 1.8. The results from this work also contribute to the current understanding of the phoretic mechanism, section 1.4.

Chapter 6 presents results on the effect of the surface coverage of the catalytically active layer. The results from this chapter also contribute to the discussion of the phoretic mechanism mentioned in section 1.4.

Finally, Chapter 7 outlines a summary of the conclusions for each experimental chapter as well as a discussion on the future work that each area of work presented could potentially lead on to further develop the field of catalytic self-phoretic active colloids.

1.10 References

[1] A. Einstein, “Investigations on the theory of the brownian movement,” *Ann. Phys.*, vol. 322, pp. 549–560, 1905.

[2] G. Taylor, “Analysis of the Swimming of Microscopic Organisms,” *Proc. R. Soc. London. Ser. A. Math. Phys. Sci.*, vol. 209, no. 1099, pp. 447 –461, 1951.

[3] E. Purcell, “Life at low reynolds number,” *Am. J. Phys.*, vol. 45, no. 1, pp. 3–11, 1977.

[4] M. a. Sleigh, “Mechanisms of flagellar propulsion,” *Protoplasma*, vol. 164, no. 1–3, pp. 45–53, Feb. 1991.

[5] D. L. Ringo, “Flagellar motion and fine structure of the flagellar apparatus in Chlamydomonas,” *Cell*, no. 21, pp. 543–571, 1967.

[6] E. M. Purcell, “The efficiency of propulsion by a rotating flagellum.,” *Proc. Natl. Acad. Sci. U. S. A.*, vol. 94, no. 21, pp. 11307–11, Oct. 1997.

[7] R. Di Leonardo, L. Angelani, D. Dell’Arciprete, G. Ruocco, V. Iebba, S. Schippa, M. P. Conte, F. Mecarini, F. De Angelis, and E. Di Fabrizio, “Bacterial ratchet motors,” *Proc. Natl. Acad. Sci.*, vol. 107, no. 21, pp. 9541–9545, 2010.

[8] A. Sokolov, M. M. Apodaca, B. a. Grzybowski, and I. S. Aranson, “Swimming bacteria power microscopic gears,” *Proc. Natl. Acad. Sci.*, vol. 107, no. 3, pp. 969–974, 2010.

[9] N. Dogra, H. Izadi, and T. K. Vanderlick, “Micro-motors: A motile bacteria based system for liposome cargo transport,” *Sci. Rep.*, vol. 6, no. October 2015, p. 29369, 2016.

[10] R. Fernandes, M. Zuniga, F. R. Sassine, M. Karakoy, and D. H. Gracias, “Enabling cargo-carrying bacteria via surface attachment and triggered release,” *Small*, vol. 7, no. 5, pp. 588–592, 2011.

[11] D. Akin, J. Sturgis, K. Ragheb, D. Sherman, K. Burkholder, J. P. Robinson, a K. Bhunia, S. Mohammed, and R. Bashir, “Bacteria-mediated delivery of nanoparticles and cargo into cells,” *Nat. Nanotechnol.*, vol. 2, no. 7, pp. 441–449, 2007.

[12] A. Najafi and R. Golestanian, “Simple swimmer at low Reynolds number: Three linked spheres,” vol. 062901, no. February, pp. 3–6, 2004.

[13] S. Erbas-Cakmak, D. a. Leigh, C. T. McTernan, and A. L. Nussbaumer, “Artificial Molecular Machines,” *Chem. Rev.*, vol. 115, no. 18, pp. 10081–10206, 2015.

[14] W. F. Paxton, K. C. Kistler, C. C. Olmeda, A. Sen, S. K. St Angelo, Y. Cao, T. E. Mallouk, P. E. Lammert, and V. H. Crespi, “Catalytic nanomotors: autonomous movement of striped nanorods.,” *J. Am. Chem. Soc.*, vol. 126, no. 41, pp. 13424–31, Oct. 2004.

[15] J. Howse, R. Jones, A. Ryan, T. Gough, R. Vafabakhsh, and R. Golestanian, “Self-Motile Colloidal Particles: From Directed Propulsion to Random Walk,” *Phys. Rev. Lett.*, vol. 99, no. 4, p. 048102, Jul. 2007.

[16] J. G. Gibbs and Y.-P. Zhao, “Autonomously motile catalytic nanomotors by bubble propulsion,” *Appl. Phys. Lett.*, vol. 94, no. 16, p. 163104, 2009.

[17] A. a Solovev, Y. Mei, E. Bermúdez Ureña, G. Huang, and O. G. Schmidt, “Catalytic microtubular jet engines self-propelled by accumulated gas bubbles.,” *Small*, vol. 5, no. 14, pp. 1688–92, Jul. 2009.

[18] D. a. Gregory, A. I. Campbell, and S. J. Ebbens, “The Effect of Catalyst Distribution on Spherical Bubble Swimmer Trajectories,” *J. Phys. Chem. C*, p. 150610185912009, 2015.

[19] W. Gao, A. Pei, R. Dong, and J. Wang, “Catalytic iridium-based Janus micromotors powered by ultralow levels of chemical fuels,” *J. Am. Chem. Soc.*, vol. 136, no. 6, pp. 2276–2279, 2014.

[20] W. Gao, A. Uygun, and J. Wang, “Hydrogen-bubble-propelled zinc-based microrockets in strongly acidic media,” *J. Am. Chem. Soc.*, vol. 134, no. 2, pp. 897–900, 2012.

[21] W. Gao, M. D’Agostino, V. Garcia-Gradilla, J. Orozco, and J. Wang, “Multi-fuel driven janus micromotors,” *Small*, vol. 9, no. 3, pp. 467–471, 2013.

[22] W. Gao, X. Feng, A. Pei, Y. Gu, J. Li, and J. Wang, “Seawater-driven magnesium based Janus micromotors for environmental remediation.,” *Nanoscale*, vol. 5, pp. 4696–700, 2013.

[23] S. J. Ebbens and J. R. Howse, “Direct Observation of the Direction of Motion for Spherical Catalytic Swimmers,” *Langmuir*, vol. 27, no. 20, pp. 12293–12296, 2011.

[24] W. Gao, A. Pei, and J. Wang, “Water-driven micromotors.,” *ACS Nano*, vol. 6, no. 9, pp. 8432–8, Sep. 2012.

[25] C. Renney, A. Brewer, and T. J. Mooibroek, “Easy demonstration of the marangoni effect by prolonged and directional motion: ‘Soap boat 2.0,’” *J. Chem. Educ.*, vol. 90, no. 10, pp. 1353–1357, 2013.

[26] W. F. Paxton, A. Sen, and T. E. Mallouk, “Motility of catalytic nanoparticles through self-generated forces.,” *Chemistry*, vol. 11, no. 22, pp. 6462–70, Nov. 2005.

[27] Y. Wang, R. M. Hernandez, D. J. Bartlett, J. M. Bingham, T. R. Kline, A. Sen, and T. E. Mallouk, “Bipolar electrochemical mechanism for the propulsion of catalytic nanomotors in hydrogen peroxide solutions.,” *Langmuir*, vol. 22, no. 25, pp. 10451–6, Dec. 2006.

[28] J. L. Moran, P. M. Wheat, and J. D. Posner, “Locomotion of electrocatalytic nanomotors due to reaction induced charge autoelectrophoresis,” *Phys. Rev. E - Stat. Nonlinear, Soft Matter Phys.*, vol. 81, no. 6, pp. 1–4, 2010.

[29] J. L. Moran and J. D. Posner, “Role of solution conductivity in reaction induced charge auto-electrophoresis,” *Phys. Fluids*, vol. 26, no. 4, pp. 1–33, 2014.

[30] S. Ebbens, D. A. Gregory, G. Dunderdale, J. R. Howse, Y. Ibrahim, T. B. Liverpool, and R. Golestanian, “Electrokinetic Effects in Catalytic Pt-Insulator Janus Swimmers,” pp. 1–5, 2013.

[31] J. F. Brady, “Particle motion driven by solute gradients with application to autonomous motion: continuum and colloidal perspectives,” *J. Fluid Mech.*, vol. 667, no. 2011, pp. 216–259, 2011.

[32] R. Golestanian, T. Liverpool, and A. Ajdari, “Propulsion of a Molecular Machine by Asymmetric Distribution of Reaction Products,” *Phys. Rev. Lett.*, vol. 94, no. 22, p. 220801, Jun. 2005.

[33] U. M. Córdova-Figueroa and J. F. Brady, “Osmotic propulsion: The osmotic motor,” *Phys. Rev. Lett.*, vol. 100, no. 15, pp. 1–4, 2008.

[34] F. Jülicher and J. Prost, “Generic theory of colloidal transport,” *Eur. Phys. J. E*, vol. 29, no. 1, pp. 27–36, 2009.

[35] J. S. Ellis and M. Thompson, “Slip and coupling phenomena at the liquid?solid interface,” *Phys. Chem. Chem. Phys.*, vol. 6, no. 21, p. 4928, 2004.

[36] J. L. Moran and J. D. Posner, “Phoretic Self-Propulsion,” *Annu. Rev. Fluid Mech.*, vol. 49, no. 1, pp. annurev–fluid–122414–034456, 2017.

[37] S. Michelin and E. Lauga, “Phoretic self-propulsion at finite Péclet numbers,” *J. Fluid Mech.*, vol. 747, no. 2014, pp. 572–604, 2014.

[38] S. Ebbens, M.-H. Tu, J. R. Howse, and R. Golestanian, “Size dependence of the propulsion velocity for catalytic Janus-sphere swimmers,” *Phys. Rev. E*, vol. 85, no. 2, p. 020401, Feb. 2012.

[39] R. J. Archer, A. I. Campbell, and S. Ebbens, “Glancing Angle Metal Evaporation Synthesis of Catalytic Swimming Janus Colloids with Well Defined Angular Velocity,” *Soft Matter*, vol. 11, pp. 6872–6880, 2015.

[40] A. Brown and W. Poon, “Ionic effects in self-propelled Pt-coated Janus swimmers.,” *Soft Matter*, pp. 4016–4027, 2014.

[41] W. F. Paxton, K. C. Kistler, C. C. Olmeda, A. Sen, S. K. St Angelo, Y. Cao, T. E. Mallouk, P. E. Lammert, and V. H. Crespi, “Catalytic nanomotors: autonomous movement of striped nanorods.,” *J. Am. Chem. Soc.*, vol. 126, no. 41, pp. 13424–31, Oct. 2004.

[42] J. Simmchen, V. Magdanz, S. Sanchez, S. Chokmaviroj, D. Ruiz-Molina, A. Baeza, and O. G. Schmidt, “Effect of surfactants on the performance of tubular and spherical micromotors – a comparative study,” *RSC Adv.*, vol. 4, no. 39, p. 20334, 2014.

[43] M. Guix, J. Orozco, M. Garcia, W. Gao, S. Sattayasamitsathit, A. Merkoči, A. Escarpa, and J. Wang, “Superhydrophobic alkanethiol-coated microsubmarines for effective removal of oil,” *ACS Nano*, vol. 6, no. 5, pp. 4445–4451, 2012.

[44] W. Gao, X. Feng, A. Pei, Y. Gu, J. Li, and J. Wang, “Seawater-driven magnesium based Janus micromotors for environmental remediation.,” *Nanoscale*, vol. 5, pp. 4696–700, 2013.

[45] S. Balasubramanian, D. Kagan, C.-M. J. Hu, S. Campuzano, M. J. Lobo-Castañon, N. Lim, D. Y. Kang, M. Zimmerman, L. Zhang, and J. Wang, “Micromachine-enabled capture and isolation of cancer cells in complex media.,” *Angew. Chem. Int. Ed. Engl.*, vol. 50, no. 18, pp. 4161–4, Apr. 2011.

[46] S. Campuzano, J. Orozco, D. Kagan, M. Guix, W. Gao, S. Sattayasamitsathit, J. C. Claussen, A. Merkoçi, and J. Wang, “Bacterial isolation by lectin-modified microengines,” *Nano Lett.*, vol. 12, no. 1, pp. 396–401, 2012.

[47] X. Ma, K. Hahn, and S. Sanchez, “Catalytic mesoporous janus nanomotors for active cargo delivery,” *J. Am. Chem. Soc.*, vol. 137, no. 15, pp. 4976–4979, 2015.

[48] E. L. K. Chng, G. Zhao, and M. Pumera, “Towards biocompatible nano/microscale machines: self-propelled catalytic nanomotors not exhibiting acute toxicity.,” *Nanoscale*, vol. 6, no. 4, pp. 2119–24, 2014.

[49] S. Ebbens, “A fantastic voyage?,” *Mater. Today*, vol. 15, no. 7–8, p. 294, Jul. 2012.

[50] W. Gao, R. Dong, S. Thamphiwatana, J. Li, W. Gao, L. Zhang, and J. Wang, “Artificial micromotors in the mouse’s stomach: A step toward in vivo use of synthetic motors,” *ACS Nano*, vol. 9, no. 1, pp. 117–123, 2015.

[51] S. Das, A. Garg, A. I. Campbell, J. R. Howse, A. Sen, D. Velegol, R. Golestanian, and S. J. Ebbens, “Boundaries can steer active Janus spheres,” *Nat. Commun.*, vol. 6, no. 8999, 2015.

[52] L. Restrepo-Pérez, L. Soler, C. S. Martínez-Cisneros, S. Sánchez, and O. G. Schmidt, “Trapping self-propelled micromotors with microfabricated chevron and heart-shaped chips.,” *Lab Chip*, vol. 14, no. 9, pp. 1515–8, 2014.

[53] T. R. Kline, W. F. Paxton, T. E. Mallouk, and A. Sen, “Catalytic Nanomotors: Remote-Controlled Autonomous Movement of Striped Metallic Nanorods,” *Angew. Chemie*, vol. 117, no. 5, pp. 754–756, 2005.

[54] A. M. Roberts, A. Science, L. South, and L. Se, “Mechanisms of Gravitaxis in Chlamydomonas,” no. April, pp. 78–80, 2006.

[55] A. I. Campbell and S. J. Ebbens, “Gravitaxis in spherical Janus swimming devices.,” *Langmuir*, vol. 29, no. 46, pp. 14066–73, Nov. 2013.

[56] G. H. Wadhams and J. P. Armitage, “Making sense of it all: bacterial chemotaxis.,” *Nat. Rev. Mol. Cell Biol.*, vol. 5, no. 12, pp. 1024–37, Dec. 2004.

[57] Y. Hong, N. Blackman, N. Kopp, A. Sen, and D. Velegol, “Chemotaxis of Nonbiological Colloidal Rods,” *Phys. Rev. Lett.*, vol. 99, no. 17, p. 178103, Oct. 2007.

[58] K. Roh, D. C. Martin, and J. Lahann, “Biphasic Janus particles with nanoscale anisotropy.,” *Nat. Mater.*, vol. 4, no. 10, pp. 759–63, Oct. 2005.

[59] Z. Nie, W. Li, M. Seo, S. Xu, and E. Kumacheva, “Janus and ternary particles generated by microfluidic synthesis: Design, synthesis, and self-assembly,” *J. Am. Chem. Soc.*, vol. 128, no. 29, pp. 9408–9412, 2006.

[60] B. Liu, W. Wei, X. Qu, and Z. Yang, “Janus colloids formed by biphasic grafting at a pickering emulsion interface,” *Angew. Chemie - Int. Ed.*, vol. 47, no. 21, pp. 3973–3975, 2008.

[61] T. Tanaka, M. Okayama, Y. Kitayama, Y. Kagawa, and M. Okubo, “Preparation of ‘mushroom-like’ janus particles by site-selective surface-initiated atom transfer radical polymerization in aqueous dispersed systems,” *Langmuir*, vol. 26, no. 11, pp. 7843–7847, 2010.

[62] B. R. Martin, D. J. Dermody, B. D. Reiss, M. Fang, L. A. Lyon, M. J. Natan, and T. E. Mallouk, “Orthogonal self-assembly on colloidal gold-platinum nanorods,” *Adv. Mater.*, vol. 11, no. 12, pp. 1021–1025, 1999.

[63] Y. Mei, G. Huang, A. a. Solovev, E. B. Ureña, I. Mönch, F. Ding, T. Reindl, R. K. Y. Fu, P. K. Chu, and O. G. Schmidt, “Versatile approach for integrative and functionalized tubes by strain engineering of nanomembranes on polymers,” *Adv. Mater.*, vol. 20, no. 21, pp. 4085–4090, 2008.

Chapter 2:

Methods

2.1 Overview

This chapter aims to produce the background information necessary to understand the procedures involved in the fabrication of self-propulsive active colloids, which will be covered in the first half of this chapter and how their motion is characterised, which will be covered in the last half of this chapter. Further specific information will be provided in each specific chapter.

2.2 Synthesis

2.2.1 Plasma Cleaning

An important aspect in the preparation of nano to micron scale active colloids is the cleanliness of the substrate used to hold the colloids on a planar surface for catalyst deposition by metal evaporation (see section 2.2.3). When metalized colloids are subsequently removed from a substrate, loosely attached debris and contaminants which also get coated in platinum may be transferred. The reactive debris can cause issues in the unwanted decomposition of hydrogen peroxide potentially causing flow and a build-up of bubbles if the rate of decomposition becomes too high. To minimise this potential, plasma cleaning was used.

Organic based impurities can be removed from the substrate by oxygen plasma cleaning[1]. In this process the inorganic substrate is subjected to a low pressure (~ $1\text{x}10^{-3}$ bar) oxygen gas environment. A high frequency Radio frequency (RF) generator is used to ionize the oxygen to generate the oxygen plasma. Oxygen ions are aggressively oxidising and readily react with carbon to form gaseous carbon monoxide and carbon dioxide which are removed through the vacuum pump, .

A Diener electronic (ZEPTO) plasma system was used throughout the course of this work.

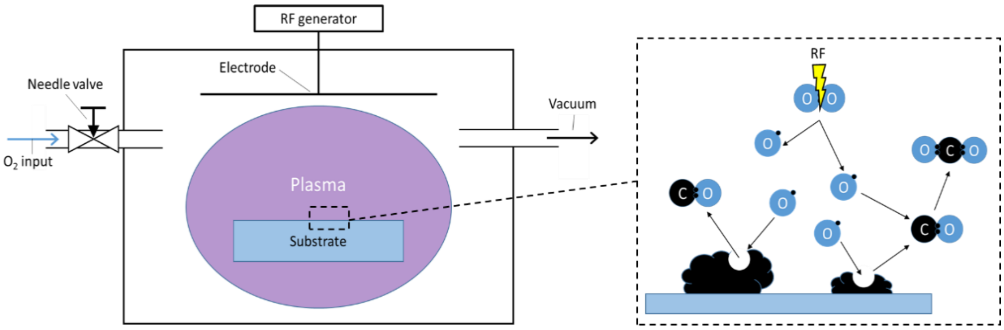

Figure 2.1 Left, Schematic of a Plasma cleaner with an oxygen inlet. Right, schematic of oxygen radical generation and reaction with carbon based impurities to form gaseous carbon species.

2.2.2 Spin Coating

Spin Coating is a well-established technique in micro-fabrication used to prepare thin films of materials on a flat substrate. This technique employs the simple principle of centripetal forces generated by spinning objects. When volatile solutions are added on top of a spinning substrate the centripetal forces spread the liquid across the surface and facilitates its evaporation. Any non-volatile components of the solution are left behind, spread across the surface of the substrate in a thin layer.

Here we use the spin coating technique to prepare disperse colloids on to a flat substrate before subsequent metal deposition is used to create active Janus colloids. In a typical procedure, colloids between 1-2 µm in diameter are dispersed by sonication in an ethanol/water mix to a low weight percentage suspension. The colloidal suspension is dropped a microliter aliquot on to the flat substrate while it is spinning at high speeds. The substrate is anchored to the rotating shaft by a partial vacuum as seen in figure 2.2 The most desirable outcome for the fabrication of active Janus colloids is a high density monolayer of dispersed non-touching colloids to maximise the number produced without causing shadowing effects that arise from touching colloids due to the line of sight nature of the metal coating technique used (Section 2.2.3 Physical Vapour Deposition (PVD)). The parameters for spin coating (colloid number density, dispersant composition and volume, spin speed) must be carefully controlled to create optimal conditions.

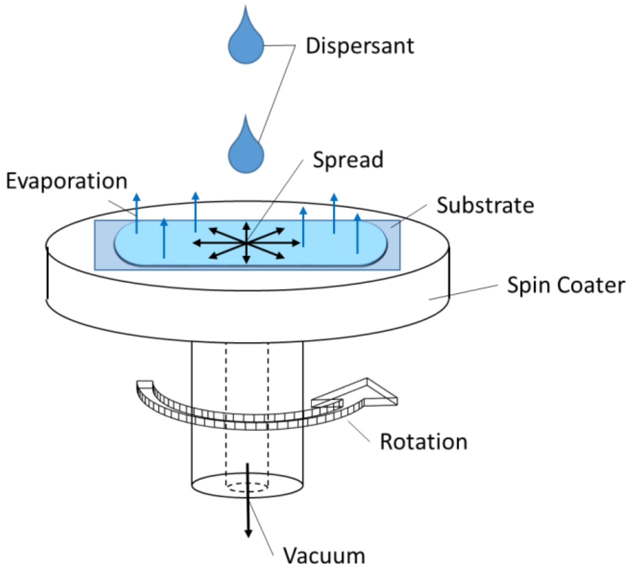

Figure 2.2. Schematic for spin coating where the material to be coated is spread across a rotating substrate through use of a liquid solvent or dispersanrt.

2.2.3 Physical Vapour Deposition (PVD)

Thin layer deposition of metals is currently pivotal in the fabrication of active colloids as described in chapter 1. Physical Vapour Deposition (PVD) is a well-established route to create thin layers of materials and is employed in many different synthetic procedures. PVD relies on a basic principle of vaporisation of a target material. The gaseous vapour then condenses on to the desired substrate. The method of vaporisation and the conditions required have important consequences on the resulting morphology of the material deposited. Described below are two common methods for vaporisation and the consequences of the resulting morphology are discussed.

2.2.3.1 Evaporation

PVD by evaporation provides enough energy to the target material to cause vaporisation. Two common methods to provide sufficient energy are: thermal evaporation where heat is supplied via resistive heating of a filament connected to the target material, and electron beam (e-beam) evaporation where energy is supplied by a beam of electrons which is directed into the material and heats up the target material. An e-beam evaporator can reach higher temperatures and is therefore capable of evaporating a wider range of materials.Additionally it produces purer films as thermal evaporators often generates impurities from the heating elements [2][3]. The principal method for metal layer coating in this project is by e-beam evaporation, largely due to the high melting point of platinum which makes thermal evaporation of platinum difficult.

Evaporated atoms may collide with gaseous species causing random scattering. At the high vacuum conditions required to allow metal vaporisation (approximately 1x10^{-9} bar) the number of gaseous species is low and therefore the evaporated metal has a high probability of travelling in a persistent direction for longer. The mean free path (MFP) of an evaporated atom can be estimated from Equation 2.1, and is inversely proportional to the pressure (P) [4]. This is a crucial aspect of evaporation as it results in a line of sight coating that allows a high level of spatial control over the deposition result.

$$MFP = {}^{6.63\ \times 10^{-3}}/_{P}$$

Equation 2.1

The basic set-up for an e-beam evaporator is shown below in Figure 2.3. Briefly, a filament generates electrons which are directed by a magnetic field onto the source material (most frequently platinum in this work) for the metal layer deposition which is contained within a crucible. The crucible is contained within a water cooled copper hearth, this cooling is important for keeping the housing material cool so as to not accidentally vaporise it by thermal transfer and thereby produce impurities. The vaporised material is emitted from the surface of the target metal. Under high vacuum this material travels in a line of sight propogation before condensing onto the first object it comes in to contact with. This line of sight behaviour is important in respect to positioning of the samples which are to be coated.

The thickness of the deposited layer is determined by a quartz crystal microbalance (QCM), a piezoelectric material which with an applied electric field oscillates at a particular frequency. This frequency changes with mass and therefore the a QCM in the line of sight of the evaporated metal can give the thickness of the deposited metal by changes in the oscillating frequency (caused by deposited metal changing the mass on the QCM) [5].

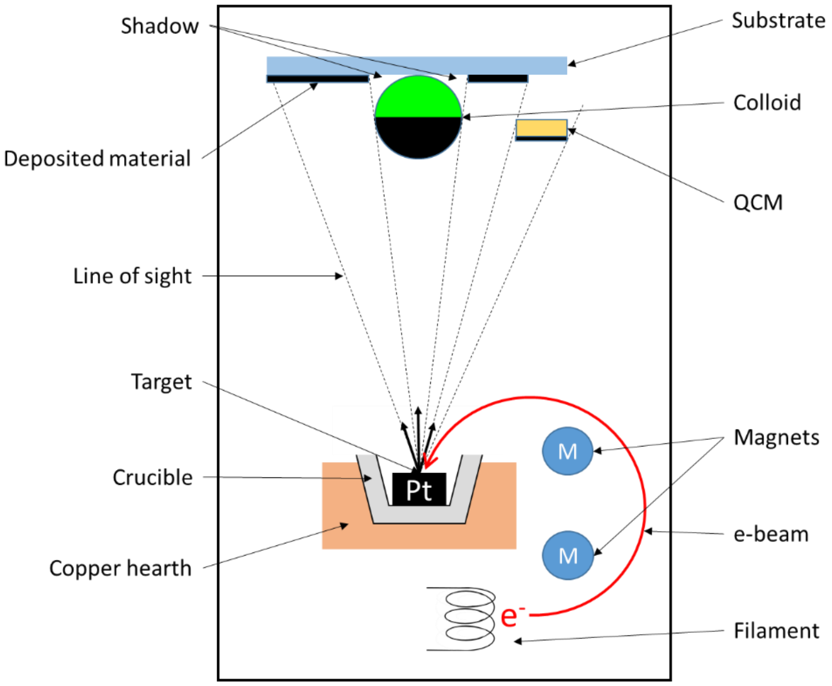

Figure 2.3. Schematic for physical vapor deposition. Cotated colloid shows hemispherical metallisation due to line of sight coating.

2.2.3.2 Sputter coating

Sputter coating is a PVD technique that works on the principle of erosion of a target material leading to material ejection from the surface as opposed to evaporation discussed in section 2.1.3.1.

A target material is surrounded by an inert gas, typically argon, which is ionised to create a plasma. As with plasma cleaning, the plasma is generated via high voltage electrodes operating at radio-frequencies. This causes ionization of the argon gas which is constrained to be near the target material through use of magnetic fields. Argon ions then collide with the target material with enough kinetic energy to eject material in the form of atoms or clusters from the surface.

Due to the inherent necessity of argon gas, the pressure at which sputter coating operates (1×10^{-3} bar) is significantly higher than for evaporation. An important consequence is the drastic shortening of the MFP. As such the eroded target material is far less likely to take a line of sight path to the substrate but instead takes a randomised path. This diminishes the directionality of this approach and can thereby coat the target material outside of the line of sight by virtue of the randomised path. Shadowing therefore does not occur by any other means than physical obstruction by direct contact. A schematic for sputter coating is given in Figure 2.4.

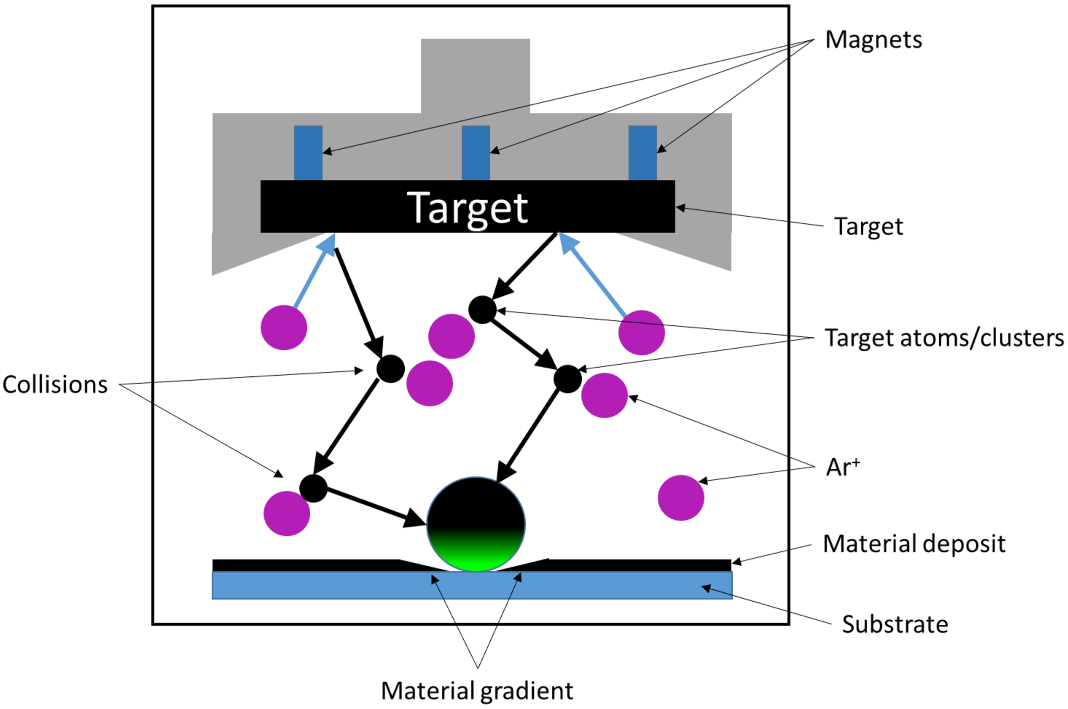

Figure 2.4. Schematic for Sputter coating. Colloid shown with metallisation beyond line of sight as coating are not restricted by line of sight.

2.2.4 Sol-Gel

Sol-Gel chemistry is a versatile technique which allows the facile formation of inorganic solids from a solution of soluble metal alkoxide pre-cursors. Typically this occurs through condensation polymerisation of the alkoxide monomers leading to metal oxide polymer structures, the end morphology of which can be controlled through the initial starting conditions, such as pH [6]. Of particular interest for this thesis is the ability to use sol-gel chemistry to generate colloids with a high level of size and morphological control. Due to the influences of these factors on swimming behaviour as previously discussed in Chapter 1, these factors must be as consistent as possible to draw reliable conclusions when changing other variables.

Wener Stober first showed that through silica precursors, SiO_2 could be synthesised as spherical nanoparticles with size monodispersity [7]. Many papers since have been published offering a variety of methods to control the dispersity, the morphology and size of sol-gel generated silica colloids [8]. The most common method for preparing monodisperse silica colloids is through the hydrolysis and condensation of the silica pre-cursor Tetraethyl orthosilicate in a base catalysed reaction in the presence of water. The mechanism for hydrolysis involves the deprotonation of water which then allows nucleophilic attack of the silicon when an ethoxy group is protonated to make a good leaving group, regenerating the catalyst and producing ethanol as a side-product as shown in Figure 2.5. The hydrolysed silanol monomer, can then condense with other monomers in the presence of the base catalyst. Shown below is a dimerization, with continued reaction all silanol groups will condense to form the SiO_2 polymer network. As stated in Chapter 1, size of the colloids is an important factor when considering the motion of self-motile particles. For this reason size control in synthesis is essential. In this report, monodisperse silica colloid synthesis in the low micron range is desirable and is achieved by two different methods reliant on the same principles as described above.

Micron sized monodisperse silica is difficult to prepare in one step. A two-step method which involves first synthesising or using pre-fabricated smaller silica nanoparticles which are comparatively easy to make monodisperse, and using these as a seed to further grow silica by gradually introducing Tetraethyl orthosilicate (TEOS) into a solution containing the seed particles and a catalyst causing the TEOS to hydrolyse and condense on the existing silica surface [9]. The result is a uniform growth of the silica seed particles while keeping the size disparity constant. The growth is determined by the quantity of TEOS added relative to surface area of the seeds given by the number and size of said seeds. Chang, Lee and Kim make the claim that the key to uniform seed growth is the rate of addition of TEOS: if the concentration of hydrolysed TEOS becomes supersaturated, unwanted secondary particles will form [10].

The second approach is a continuous feed reaction, similar to the second stage of the seed growth. TEOS is fed into a reaction mixture containing the alcohol based solvent, water and the catalyst with no seed particles, over a set period of time (fixed rate). The nucleation occurs when the hydrolysed silanols reach a critical concentration and condense out as nanoparticles, these initial nanoparticles then act as the nuclei for further growth by a steady build-up of silanol groups condensing on the surface. This one pot method is an attractive method for the sol-gel synthesis of silica [11]. This method is made even more attractive as it was discovered that in the one pot method, the rate of addition of the silica pre-cursor TEOS had influence of the final size of the silica colloids, giving easy size control [12].

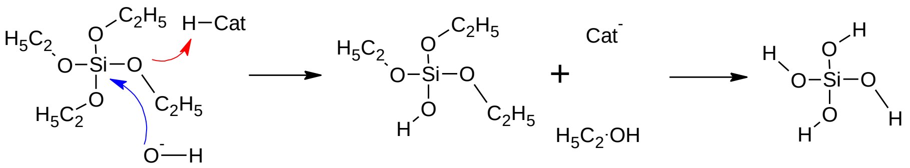

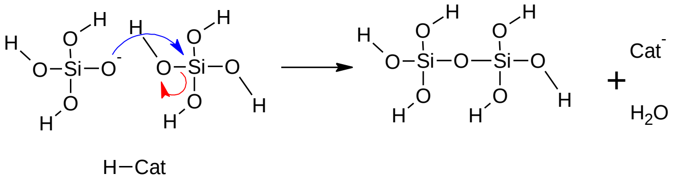

Figure 2.5. Reaction schematic for based catalysed condensation polymerisation of silica alkoxides. The reaction is displayed only as far as dimerization for simplicity.

2.2.5 Surface Functionalisation

Silica shows versatile chemistry which can be exploited to achieve a variety of goals which will be utilised in chapters 3 and 5. For silica colloids, while the bulk silica is covalently saturated, the surface is terminated in silanol groups which can react with purchasable silicon species containing a desired functional group to covalently anchor the desired functionality onto the surface. There are many silane species available to purchase and many purchasable silanes can be further reacted to alter their chemistry allowing a vast array of different functionalities.

There are two approaches to adding functionality to a silica surface. Adapting the seed growth technique for the growth of silica, an alternative to TEOS can be used. Silanes with functional groups can be used instead, they will condense and grow much like TEOS around a silica core but with the added functional group, this approach then affects the size and surface functionality [13]. The effect of altered size of the colloids for this method is a clear disadvantage as size control is crucially important for the synthesis of self-motile particles. An alternative approach, and a more commonly used method for surface modification, is known as grafting. Grafting reacts the methoxy or ethoxy groups of the desired silane species with the silanol groups on the surface at elevated temperatures. Simply refluxing colloids with the silane species results in modified surface [14]. Crucially, this is a monolayer modification, the colloidal size will not be noticeably affected and therefore this is the chosen method of surface functionality in this project. The mechanism is shown below in Figure 2.*6*.

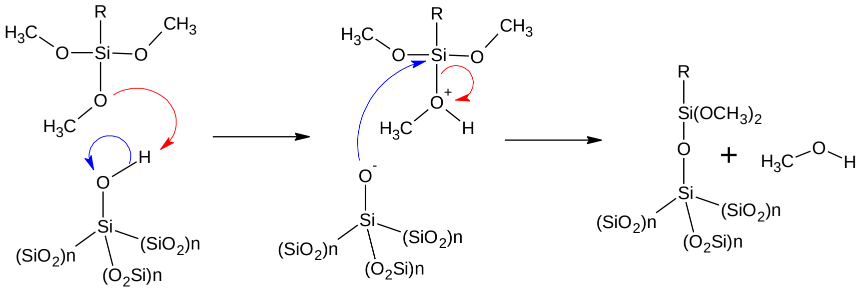

Figure 2.6. Reaction schematic for the non-catalysed coupling of a functionalised silicon alkoxide and a surface silanol group.

2.3 Analysis and Characterisation

2.3.1 Optical Microscopy

Optical microscopy is a technique used to magnify objects by using lenses to bend light and create virtual images which are larger than the source object. This allows objects too small for the naked eye to become observable. Here we use optical microscopy to observe micron-scale colloids.

Two main types of microscope set-ups are commonly used, namely brightfield and darkfield. Brightfield microscopy passes light through a sample and directly into an objective, the subjects of interest block the transmission of light to the objective and therefore show as dark shadows. In darkfield microscopy, light does not directly enter the objective. Instead light passes past into the sample and the sample reflects light indirectly into the objective which therefore show as illuminated objects in a dark background. In this study we exclusively use brightfield microscopy.

A basic representation of brightfield microscopy set up is given in Figure 2.7. Briefly, a light source is used to illuminate a sample. An aperture is located across the light source, designed to control the output of light intensity reaching the sample. A condenser lens is used to focus the light source on to the sample. The objective is the lens closest to the sample and the focus lens directs the image to the camera. It is important to note that light microscopy has an inherent limit to the size of a resolvable object (d) known as the Abbe diffraction limit, caused by both the fundamental diffraction of light based on the wavelength of the light (λ) in conjunction and the numerical aperture (NA, mathematically described as $n\ sin\theta$) of the objective as described mathematically below (Equation 2.2).

$$d = \frac{\lambda}{2\ n\ sin\theta}$$

Equation 2.2

The diffraction limit arises from the wave like behaviour of light which diffracts between sufficiently small spaces. During diffraction, the coherent incident light waves combine as a singular product of constructive and destructive interference resulting in an unresolved image with consecutive light (constructive interference) and dark rings (destructive interference). The degree of this diffraction is dependent on the wavelength (λ) of the incident light.

The numerical aperture of the objective is defined by the angle of the cone of incident light which the objective receives and the refractive index of the media within which the light propagates. Objectives can reach numerical apertures of up to approximately 0.95 in air, however using oil immersion objectives can further increase the NA up to 1.4 due to the high refractive index of oil. This can limit the resolution of the microscope with a dry objective to approximately 200 nm even for blue light. For the work conducted in this thesis we observe objects between 800 nm and 5000 nm. Using visible light microscopy is entirely suitable for characterisation of these particles.

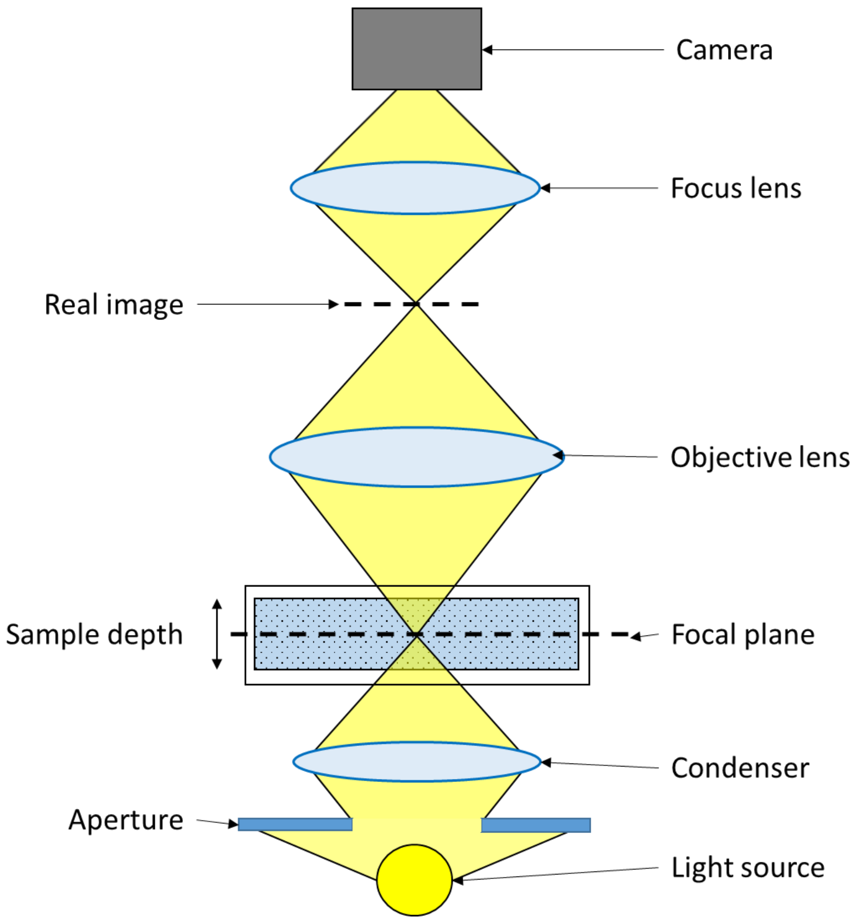

Figure 2.7. Schematic for Brightfield microscopy.

2.3.2 Scanning Electron Microscopy (SEM)

Scanning Electron Microscopy (SEM) is an imaging technique that uses electrons as opposed to visible electro-magnetic radiation used in optical microscopy. Electrons have a smaller wavelength than visible light and therefore have a significantly higher diffraction limit as stated by the Abbe resolution limit. In short, this allows an electron microscope to see far greater detail than its optical counterpart. SEM has further advantages in that the electrons' interaction with the surface is dependent on the composition of the sample and therefore allows some compositional analysis. This feature is particularly exploited in chapters 4 and 5 to assess the active cap shape and coverage.

A simple schematic for SEM is give below in Figure 2.*8*. Briefly, electrons are generated by an electron gun. Two types of electron guns are commonly used, tungsten filament based guns which use thermionic electron emission or Field Emission Guns (FEG) which uses an extremely strong electrostatic field to pull electrons from a metallic surface in to a free vacuum. Typically FEG systems produce a smaller more coherent electron beam compared with the tungsten filament systems[15]. FEG systems therefore produce better quality images, however are more expensive to run due to the ultra-low vacuum requirement. Both emission types have been used in this thesis depending on the scale of detail required.

Regardless of how the electrons are generated, an electron beam cannot penetrate far in atmospheric conditions due to the interaction of electrons with gaseous species. An SEM is therefore operated under vacuum to minimise these interactions. The vacuum requirement can place limitations on sample types able to be analysed to those unaffected by low pressure environments. An anode placed near the electron gun is used to accelerate the electrons towards the sample. The difference in voltage potential between the anode and the electron gun can be changed, typically between 1 and 20 KeV. The result is the ability to change the energy of the electron beam which in turn dictates signal intensity and the electron's penetrative depth into the sample. Accelerated electrons are passed into a condenser lens. A condenser lens uses magnetic fields in order to converge the electron beam. To further narrow the beam an aperture is used to control and restrict the beam size passing through. Scanning coils again use magnetic fields to manipulate the electron beam. In this instance however, the magnetic field is used to sweep the electron beam in a raster pattern across the sample surface in order to scan the topography and build a larger image from a small electron spot-size. Finally, the objective lens is used to focus the beam on to the sample by controlling the working distance.

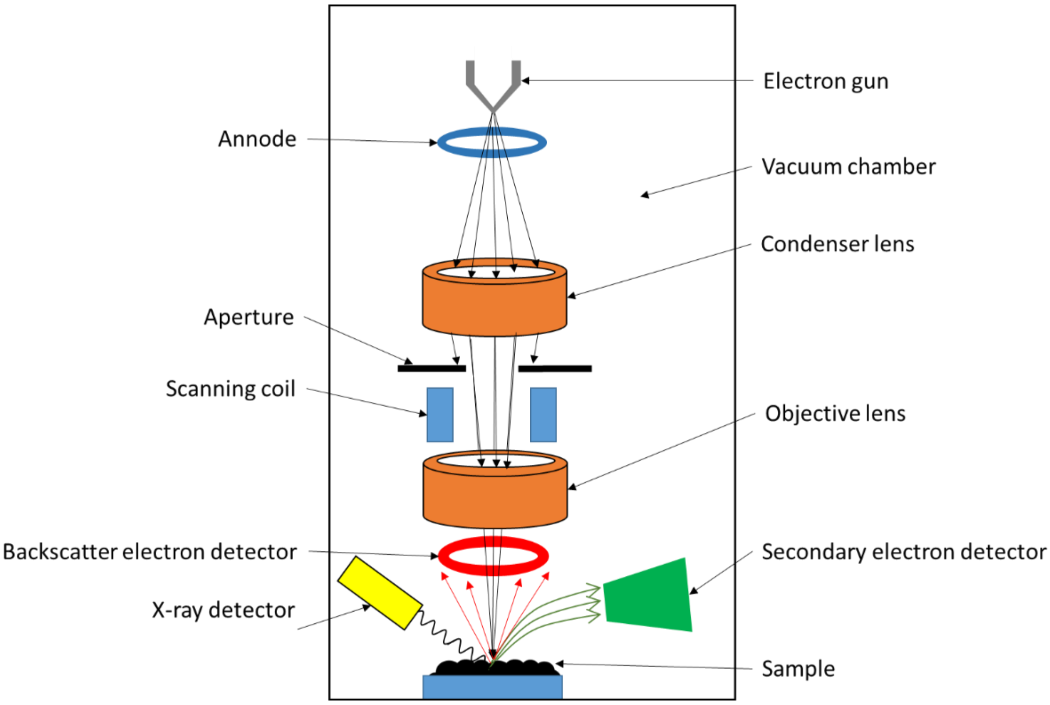

Figure 2.8. Schematic for scanning electron microscopy (SEM).

The incident electrons can interact with the atoms of a sample in three main ways. Each different interaction can be measure independently to garner different information from the sample.

Firstly, the incident electron can knock electrons out of the sample, the liberated electrons are denoted as secondary electrons (SE) (Figure 2.9a). The SE are low in energy due to the energy required to overcome the work function and eject the electron from the atom. The secondary electron detector uses a cage with a small positive potential applied to selectively draw in the low energy SE while the more energetic electrons are minimally affected by the weak positive potential and therefore are not biased towards the detector. This provides a high signal to noise ratio.

Secondly, the incident electrons can be deflected by the nucleus of the atoms in the sample back towards the incident source (Figure 2.9b). These are known as backscattered electrons (BSE). The deflection is elastic in nature and so the BSE remain highly energetic. The backscatter detector is placed above the sample, as the elastically scattered BSE are deflected back towards the incident beam. A key advantage to backscatter detection is that the efficiency of backscatter is proportional to the mass of the atomic nucleus. Heavier atoms are more likely to cause backscatter which gives a higher detection signal. This feature can be exploited to highlight contrast between spatially separated regions containing heavier and lighter atoms

Thirdly, the incident electrons can knock electrons from lower energy orbitals. As an electron from a higher energy orbital fills the created vacancy, energy is released in the form of x-rays (Figure 2.9c). The energy of the corresponding x-ray is equal to that of the electron transition which due to the discrete and nucleus dependant energy levels of the orbitals, creates characteristic x-rays which can be used to identify and even spatially map elements in the sample. This analysis techniques is known as energy dispersive x-ray spectroscopy (EDS).

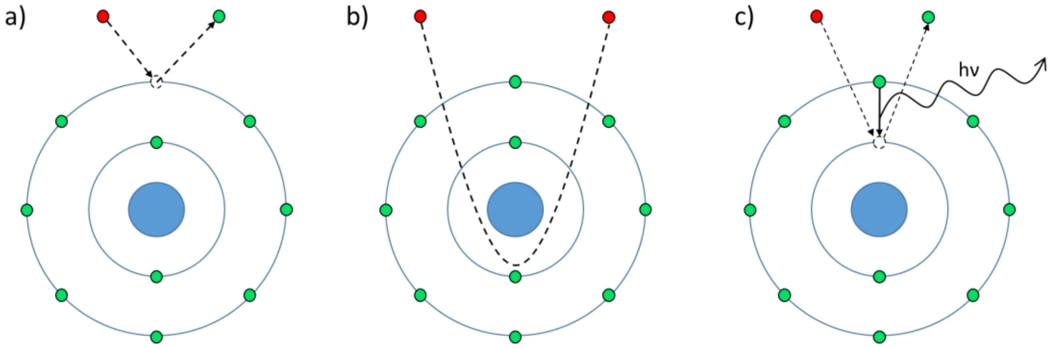

Figure 2.9. Schematic for the three typical interactions between the electron beam (red) and the subject atoms. a) Secondary electron emission, b) Backscattered electrons and c) Electro-magnetic wave emission.

As electrons from the incident beam hit the surface of the sample, it is possible for charge build up to occur. Samples with poor conductivity build charge in the scanned area as the electrons do not readily dissipate. A charge build up leads to image distortion as the surface of the sample becomes repulsive to the scan beam. It is therefore important to provide conductive pathways on insulating samples to prevent charge build up. The most common method to achieve this is through sputter coating a thin (10-15 nm) conductive layer, typically gold, on to the sample surface. While sputter coating gold on to samples effectively prevents the build-up of charge, the elementally homogenous topical layer masks information potentially gained from backscattered and EDS modes. As an alternative, Carbon coating can provide a thin film of electrically conductive amorphous carbon which as a low atomic number element, does not backscatter strongly and allows some contrast from the sample to be retained.

2.3.3 Atomic Force Microscopy (AFM)

Atomic Force microscopy is an imaging technique used to obtain topographical images of sample with nanometre resolution. AFM can also be used to obtain information about the hardness of the material.

The basic principle of AFM is to use an ultra-fine, nano-dimensioned tip connected to a cantilever which is scanned across the surface of a substrate. A laser focused on the cantilever is reflected onto a photodiode. As the cantilever bends in response to changes in the topography of sample, the laser in turn is deflected and this change is recorded by the photodiode. A feedback loop is established between the photodiode and the cantilever which opposes the change in the laser position on the photodiode by triggering a piezoelectric actuator to change the z-height of the cantilever. This feedback mechanism therefore is present to keep the AFM tip in close proximity to the sample and prevent drift from the surface. A schematic for AFM is given in Figure 2.10.

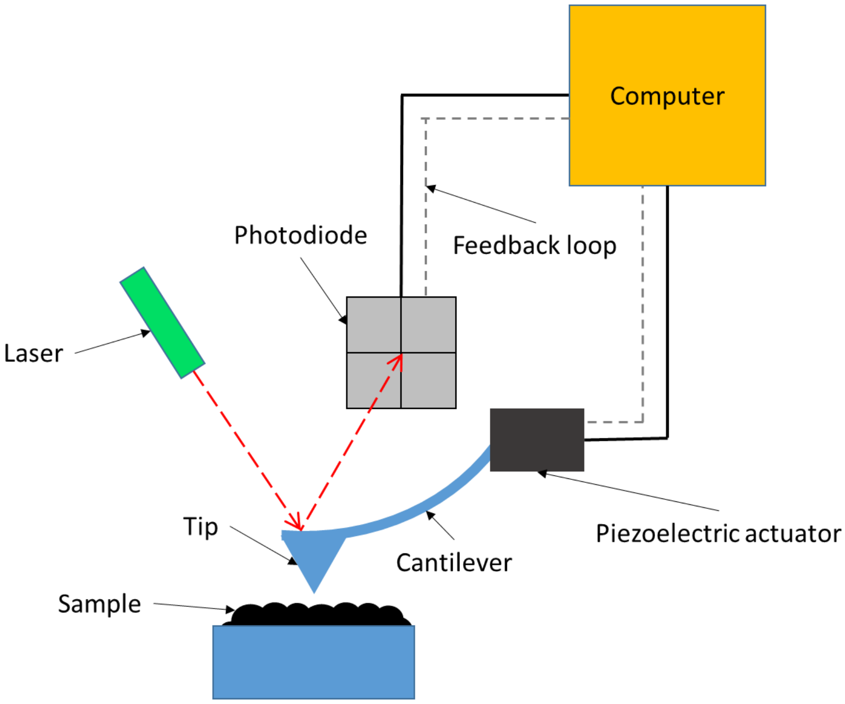

Figure 2.10. Schematic for AFM

2.3.4 Nano Tracking Analysis (NTA)

Nano Tracking Analysis (NTA) is a relatively new technique based on direct tracking of individual particles in a solution.

NTA uses a measurement of the Brownian motion of particles to derive their size. The Diffusion coefficient (D) of the particle is found directly from particle trajectories and used in the Stokes-Einstein equation (equation 2.3) to obtain the hydrodynamic radius of the particle (r), where K_B is boltzmanns constant, T is the temperature and η is the viscosity [16].

$$D = \frac{K_B T}{6\pi\eta r}$$

Equation 2.3

Both NTA and dynamic light scattering (DLS) use Rayleigh scattered laser light to observe particles in solution. The key difference between the Nanosight and a DLS is how the scattered light is interpreted and used.

DLS measures the rate of change in intensity of a diffraction pattern caused by scattered light over time. Since smaller particles have a higher diffusional constant (inversely proportional from r as can be seen in equation 2.3) the rate of change in scattered intensity will be greater. The rate of change in intensity can then be related to the diffusion coefficient D which can be used to give the hydrodynamic radius r [17].

The Nanosight, instead of using an overall pattern, observes the scattered light of individual particles in solution. The Nanosight achieves single particle identification through use of an attached microscope to correlate scattered light intensity to spatial position. This then allows for tracking of the spatial position of multiple individual particles over time and the calculation of the mean square displacement from which the diffusion coefficient and size can be calculated (Figure 2.*11*).

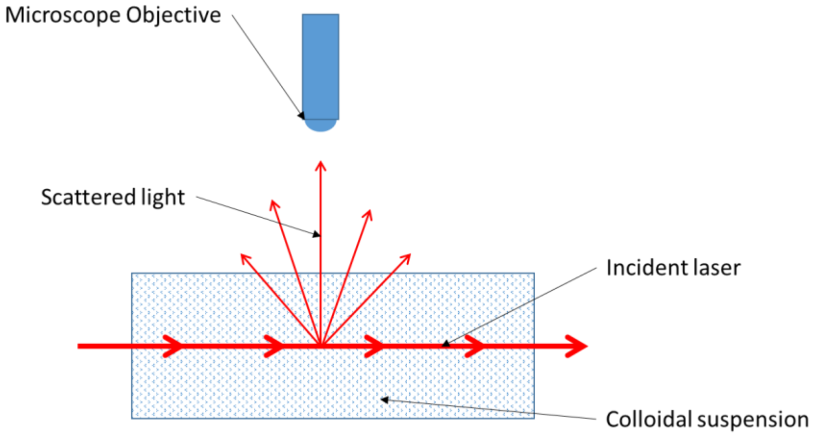

Figure 2.11. Schematic for Nano-tracking analysis.

2.3.5 Zeta Potential

Zeta potential is a measure of electrostatic potential of fluid near the colloid surface which gives information on the surface chemistry of colloids and also their dispersibility in water due to electrostatic interactions.

The zeta potential can be measured using the principles of electrophoresis, where an applied electric field on a charged particle in an electrolyte induces motion. The velocity of the particle (v) is proportional to the applied field strength (E) and the zeta potential (ζ) which gives the electrophoretic mobility (μ) (Equation 2.4), the electrophoretic mobility is therefore found by observing the velocity of colloids in relation to an applied electrical field [18].

$$\mu \propto \frac{v}{E}$$

Equation 2.4

Zeta potential (ζ) measured by electrophoresis is then given by the Smoluchowski equation (Equation 2.5) determined by the electrophoretic mobility (μ), the permittivity of the medium (ε) and the viscosity of the medium (η) [19].

$$\mu = \frac{\varepsilon\zeta}{\eta}$$

Equation 2.5

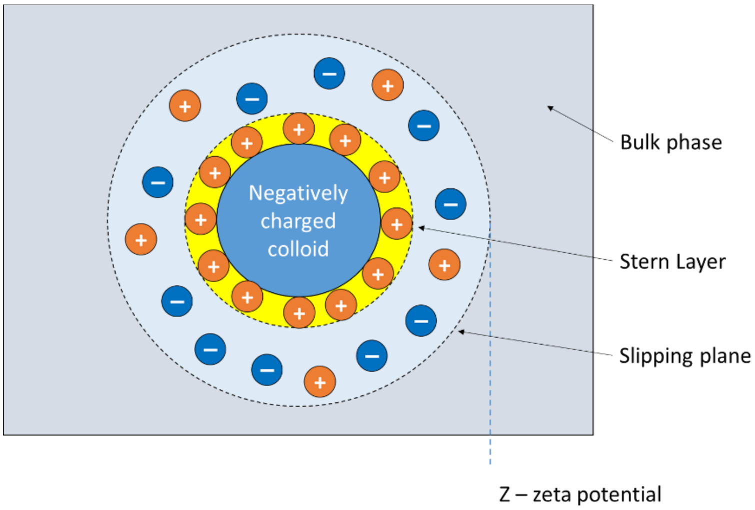

Figure 2.12. Schematic for a colloid with a negative electrostatic potential and how this orientates mobile charges in solution.

2.3.6 UV-Vis Spectroscopy

UV-Vis spectroscopy is an analytical technique that can be used to determine the concentration of analytes in a solution (as well as assisting in the identification in the composition of unknown solutions). In the context of this thesis, the catalytic decomposition of hydrogen peroxide by platinum can be followed using UV-Vis spectroscopy to follow the depletion of hydrogen peroxide over time.

UV-Vis spectroscopy works because many chemical species, including hydrogen peroxide, absorb light in the visible to ultra-violet wavelength due to the excitation of electrons in their orbitals. As electron transitions occur at discrete energy transitions the wavelengths of light absorb (which must precisely match in energy to the electron transition) this causes identifiable absorption spectra which can be used to single out particular species in a solution.

The concentration of the analyte can be determined simply by measuring the change in intensity of light as it passes through a sample given that the change in intensity (due to absorption) is proportional to the concentration of the analyte and the path length of the sample (a known value). More precisely, the concentration can be determined mathematically from the Beer-Lambert law as given in Equation 2.66 below, where “Abs” is the absorption of light, $log_{10}\frac{I_0}{I}$ is the mathematical description of absorption representing the difference in the incident light (I_0) to the light received after passing through the sample (I). The path length of the cell (l), and the concentration (c), together can be considered as the likely-hood of interception. The molar absorption coefficient ε, is a chemical specific attenuation factor, this can be considered as the absorption strength of a species.

$$Abs = log_{10}\frac{I_0}{I} = \varepsilon cl$$

Equation 2.6

For the Uv-Vis spectroscopy conducted in this work, an Ocean Optics system is used. A simple system schematic is given below in Figure 2.13. Briefly, a light source emitting the full range of wavelengths needed, is collimated by a mirror onto a diffraction grid. The diffraction grid spatially splits the homogenous incident light by its component wavelengths. The now spatially separated wavelengths are focused by a mirror through a sample. The attenuated light received through the sample is detected by a CCD detector which converts the optical input to an electronic output signal. The electronic output is then passed to a computer for recording.

In practise, solvent without analyte is first anaysed in order to record a background absorption spectrum. The sample containing analyte can then be measured with the background subtracted from the reading. Any absorption can then be reasonably stated to be from dissolved compounds in the solvent.

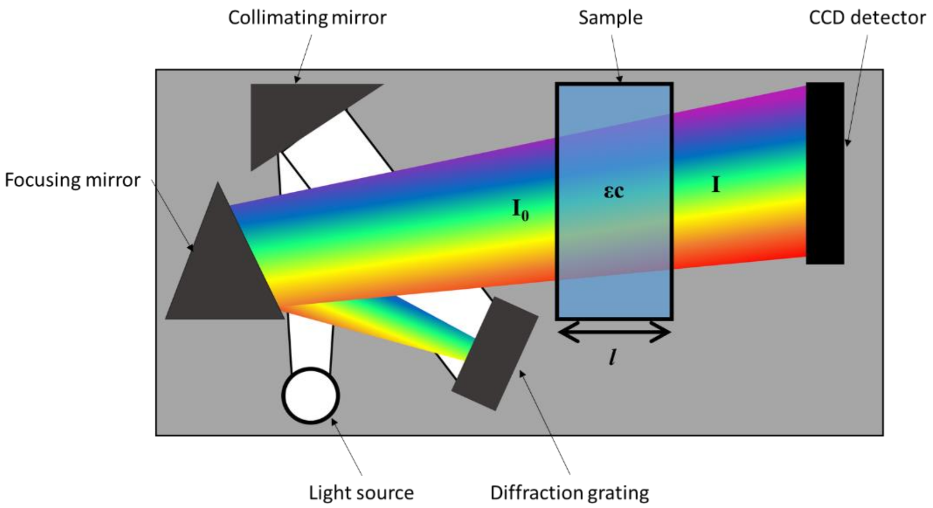

Figure 2.13. Schematic for a UV-Vis spectrometer. In this example a multi-chromatic spectrometer is shown. Monochromatic versions use a slit after the diffraction grid to sweep through singular wavelengths incrementally.

2.3.7 Particle Tracking and Quantification

The self-motile colloids studied in this thesis display enhanced motion in hydrogen peroxide as discussed in chapter 1. A necessity arises to characterise their motion. Here we use Mean Squared Displacement (MSD) to mathematically describe their motion and quantify their velocity. The MSD quantifies the average displacement of objects over incremental time periods. The advantage of using MSD over a simpler calculation such as the instantaneous velocity, is that MSD can be used to distinguish between different regimes of colloidal motion, as stated by Dunderdale *et al.* which will be discussed in more detail later in this section [20].

The colloidal motion is recorded using a Pixelink camera attached to the microscope. A LabVIEW programme created by Dr. Jonathan Howse and Dr. Stephen Ebbens is used to characterise the tracks from the output AVI files. Firstly, the programme locates particles through the contrast between the object and its surroundings. The threshold of contrast detection is a user defined value. From these detectable objects, the centre of mass is calculated and an x, y coordinate is assigned. This is repeated for each frame to build a complete Δx,Δy profile over the length of the video. Coordinates are initially given in pixels but are easily converted to micrometres by comparing against a reference material of known size to give a pixel to micron calibration factor. In this work a Copper TEM grid with known grid spacing's (D) of 63.5 µm is used as a calibration standard, as shown below in Figure 2.*14*.

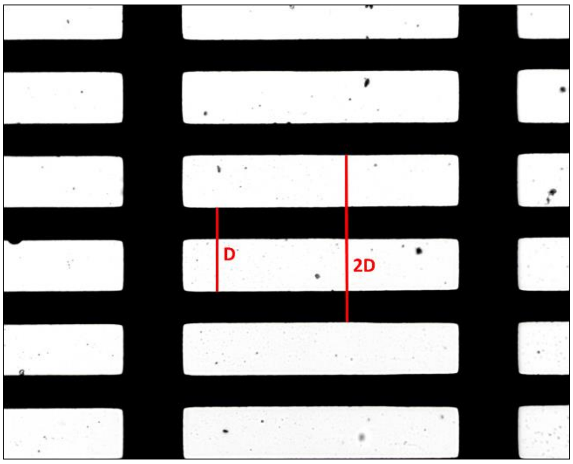

Figure 2.14. TEM grid with known spacing's used for conversion between pixels and distance (typically reported in microns). D represents the standard single spacing of 63.5 µm.

From the raw experimental data where a colloid has been recorded by video camera at *n* frames per second, a series of x,y spatial coordinates are generated for each frame (representing defined intervals of time). Through basic trigonometry we find the step length (ΔL) by the change in the x (Δx) and y (Δy) position ($\Delta x^2 + \Delta y^2 = \Delta c^2$) we can ascertain the colloid step length ($\Delta c^2 = \Delta L^2$) between frames.

The MSD values are calculated by averaging the squared step length over incremental time intervals (Δt). For example at Δt = 1s, vectoral paths between the colloid positions every 1 second are taken and an average value is obtained. Δt = 2s, vectoral paths between the colloid positions every 2 second are taken and an average value is obtained and so forth.

Figure 2.15 below demonstrates how the averaging is performed. For simplicity the schematic shows only 6 positions over three time intervals, Δt_n, $\Delta t_{n+1,}$ Δt_{n+2}. The MSD for the first time interval then becomes the squared average of the blue lines, for the second time interval –

the squared average of the red lines and finally the third time interval is the squared average of the green lines. A typical experimental system contains 1000 positions (frames) and therefore many more data points which allows statistically significant analysis.

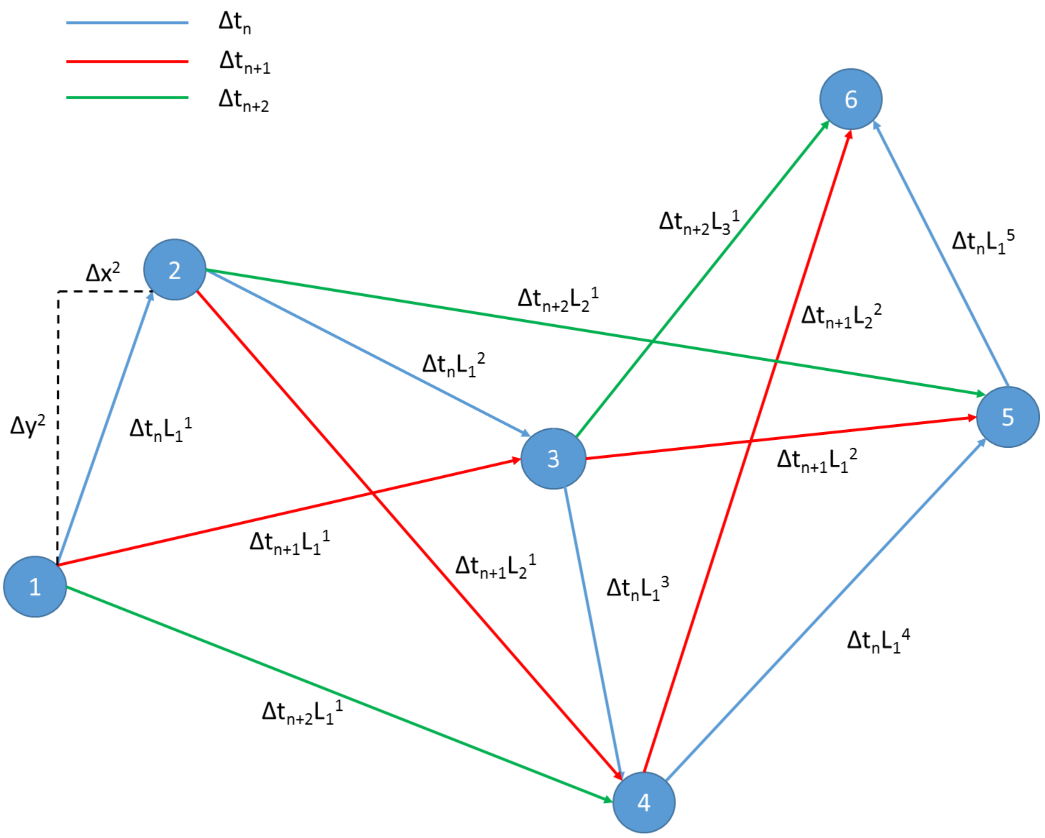

Figure 2.15. Schematic demonstrating a simple 6 position MSD calculation from the averaged sum of transformations per time interval.

The MSD profile built from applying this to the active Janus colloids can then be used to derive the relevant information from the MSD 2D form equation to the data (Equation 2.7).

$$\langle \Delta L^2 \rangle = 4D\Delta t + \frac{v^2 \tau_R^2}{2}\left[\frac{2\Delta t}{\tau_R} + e^{\left(\frac{2\Delta t}{\tau_R}\right)} - 1\right]$$

Equation 2.7

It is important to note that for objects displaying enhanced motion the MSD consists of two main forms based upon the rotational diffusion of the colloid(τ_R). The rotational diffusion re-orientates the particle at a frequency related to its diameter and therefore also re-orientates the trajectory of enhanced motion in conjunction. At time periods well below τ_R the particle can be considered to be not rotating and therefore is travelling in a persistent direction. As a consequence the MSD shows a quadratic increases as the active colloid consistently moves away from the point of origin.

Over longer time periods however, τ_R becomes an important factor as it randomises the trajectory. This randomisation leads to the MSD becoming linear in nature as the particle moves away from the point of origin in a randomised “enhanced diffusion” manor.

Dunderdale *et al*. described three different outputs from the MSD that would indicate different colloid motion. Firstly if the MSD is purely linear, it would be indicative of diffusive Brownian motion. If the MSD is purely quadratic over timescales longer than the rotational diffusion time of the colloid, this would not be indicative of colloidal motion and that the colloid motion is a result of external flow. If the MSD shows quadratic function at time scales below the rotational diffusion of the colloid returning to a linear function at time scales longer than the rotational diffusion this would show the expected MSD profile for propulsive active colloids[20].

To quantify the velocity from the MSD, Equation 2.7 must be fit to either the short time scale propulsive, quadratic function, or the longer time scale, linear function as presented below in *Figure 2.16*.

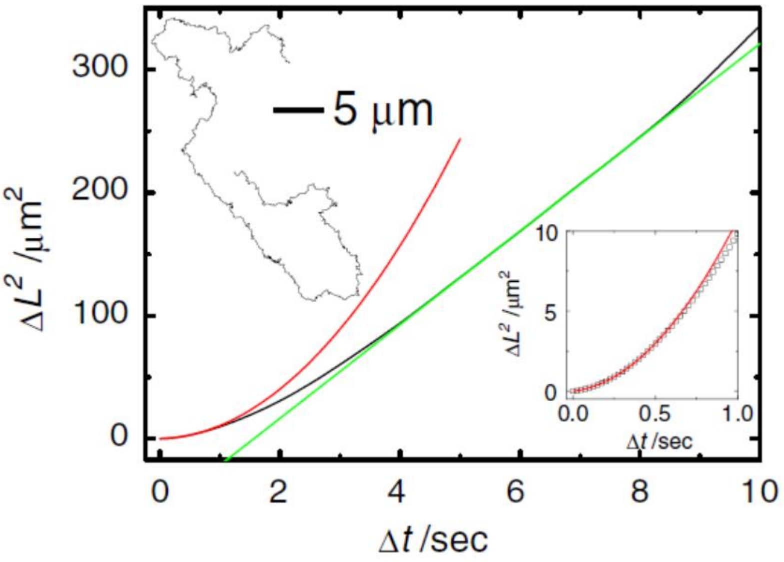

Figure 2.16. MSD plot (black) with two different mathmatical fits for short time periods (red) and long timeperiods (green). Top left inset gives the track from which the MSD was derived. Bottom right inset gives expanded view of the MSD at short time periods. Taken from [21].

These two limiting regimes can be described by simplified versions of Equation 2.7. When $\Delta t << \tau_{R,}$, Taylor expansion is used to remove the exponential function, Equation 2.8, which can be further simplified to Equation 2.9 and by elimination of redundant terms to Equation 2.10 which can then be applied to the curve fitting.

$$\langle \Delta L^2 \rangle = 4D\Delta t + \frac{v^2\tau_R^2}{2}\left[\frac{2\Delta t}{\tau_R} + \frac{(-2\Delta t/\tau_R)}{1!} + \frac{(-2\Delta t/\tau_R)^2}{2!} - 1\right]$$

Equation 2.8

$$\langle \Delta L^2 \rangle = 4D\Delta t + \frac{v^2\tau_R^2}{2}\left[\frac{2\Delta t}{\tau_R} - \frac{2\Delta t}{\tau_R} + \frac{4\Delta t}{2\tau_R}\right]$$

Equation 2.9

$$\langle \Delta L^2 \rangle = 4D\Delta t + v^2\Delta t^2$$

Equation 2.10

To fit the MSD equation to the quadratic form when Δt >> τ_R , where the MSD shows a linear increase due to 'enhanced diffusion' nature of the trajectories, Equation 2.7 must be modified to account for the exponential term becoming insignificant as τ_R becomes much larger than Δt (Equation 2.11) . Equation 2.11 can then be simplified to eliminate the exponential function, Equation 2.12 which can then be simplified to give Equation 2.14.

$$e^{\left(\frac{2\Delta t}{\tau_R}\right)} \Rightarrow e^{(-2\infty)}$$

Equation 2.11

$$\langle \Delta L^2 \rangle = 4D\Delta t + \frac{v^2\tau_R^2}{2}\left[\frac{2\Delta t}{\tau_R} - 1\right]$$

Equation 2.12

$$\Rightarrow \langle \Delta L^2 \rangle = 4D\Delta t + v^2\tau_R\Delta t - \frac{v^2\tau_R^2}{2}$$

Equation 2.13

$$\Leftrightarrow \langle \Delta L^2 \rangle = (4D + v^2\tau_R)\Delta t - \frac{v^2\tau_R^2}{2}$$

Equation 2.14

2.4 References

[1] Z. O. H. Li, A. Belkind, F. Janse, “An in situ XPS study of oxygen plasma cleaning of aluminum surfaces,” *Surf. Coatings Technol.*, vol. 92, no. 3, pp. 171–177, 1997.

[2] M. A. Parker, *Solid State and Quantum Theory for Optoelectronics*. Florida: CRC Press, 2009.

[3] M. J. Madou, *Fundamentals of Microfabrication: The Science of Miniaturization*. Florida: CRC Press, 2002.

[4] R. Kossowsky, *Surface Modeling Engineering*. Florida: CRC Press, 1989.

[5] K. Seshan, *Handbook of Thin Film Deposition*. Oxford: William Andrew, 2012.

[6] a. E. Danks, S. R. Hall, and Z. Schnepp, “The evolution of ‘sol–gel’ chemistry as a technique for materials synthesis,” *Mater. Horizons*, vol. 3, pp. 91–112, 2016.

[7] W. Stober and A. Fink, “Controlled Growth of Monodisperse Silica Spheres in the Micron Size Range,” *J. Colloid Interface Sci.*, vol. 26, pp. 62–69, 1968.

[8] A. Kuijk, A. van Blaaderen, and A. Imhof, “Synthesis of monodisperse, rodlike silica colloids with tunable aspect ratio.,” *J. Am. Chem. Soc.*, vol. 133, no. 8, pp. 2346–9, Mar. 2011.

[9] J. H. Zhang, P. Zhan, Z. L. Wang, W. Y. Zhang, and N. B. Ming, “Preparation of monodisperse silica particles with controllable size and shape,” *J. Mater. Res.*, vol. 18, no. 3, pp. 649–653, 2003.

[10] S. M. Chang, M. Lee, and W.-S. Kim, “Preparation of large monodispersed spherical silica particles using seed particle growth.,” *J. Colloid Interface Sci.*, vol. 286, no. 2, pp. 536–42, Jun. 2005.

[11] X.-D. Wang, Z.-X. Shen, T. Sang, X.-B. Cheng, M.-F. Li, L.-Y. Chen, and Z.-S. Wang, “Preparation of spherical silica particles by Stöber process with high concentration of tetra-ethyl-orthosilicate.,” *J. Colloid Interface Sci.*, vol. 341, no. 1, pp. 23–9, Jan. 2010.

[12] K. Nozawa, H. Gailhanou, L. Raison, P. Panizza, H. Ushiki, E. Sellier, J. P. Delville, and M. H. Delville, “Smart control of monodisperse Stöber silica particles: effect of reactant addition rate on growth process.,” *Langmuir*, vol. 21, no. 4, pp. 1516–23, Feb. 2005.

[13] M. Marini, B. Pourabbas, F. Pilati, and P. Fabbri, “Functionally modified core-shell silica nanoparticles by one-pot synthesis,” *Colloids Surfaces A Physicochem. Eng. Asp.*, vol. 317, no. 1–3, pp. 473–481, Mar. 2008.

[14] S. Ghosh, S. K. Goswami, and L. J. Mathias, “Surface modification of nano-silica with amides and imides for use in polyester nanocomposites,” *J. Mater. Chem. A*, vol. 1, no. 19, p. 6073, 2013.

[15] W. Coene, G. Janssen, M. Op De Beeck, and D. Van Dyck, “Phase retrieval through focus variation for ultra-resolution in field-emission transmission electron microscopy,” *Phys. Rev. Lett.*, vol. 69, no. 26, pp. 3743–3746, 1992.

[16] D. H. W. Hans Kuhn, Horst-Dieter Försterling, *Principles of Physical Chemistry*. New Jersey: John Wiley & Sons, 2009.

[17] B. J. Berne and R. Pecora, *Dynamic Light Scattering: With Applications to Chemistry, Biology, and Physics*. Toronto: Courier Dover Publications, 2000.

[18] A. J. Milling, *Surface Characterization Methods: Principles, Techniques, and Applications*. CRC Press, 1999.

[19] C. Washington, *Particle Size Analysis In Pharmaceutics And Other Industries: Theory And Practice*. CRC Press, 2005.

[20] G. Dunderdale, S. Ebbens, P. Fairclough, and J. Howse, “Importance of particle tracking and calculating the mean-squared displacement in distinguishing nanopropulsion from other processes.,” *Langmuir*, vol. 28, no. 30, pp. 10997–1006, Jul. 2012.

[21] J. Howse, R. Jones, A. Ryan, T. Gough, R. Vafabakhsh, and R. Golestanian, “Self-Motile Colloidal Particles: From Directed Propulsion to Random Walk,” *Phys. Rev. Lett.*, vol. 99, no. 4, p. 048102, Jul. 2007.

Chapter 3:

Influence of the inactive hemisphere on the velocity of active Janus colloids.

3.1 Introduction

Golestanian described mathematically the influence on the motility, of not only the catalytic side of self-motile Janus particles but also the non-reactive hemisphere[1]. Based upon the theory that the displacement of the colloid is caused by self-generated fluid motion, it is argued that interaction between the solvent and the inert hemisphere will affect the mobility of the fluid at short ranges and therefore affects the slip velocity[1]. The relationship between fluid mobility and slip velocity is given below in Equation 3.1 where for a given position on the surface (R_s), V_s is the slip velocity, μ is the surface fluid mobility, I is the identity tensor, n is the local normal to the surface and ∇c is the solute concentration gradient.

$$\boldsymbol{V_s}(\boldsymbol{R_s}) = \mu(\boldsymbol{R_s})(\boldsymbol{I} - \boldsymbol{nn}).\boldsymbol{\nabla c}(\boldsymbol{R_s})$$

Equation 3.1

For simplicity it can be considered simply as the slip velocity ($V_s(R_s)$) is proportional to the mobility ($\mu(R_s)$), Equation 3.2.

$$\boldsymbol{V_s}(\boldsymbol{R_s}) \propto \mu(\boldsymbol{R_s})$$

Equation 3.2

It is also stated that an asymmetric distribution of the slip velocity can influence or even induce velocity of a self-motile particle. Golestanian describes a theoretical particle where catalytic activity is symmetrically located around the equator of a spherical particle, forces generated should be equal and opposite creating no net movement, however in the described system the non-active sides of the particle show asymmetry in the surface-fluid mobility (μ), this generates a net movement in the slip velocity and thus net movement in drift velocity[1].

Here, to investigate the effect of the inactive side properties experimentally, surface hydrophobicity is altered by functionalization with hydrophobic silanes. This modification has the potential to also alter the zeta potential of the inactive face, potentially resulting in a change to the behaviour of ions around the particle. This provides a mechanism to possibly influence diffusiophoretic effects.

3.2 Experimental

3.2.1 Materials

Tetraethyl orthosilane (TEOS, 98%), Ammonia (25% wt), 2-propanol solvent (99.8 %), ethanol (99.8 %), hexadecyltrimethoxy silane (HDTMS, ≥85 %) and toluene (99.8%), were purchased from Sigma Aldrich. perfluorooctyltriethoxy silane (PFOTMS, 98 %), (3-aminopropyl)triethoxysilane (APTES, 97 %) were bought from Alfa Aesar.

3.2.2 Colloid Synthesis

Silica micro-spheres were synthesised by the general method described by Wang et al. and influenced by Nozawa et al. [2][3]. All chemicals used were supplied by Sigma-Aldrich unless otherwise stated.

Using constant concentrations based on total volume (100ml) of the silica precursor TEOS (98.0 %), the catalyst ammonium hydroxide (25.0 %) and water in 2-propanol solvent (99.8 %), and a constant temperature of 4 ^{o}C, TEOS (diluted in 2-propanol to 50 % by volume) was continuously drop added by an Aladdin syringe pump (model NE-1000). Addition rates of 2.5, 5 and 10 ml per hour were investigated. The solutions were magnetically stirred throughout the duration of the TEOS addition.

Each sample was left stirring for a further 4 hours post completed addition of the TEOS solution to allow the reaction to complete.

After this time the samples were centrifuged using an Eppendorf centrifuge (model 5810) at 3100 g for 10 minutes. The supernatant was removed and the samples were washed by centrifugation and decantation, 3 times in ethanol (99.8 %) to remove any unreacted TEOS, and then washed to neutrality using distilled water. Particles were sonnicated using an Eumax sonnicator (UD50SH, 50 watt power output), for 15 minutes to re-disperse in solution before each centrifugation.

After washing to neutrality the particles were re-washed twice in ethanol to remove water and finally the particles dried in a drying oven at 60 °C overnight.

3.2.3 Surface functionalization

Surface functionalization was achieved via the grafting method as described in chapter 1.

Synthesised silica (0.01 g) was sonnicated in toluene (50 ml) for 30 minutes in an attempt to maximise available surface area by dispersing colloidal agglomerates. Selected functional silane agents were then added in excess (0.2 ml). The three silanes separately used to functionalise the colloids are, hexadecyltrimethoxy silane (HDTMS, ≥85 %), perfluorooctyltriethoxy silane (PFOTMS, 98 %) and (3-aminopropyl)triethoxysilane (APTES, 97 %, supplied by Alfa Aesar), represented in Figure 3.1, a. b. and c. respectively.

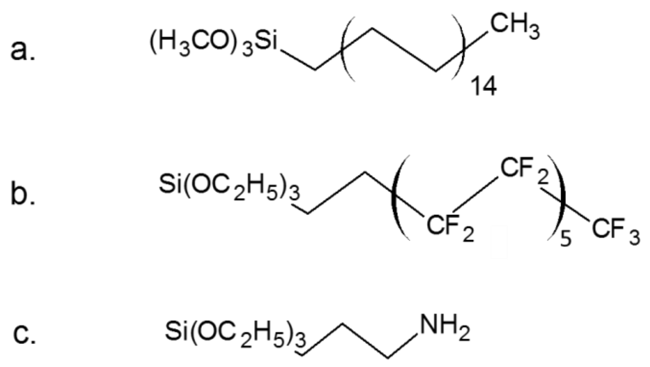

Figure 3.1 Molecular structure for a. Hexadecyltrimethoxy silane, b. Perfluorooctyltriethoxysilane, and c. (3-Aminopropyl) triethoxysilane

The solutions were refluxed gently for 6-12 hours, the times chosen based on contact angle measurements on modified glass slides using a goiniometer tensiometer (see section 3.3.2). After completion the silica colloids were separated from the toluene solution by centrifugation at 3100 g for 10 minutes and the washing procedure was repeated with ethanol three times to remove unreacted silanes.

The functionalised silica was removed from ethanol by centrifugation and dried at 60°C overnight.

3.2.4 Self-motile particle synthesis.

Glass slides were cleaned firstly using Decon 90 (1 % solution) followed by deionised water and finally cleaned by oxygen plasma using a (Diener electronic, model-Zepto) for 15 minutes. Surface functionalised silica microspheres were sparsely dispersed onto the cleaned slides by spin coating. A 70 µL volume of dilute suspensions of the unmodified or silanized silica colloids in ethanol was slowly dropped on to a rotating glass substrate, using a Laurell Spin Coater (Model WS-400BZ-6NPP/LITE) at 2000 RPM over 30 seconds.

Janus functionality was added to the chemically modified silica through e-beam evaporation of platinum metal (99.99%) by use of a Moorfield thin film evaporator. The spun coat slides were positioned above the source metal so the particles are in the line of sight as shown in Figure 3.2. As stated in section 2.3 the position of the slides relative to the source material is important due to a slight radial variation in thickness. In order to allow comparisons between surface functionalities, each set of surface modified particles was paired with an unmodified sample which was placed symmetrically within the evaporator (paired A to B). Given the symmetric distribution of metal deposition, the paired samples should be exposed to the same metal coverage. Approximately 10 nm of platinum was deposited on the surface (value given by the QCM).

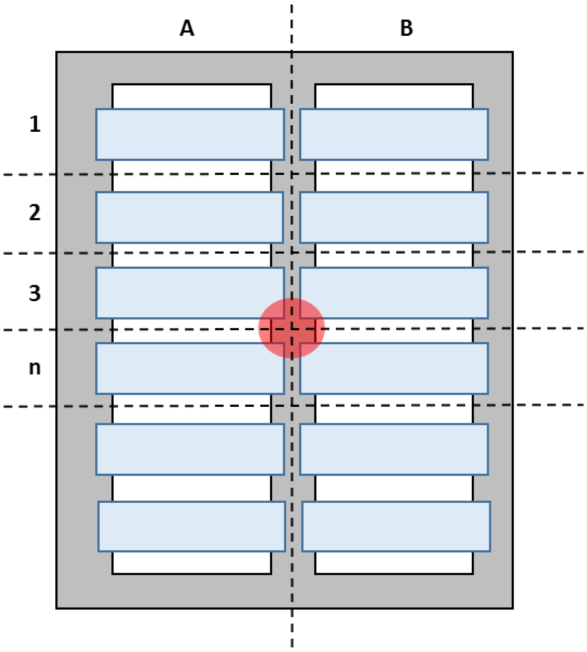

Figure 3.2 Sample holder for evaporator, top down view. Red circle indicates Pt source through the z-axis. Holder is divided by rows and columns, samples to be compared are paired by row position (A and B) of row position x.

3.2.5 Particle tracking

Pt coated particles were removed from the slides using wetted lens tissue to scrape the surface. The lens tissue was then submerged in DI water (1.1 ml) and sonnicated for 5 seconds to disperse the particles. Of this solution, 1 ml was transferred to a clean vessel and hydrogen peroxide (30% w/w) added to make a 15 % H_2O_2 solution.

The 15 % H_2O_2 solution was sonnicated for 5 minutes and allowed to stand for a further 25 minutes as it has been shown that the reaction rate shows an initial increase before plateauing to a constant. This step is important in keeping particle velocities time independent.

DI water was added to dilute the solution to 10 % H_2O_2 and transferred to a cuvette cleaned by oxygen plasma.

Observation and recording of self-motile particles was performed using a Pixelink camera (PL-B742F) attached to an inverted microscope (Nikon eclipse TS-100). All recordings were taken at 30 frames per second unless otherwise stated. During recording the z focus of the microscope was changed to keep the particles in focus but the x,y coordinates were kept static through the duration of each recording.

Analysis of the recorded tracks was performed using a LabView produced VI created by Dr's Stephen Ebbens and Jonathan Howse as stated in chapter 2.

3.3 Results and Discussion

3.3.1 Synthesised silica

The size of synthesised silica was measured using the Nanosight LM10 and analysed visually by SEM.

Results presented below in Figure 3.3 show the size of silica colloids synthesised with variable feed rate of diluted TEOS as described in section 3.2 with final volumes of 2-Propanol (29.2 ml), H_2O (6.45 ml), NH_3 (25 %wt, 0.527 ml) and TEOS (13.83 ml).

The results show an inverse proportional relationship between feed-rate and size of the resulting silica colloids which is in agreement with work done by Nozawa et al [3]. It is interesting to note the relative standard deviation remains around 20% irrespective of feed-rate.

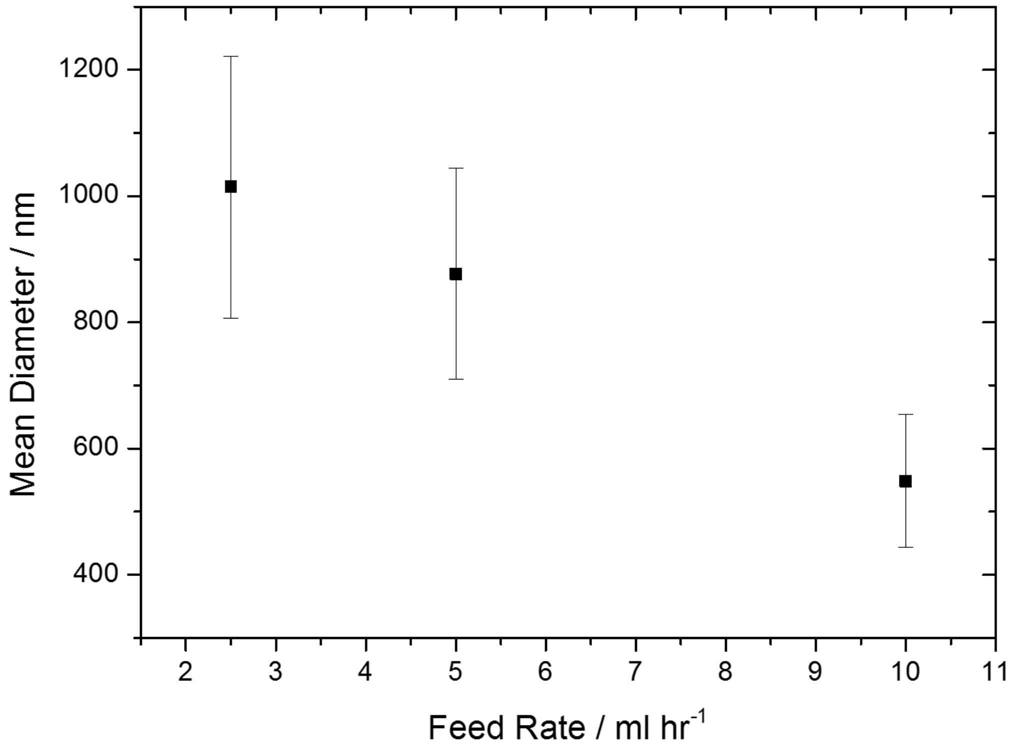

Figure 3.3 **Feed rate of TEOS and resulting mean diameter. Feed rates of 10, 5 and 2.5 ml per hour give mean diameters of 549.6, 876.8 and 1014.4 nm respectively. Their respective relative standard deviations are ±19.1, ±19.1 and ±20.5 %**

Silica colloids synthesised at a TEOS feed rate of 2.5 ml hr^{-1}, were of an ideal size for optical tracking and a tolerable size dispersity for use in the synthesis of self-motile particles. The full frequency distribution chart is shown in Figure 3.4.

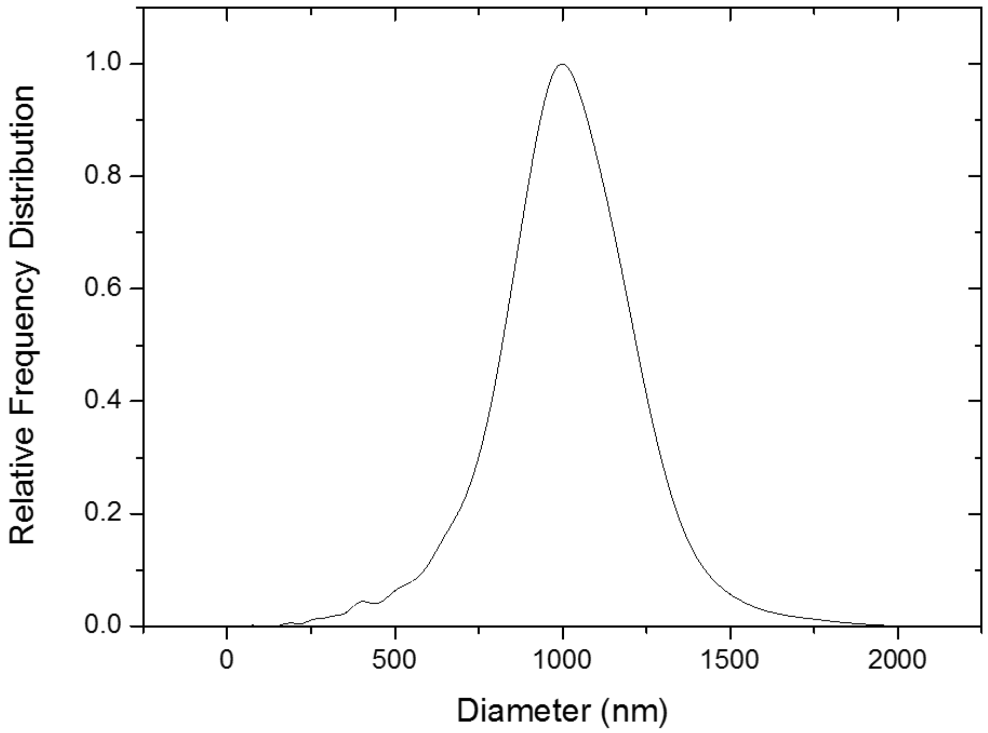

Figure 3.4 **Relative diameter frequency distribution of silica colloids produced by TEOS addition feed rate of 2.5 ml hr^{-1} by Nanosight analysis, result displayed is the average of 3 concurrent results. Mean diameter is reported as 1014 ± 104 nm**

Samples were also observed using a scanning electron microscope (SEM, JEOL, JSM-6010LA). SEM results (Figure 3.5) confirmed visually that the 1 µm colloids synthesised by TEOS feed rate of 2.5 ml hr^{-1} were indeed of a narrow size-distribution. Furthermore the particle morphology was shown to be consistently spherical with very low numbers of anomalous shapes (such as dimers).

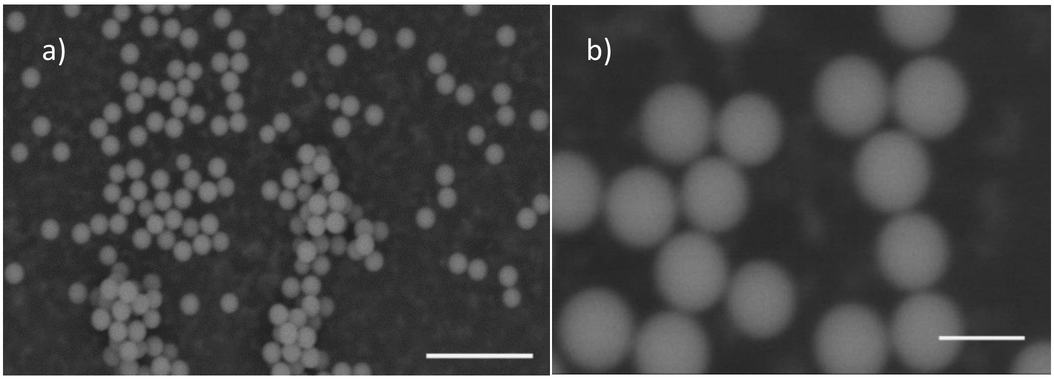

Figure 3.5 SEM of silica produced at TEOS feed rate of 2.5 ml hr^{-1} using back scattered electron imaging. Scale bars represent 5000 and 1000 nm for a. and b. respectively.

3.3.2 Chemical modification

Hexadecyltrimethoxysilane (HD) grafting on a silica surface increases hydrophobicity due to the addition of long aliphatic chains on the surface. To show this hydrophobisation and chart its progression, glass coverslips were cleaned by oxygen plasma treatment for 15 minutes and modified with HDTMS by refluxing for varied times at consistent silane concentration revealed the grafting process is relatively quick. By measuring the contact angle of water on the HDTMS hydrophobised surface against reflux time and assuming the point of plateaued contact angle represents the completed reaction, it is seen that the reaction was largely completed by 3 hours and a maximum contact angle of 100^{o} was reached after 6 hours with no significant change seen from 6 to 12 hours. Results from contact angle measurements are shown in Figure 3.6 and Figure 3.7

The reaction time at which contact angle no longer increases was used to determine the optimum reaction length for the colloids to be treated.

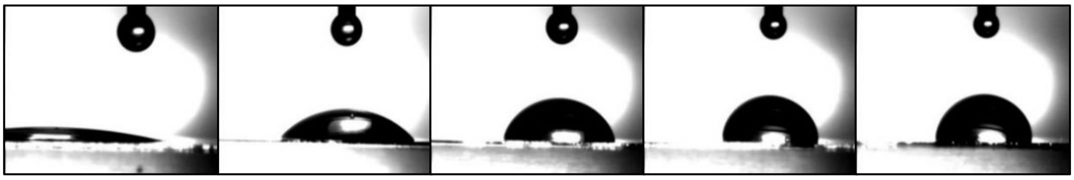

Figure 3.6 Contact angle measurements of DI water on glass slides refluxed in toluene with HDTMS for 0 (untreated), 0.5, 3, 6 and 12 hours from left to right.

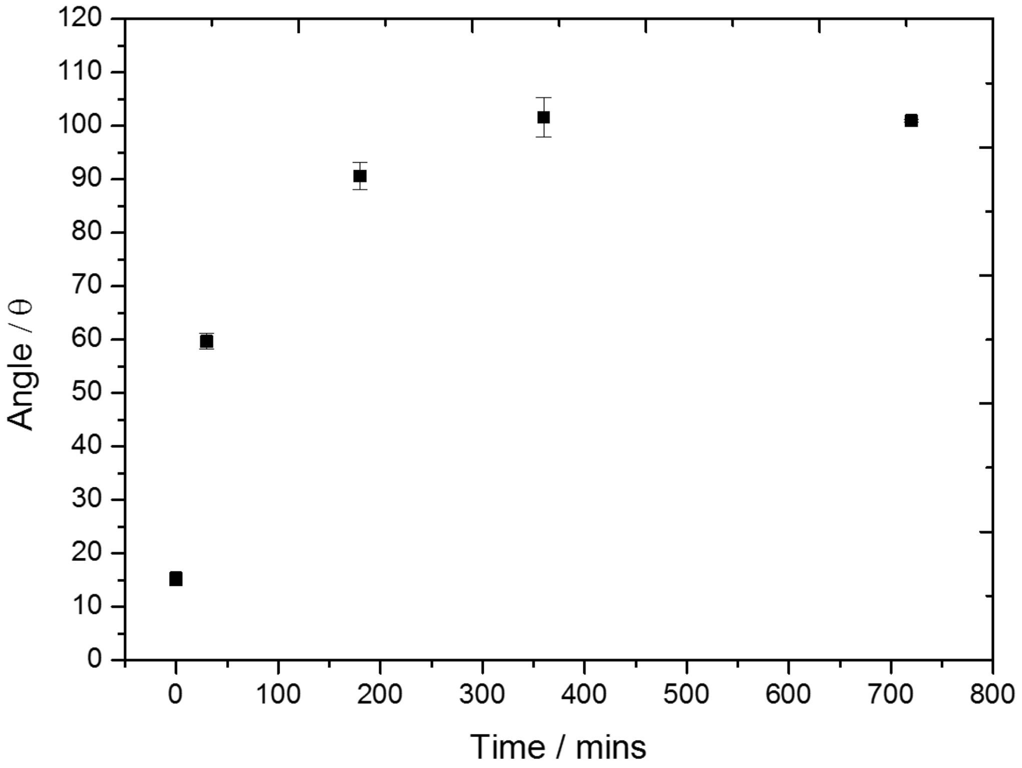

Figure 3.**7** contact angle measurements of DI water on glass slides refluxed in toluene with HDTMS for 0 (untreated), 0.5, 3, 6 and 12 hours. Showing contact angles of **15.4°, 59.7°, 90.5°, 101.6° and 100.9° θ.**

The synthesised 1 µm diameter silica spheres refluxed in toluene with HDTMS or PFOTMS silanes for 6 hours or longer, showed hydrophobic behaviour and could not be dispersed into DI water even with sonication. APS modified silica was still dispersible in DI water.

Direct quantification of contact angles on the silanized colloids was deemed impractical due to the inherent roughness of even planar, 2D colloidal crystals. Rough surfaces allow different wetting states, from the complete wetting Wenzel state for hydrophilic surfaces, to the partial wetting Cassie-Baxter state which incorporates tapped air pockets and minimises contact with the substrate. These two states affect the hydrophobicity by changing the percentage contact between the liquid and solid phase boundary[4]. Published reports place Stober prepared silica colloids with surface roughness in the order of 5-10 nm, which we can consider smooth for the purpose of contact angle measurements[5].

Contact angle for glass slides prepared under the same conditions as the colloids are presented in Figure 3.8 to offer comparative hydrophobicities on flat, smooth substrates. Contact angles were found to be 10.2° (± 4.2°), 47.7° (± 9.4), 77.0° (± 3.0°), 100.9° (± 0.2°) for unmodified, APS, PFO and HD modified surfaces respectively.

The contact angles for aminopropyl silane (APS) modified surfaces fit closely with literature reported values for APS coatings. The contact angle measurements for hexadecyl silane correlate with similar long alkyl functionalisations[6][7]. The perfluorooctyl trimethoxy silane (PFO) modified surface was however expected to produce larger contact angles due to the low surface energy of fluorinated alkanes and literature contact angle values reported to be as high as 110^{o} for flat substrates [8]. This would suggest an incomplete surface coverage of the PFO silane.

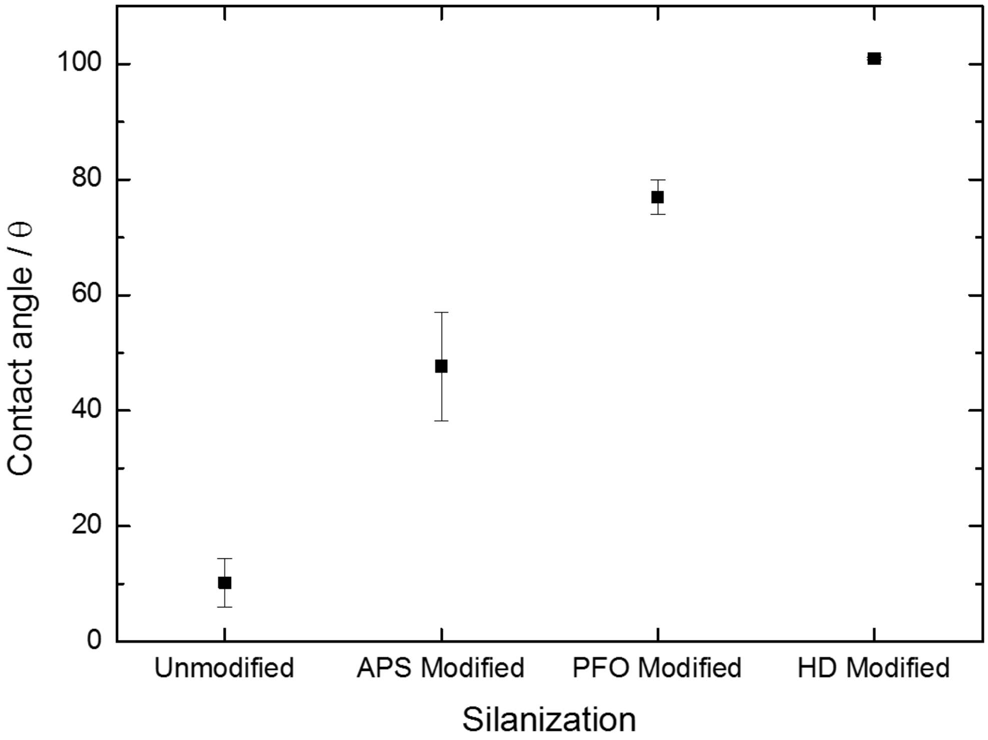

Figure 3.8 Contact angles measured on glass substrates for given silanization treatments after 6 hours of reflux.

3.3.3 Motion characterisation

Final platinum coverage for each set was recorded as 10.3 nm, 10.6 nm and 10.2 nm for APS, HD and PFO modified colloids respectively along with their respective unmodified control which were coated simultaneously. 3 sets of at least 30 tracks were recorded for each silanization analysis. Velocities found from analysis of the MSD as discussed in chapter 2, are presented below in Figure 3.9

For APS modified active colloids in 10 % wt/wt hydrogen peroxide the average velocity of 90 tracks is 5.60 (±0.09) µm s^{-1} and for the unmodied counterpart 5.2 (±0.5) µm s^{-1}

For HD modified active colloids in 10% wt/wt hydrogen peroxide the average velocity of 90 tracks is 6.3 (±0.1) µm s^{-1} and for the unmodied counterpart 4.3 (±0.4) µm s^{-1}

For PFO modified active colloids in 10% wt/wt hydrogen peroxide the average velocity of 90 tracks is 5.3 (±0.4) µm s^{-1} and for the unmodified counterpart 4.9 (±0.7) µm s^{-1}

A t-test with a null hypothesis (H_0) of there being no difference between the unmodified and modified pair is applied to assess the significance of the difference between the modified and unmodified pairs, presented below in Table 3.1. The t-values p-values of <0.1% in each case, we therefore reject the null hypothesis. The silanization is subsequently shown to change the average velocity by a small but statistically significant margin.

Results from the HDTMS modified self-motile particles showed the greatest difference between the hydrophobised silica and the unmodified silica with the hydrophobic surfaces resulting in a higher velocity in the order of 2 µm s^{-1}.

Table 3.1. Students' t-test between surface modified active colloids and their unmodified counterpart

	APS	HD	PFO
$\chi 1$	5.15	4.28	4.87
$\chi 2$	5.60	6.31	5.33
$\Delta\chi$	0.45	2.03	0.46
MSD	0.13	0.08	0.28
$\sqrt{\frac{2MSD}{n}}$	0.054	0.043	0.079
t	8.34	46.95	5.84
dof	178	178	178
p-value	<0.0001	<0.0001	<0.0001
H_0	Rejected	Rejected	Rejected

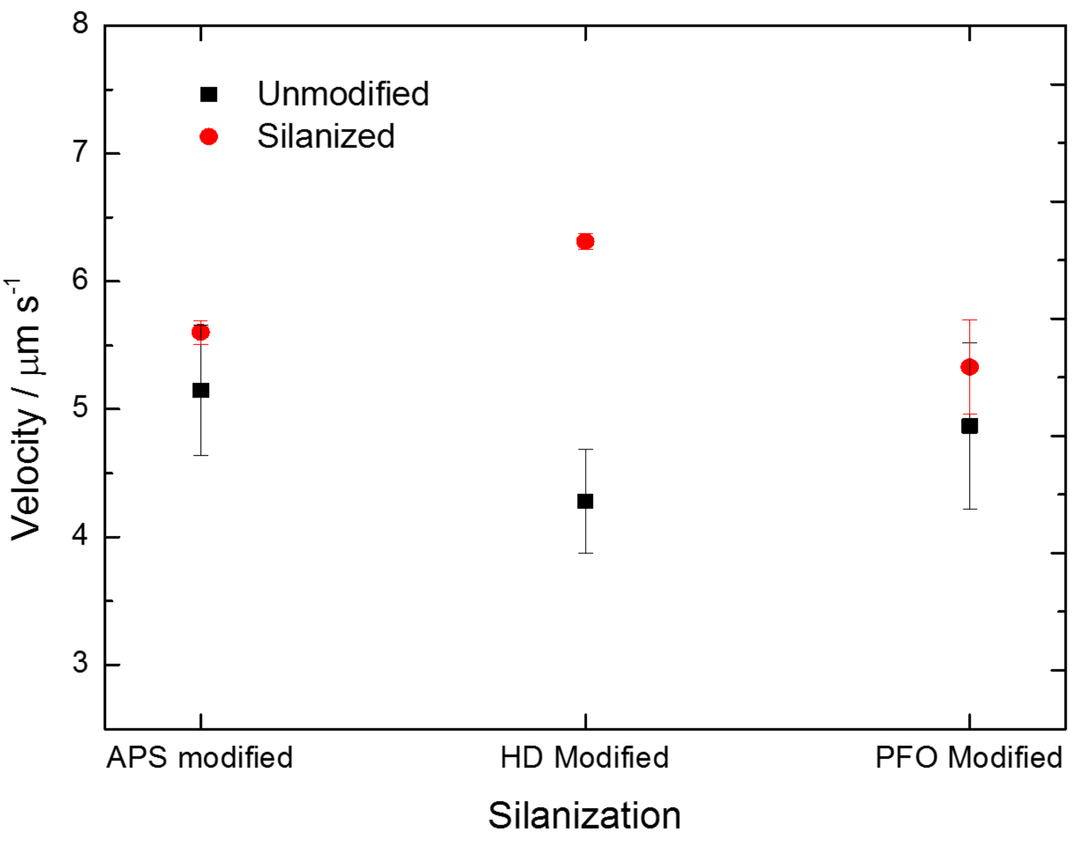

Figure 3.9 Average velocity for populations of active colloids

Confirmation of the inactive hemisphere having a statistically significant effect on the velocity reveals insights in to the mechanism of phoretic motion. Proposed models based solely on force imbalances, such as osmotic pressure[9] or nanobubbles[10] which do not account for the influence of the inactive hemisphere, can be considered at the very least incomplete.

To discern the nature of this increase in velocity, the velocity was plotted against two of the physical properties expected to be changed through Silanization treatment – hydrophobicity and zeta potential.

The relationship between hydrophobicity and velocity is plotted in Figure 3.10. Velocity appears to show weak positive correlation with increasing hydrophobicity. Such a relationship aligns itself with the self-generated fluid flow theories which allow for an interaction between the fluid and the inactive face of the active colloids, such as the theories proposed by Jülicher and Prost for diffusiophoretic models[11] and electrophoretic proton pumping by Ebbens, et al[12] as discussed in chapter 1.

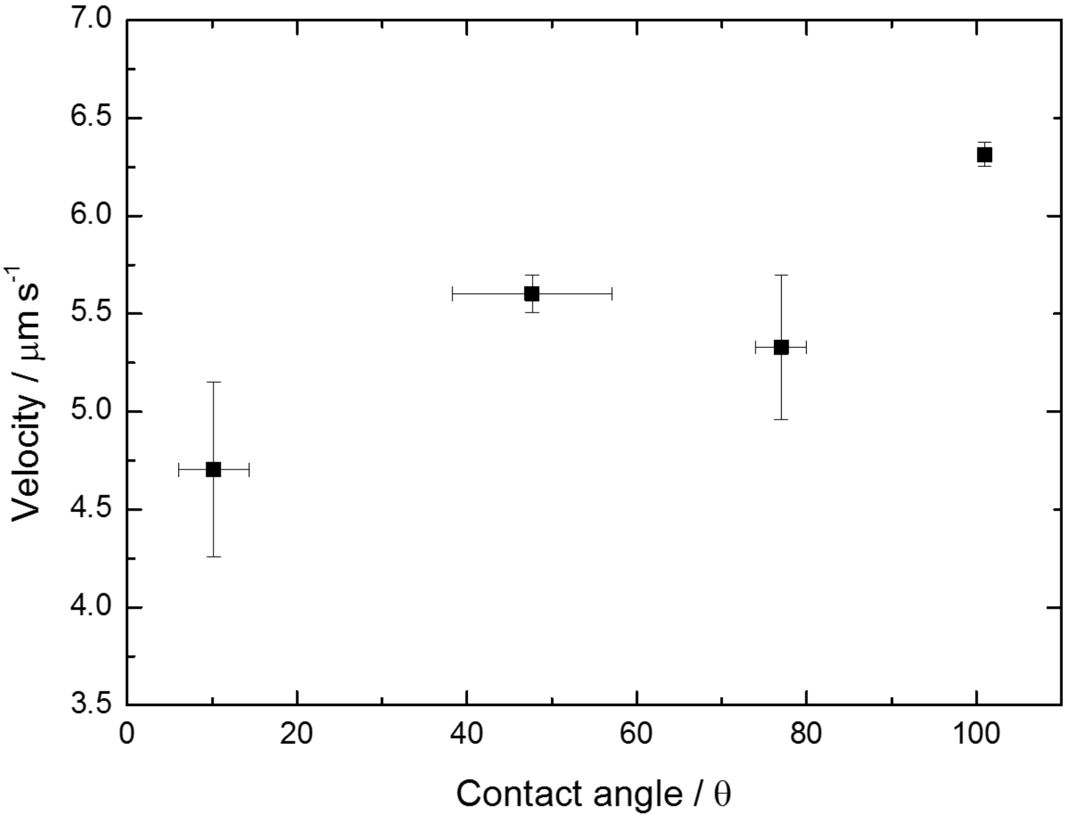

Figure 3.10. Average velocity plotted against their respective contact angle

The analysis of zeta potential for the base colloid measured in 10mM KCl, against velocity of the respective active colloid is given in Figure 3.11, reveals no obvious trend. HD and PFO modified silica colloids are suspected to have zeta potential close to 0 due to their non-interaction with water but cannot be directly measured as they could not be dispersed in the aqueous media at concentrations required for zeta potential analysis. However both show significantly different velocity profiles.

That velocity and zeta potential show no connection is of interest in the discussion of the mechanism for self-phoretic motion. Particularly, arguments for phoretic motion arising from self-electrophoresis or self-generated dipoles where charged species are 'pumped' across the colloidal surface are difficult to reason why zeta potential would have no effect on the proton flow as described by Ebbens et,al[12]. As zeta potential is a description of the electro kinetic potential at the slipping plane of the colloid, it would stand to reason that it would directly influence the charge density at the slip plane and interaction strength between the colloid and proton flow. These results indicate that the electrostatic potential does not significantly affect the fluid flow at the slip plane.

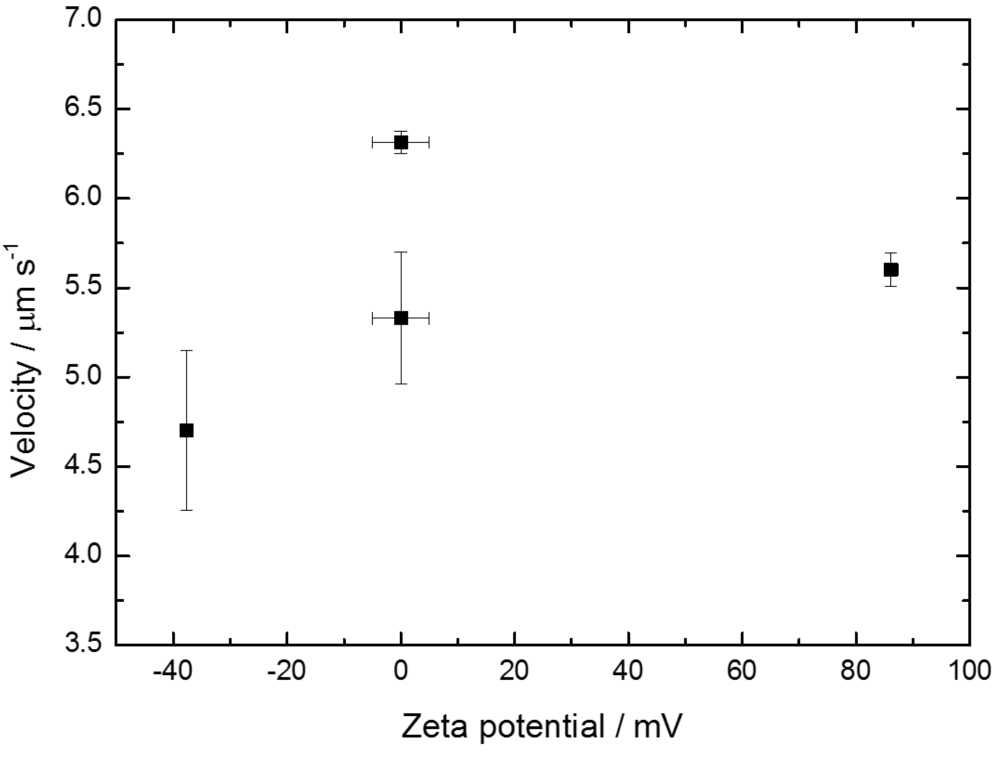

Figure 3.11 Average velocity plotted against their respective zeta potential.

3.4 Conclusion

It came to attention during this piece of work, that a paper by Manjare et al. was published in February 2014 on the effects of hydrophocity affecting velocity [13]. The paper concerned similar effects to those reported here, and also found that hydrophobic self-motile particles showed an increased velocity compared to their hydrophilic counterparts. The work conducted here is consistent in this respect with Manjare's findings that increasing hydrophobicity increases velocity of active colloids. Manjare however argued that rather than being a mobility effect as Golestanian proposed, this effect is caused by enhanced catalysis resulting from increased oxygen diffusion around to the hydrophobic hemisphere[13].

While hydrophobicity of the inactive hemisphere has been shown to affect the velocity, the hydrophobicity in this study and that used by Manjare et al, is limited by the 'smooth' surface of the colloids. It would be interesting to investigate the effects of morphology of the inactive hemisphere.

It can be thought that a roughened hydrophobic surface would enhance the hydrophobicity in a Cassi-Baxter wetting system, minimising the friction and loss of slip velocity at the slip plane[14]. Importantly such a system would likely not affect the oxygen flux that Manjare proposed was the source of velocity increase allowing the slip and oxygen flux to be isolated, quantifiable variables.

Few studies have examined the effect of surface morphology on stokes drag, an opportunity is presented here to investigate the comparison on surface roughness in fully wetting states on the resulting turbulence at the slipping plane[15].

Since the link between hydrophobicity and velocity has been shown it opens the possibility of utilising the effect for 'smart' behaviour. A change in hydrophobicity linked to an environmental stimulus would allow for autonomous modulation in velocity in response to 'programmed' triggers. Reports of pH responsive polymers able to switch between extremes of highly hydrophilic to highly hydrophobic would suit such a criteria[16]

3.5 References.

[1] R. Golestanian, T. B. Liverpool, and a Ajdari, “Designing phoretic micro- and nano-swimmers,” *New J. Phys.*, vol. 9, no. 5, pp. 126–126, May 2007.

[2] X.-D. Wang, Z.-X. Shen, T. Sang, X.-B. Cheng, M.-F. Li, L.-Y. Chen, and Z.-S. Wang, “Preparation of spherical silica particles by Stöber process with high concentration of tetra-ethyl-orthosilicate.,” *J. Colloid Interface Sci.*, vol. 341, no. 1, pp. 23–9, Jan. 2010.

[3] K. Nozawa, H. Gailhanou, L. Raison, P. Panizza, H. Ushiki, E. Sellier, J. P. Delville, and M. H. Delville, “Smart control of monodisperse Stöber silica particles: effect of reactant addition rate on growth process.,” *Langmuir*, vol. 21, no. 4, pp. 1516–23, Feb. 2005.

[4] A. Marmur, “The lotus effect: Superhydrophobicity and metastability,” *Langmuir*, vol. 20, no. 9, pp. 3517–3519, 2004.

[5] V. M. Masalov, N. S. Sukhinina, E. a Kudrenko, and G. a Emelchenko, “Mechanism of formation and nanostructure of Stöber silica particles.,” *Nanotechnology*, vol. 22, no. 27, p. 275718, 2011.

[6] X. Zeng, G. Xu, Y. Gao, and Y. An, “Surface Wettability of (3-Aminopropyl) triethoxysilane Self-Assembled Monolayers,” no. 100, pp. 450–454, 2010.

[7] J. W. Grate, M. G. Warner, J. W. Pittman, K. J. Dehoff, T. W. Wietsma, C. Zhang, and M. Oostrom, “Silane modification of glass and silica surfaces to obtain equally oil-wet surfaces in glass-covered silicon micromodel applications,” *Water Resour. Res.*, vol. 49, no. 8, pp. 4724–4729, Aug. 2013.

[8] A. Hozumi, K. Ushiyama, H. Sugimura, and O. Takai, “Fluoroalkylsilane monolayers formed by chemical vapor surface modification on hydroxylated oxide surfaces,” *Langmuir*, vol. 15, no. 22, pp. 7600–7604, 1999.

[9] U. M. Córdova-Figueroa and J. F. Brady, “Osmotic propulsion: The osmotic motor,” *Phys. Rev. Lett.*, vol. 100, no. 15, pp. 1–4, 2008.

[10] J. G. Gibbs and Y.-P. Zhao, “Autonomously motile catalytic nanomotors by bubble propulsion,” *Appl. Phys. Lett.*, vol. 94, no. 16, p. 163104, 2009.

[11] F. Jülicher and J. Prost, “Generic theory of colloidal transport,” *Eur. Phys. J. E*, vol. 29, no. 1, pp. 27–36, 2009.

[12] S. Ebbens, D. A. Gregory, G. Dunderdale, J. R. Howse, Y. Ibrahim, T. B. Liverpool, and R. Golestanian, “Electrokinetic Effects in Catalytic Pt-Insulator Janus Swimmers,” pp. 1–5, 2013.

[13] M. Manjare, Y. Ting Wu, B. Yang, and Y.-P. Zhao, “Hydrophobic catalytic Janus motors: Slip boundary condition and enhanced catalytic reaction rate,” *Appl. Phys. Lett.*, vol. 104, no. 5, p. 054102, Feb. 2014.

[14] C.-O. Ng and C. Y. Wang, "Effective slip for Stokes flow over a surface patterned with two- or three-dimensional protrusions," *Fluid Dyn. Res.*, vol. 43, no. 6, p. 65504, 2011.

[15] A. Md Rashedul Kabir, D. Inoue, Y. Kishimoto, J. Hotta, K. Sasaki, N. Kitamura, J. Ping Gong, H. Mayama, and A. Kakugo, "Drag force on micron-sized objects with different surface morphologies in a flow with a small Reynolds number," *Polym. J.*, vol. 47, no. December 2014, pp. 564–570, 2015.

[16] Q. Zhang, F. Xia, T. Sun, W. Song, T. Zhao, M. Liu, and L. Jiang, "Wettability switching between high hydrophilicity at low pH and high hydrophobicity at high pH on surface based on pH-responsive polymer.," *Chem. Commun. (Camb).*, no. 10, pp. 1199–1201, 2008.

Chapter 4:

Glancing angle deposition to control active layer shape

Sections of this chapter were successfully published in:

"Glancing angle metal evaporation synthesis of catalytic swimming Janus colloids with well defined angular velocity"

Archer, RJ. Campbell, AI. & Ebbens, SJ. SOFT MATTER, 11(34), 6872-6880 2015

4.1 Introduction

Potential applications for autonomous micron scale swimming devices include microfluidic transport[1][2]. For example the ability to selectively bind and transport cancer cells has been demonstrated[3], and drug delivery, where enhanced transport combined with smart release behaviours could improve active ingredient potency and selectivity[4]. Motivated by these goals, most current autonomous swimming devices have been designed to produce intrinsically linear trajectories within the constraints of Brownian rotational diffusion. For example, in the case of Janus colloids, catalytic decomposition results in propulsion orientated away from the active coated hemisphere[5], producing ballistic propulsion until Brownian rotational diffusion randomises orientation[6]. However, it has become clear that there are additional potential application areas that could be enabled by the ability to produce swimming devices with well-defined spiralling and spinning trajectories. Interest in micron scale spinning particles has led to a number of different systems such as magnetically driven rods[7] and light induced motile particles with geometry controlled circling trajectories[8]. As an example of the potential applications for rotating devices, micron sized spinning colloids have been shown to influence the directional growth of neurons in vitro[9], induce cell death by bursting lysosomes through the generation of shear forces[10], and enhance surface protein binding rates[11]. However, in each case these demonstrations required external actuation of the rotational behaviour by external magnetic and light fields generating localised heating. Additionally a range of proposals for the fundamental behaviour of rotationally propulsive colloids have been made including chiral diffusion[12] and reversal of rotation direction in confined geometry,[13] which have yet to be experimentally tested. An extra motivation for investigating autonomous rotation is provided by the potential for devices that can transition from linear running to rapid rotation to emulate the chemotaxis behaviour displayed by bacteria in order to respond to local stimuli gradients.[14] However, despite these potential benefits, modifying autonomous active colloids to impart controlled rotational behaviour has received very little attention. In some early reports, self-propulsive nanorods were observed to undergo tight rotations, however this was due to them becoming randomly stuck to substrate defects, and was not well controlled.[15] Ebbens et al also noted that agglomerated self-propulsive Janus colloid dimers would rotate with a frequency dependant on the relative cap orientation between Janus colloids[14]. The self-assembley process however resulted in random, uncontrolled dimer orientations leading to a distribution in rotational frequencies. A small degree of propulsive spin, not due to surface interactions, was also noted in the original report for hemispherical platinum coated Janus active colloids, and was suggested to be due to physical imperfections in the active cap, breaking to generate circling and spinning trajectories, however, no method to bias the random assembly process towards a particular range of spins was established[6].

Here, the lack of attention given to designing autonomous micro-swimming devices with well-defined rotational behaviour is addressed by demonstrating an approach that can systematically break the rotational symmetry of the hemispherical active layer in platinum coated Janus spheres. The hypothesis that this reduction in symmetry will imbalance the force generation in the resulting devices and produce a well-defined torque is tested. To break the cap symmetry the standard Janus swimmer manufacturing procedure where platinum is directionally evaporated from a normal angle onto Janus spheres sparsely distributed across a planar substrate is modified. Instead, a glancing angle metal evaporation technique developed by Pawar and Kretzschmar[16] is used. In this prior study, colloids were assembled into close packed colloidal crystals and exposed to a directional metal vapour from a well-defined glancing angle. In this arrangement, neighbouring colloids shadow one side of a given colloid, breaking the symmetry through the deposited hemisphere to a variable extent controlled by the glancing angle, allowing a high level of control over cap shape. This chapter shows that this method can impart a well-defined amount of rotational velocity to the trajectories of platinum coated Janus active colloids prepared in a similar manner.

4.2 Experimental

4.2.1 Materials.

Platinum wire of 0.25 mm (99.99%), ethanol (99.98%) and H_2O_2 (puriss grade, 30% w/w) were purchased from Sigma Aldrich. Carboxyl terminated polystyrene microspheres (1.9 µm, 4 % w/w in water) were bought from Invitrogen. All materials were used as received. Deionised (DI) water was obtained from an Elga Purelab Option filtration system (15 MΩ cm).

4.2.2 High density colloidal crystals.

Monolayers of hexagonaly close packed carboxyl terminated polystyrene microspheres were prepared by self-assembly at an air/water interface as described by Weekes et al[17]. Briefly, the stock solution of carboxyl terminated polystyrene microspheres was diluted with ethanol (1:1). The diluted solution was spread slowly across a glass slide partially submerged in DI water and angled at approximately 45° relative to the water surface. The diluted solution of carboxyl terminated polystyrene microspheres spreads down the slide to the meniscus of the DI water where upon they spread across the surface as a monolayer and assemble into the colloidal crystal hexagonal close pack array. These floating crystals are scooped up on to glass slides and left to dry under ambient conditions.

4.2.3 Low density colloid dispersion.

Low density, well separated arrangements of carboxyl terminated polystyrene microspheres were prepared by spin coating (2000 RPM) low concentration solutions of the stock bead solution, diluted with ethanol (1:4000), onto cleaned glass microscope slides.

4.2.4 Metal deposition.

Platinum metal was coated onto the prepared slides containing either high density colloidal crystals or low density spun coat microspheres, by e-beam evaporation of the source platinum metal using a Moorfield Minilab 80 e-beam evaporator under high vacuum, ($1x10^{-9}$ bar). Platinum films were deposited to an approximate thickness of 10 nm, measured using a quartz crystal monitor. E-beam evaporation under these conditions is highly directional and coats only by line of sight, therefore (for unshadowed colloidal particles) coats only the exposed hemisphere giving the desired Janus particles with catalytic activity. A full description of PVD is given in chapter 2 section 2.

4.2.5 Angle control.

Angles reported here are relative to the source metal with 0^o being perpendicular and 90^o being parallel to the path of the ejected metal vapour during e-beam evaporation. During e-beam evaporation the prepared samples of carboxyl terminated polystyrene microspheres on glass microscope slides are held at angles from 0 to 80^o. This is achieved through use of a purpose built microscope slide holder on a rotatable axis, held within a metal frame. The angle is set manually before loading into the vacuum chamber of the e-beam evaporator.

4.2.6 2D Tracking.

Platinum coated colloids were transferred to solution using damp lens tissue to physically rub the microscope slides, displacing the particles from the surface and into the tissue. The tissue is transferred into a small (ml) volume of DI water and shaken to release the Janus particles into solution. The solution is transferred to a clean vial without the tissue. An initial cleaning step is employed to remove contaminants from the platinum cap surface by the addition of hydrogen peroxide (1:1) to make a 15% w/w H_2O_2 solution, this solution is sonnicated in a sonic bath for 5 minutes and left to stand for a further 25 minutes after which the solution is diluted with additional DI water (2:1) to 10% w/w H_2O_2 in which the measurements will take place.

Tracking of the synthesised self-motile particle was performed using a Nikon eclipse inverted microscope fitted with a Pixelink PL-B742F camera. Videos of 1000 frames recorded at 33 fps at a resolution of 640x480 were taken of the swimming device in 10% H_2O_2 and the videos were analysed using custom built software based on LabVIEW vision assistant which gives frame by frame x,y coordinates of the swimming devices and their mean square displacements by time.

4.3 Results and Discussion

4.3.1 Structure analysis

Firstly the structure of the Janus spheres generated by glancing angle deposition were determined to verify the expected cap-asymmetry due to near neighbour shadowing has been achieved. Figure 4.1 shows schematically the expected outcomes for glancing angle deposition. As the schematic illustrates, a glancing angle is physically introduced by tilting a 2D colloidal crystals plane relative to the fixed directional evaporation source. For conventional normal deposition (glancing angle, $\theta=90^0$), no shadowing effects are expected, however when $\theta<90^0$, neighbouring colloids obstruct (shadows) the line of sight path of the metal coating in PVD Figure 4.1 (a). The degree of obstruction is proportional to the angle.

As a control experiment, to verify the reliance on a close packed colloidal crystal to control catalyst cap shape in the proposed way, glancing angle deposition for a sparse arrangement of colloids deposited by spin-coating. As shown in Figure 4.1 (b). Separated colloids, such as those deposited by spin coating from low volume fraction solutions, are not expected to be subject to the same shadowing effects and the full hemisphere will be coated regardless of θ.

Figure 4.1c shows schematically how obstruction of the path of the platinum vapour is expected to occur due to shadowing by neighbouring colloids, resulting in an asymmetrical distribution of metal across the coated surface and complex cap perimeters. It can be seen that the shape of the perimeter of the resulting cap will be also effected by the rotational orientation (crystal orientation angle, α) of the colloidal crystal with respect to the glancing angle tilt axis.

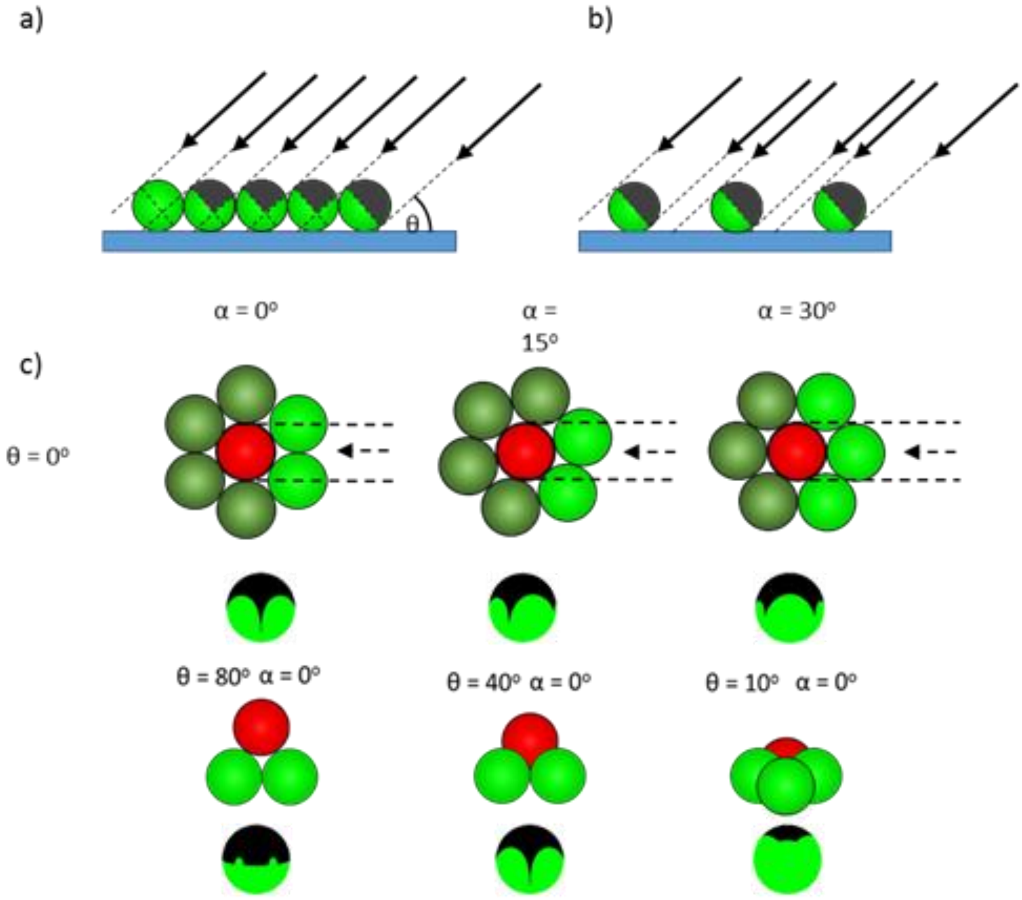

Figure 4.1 (a) Glancing angle evaporation onto a colloidal crystal modifies the cap shape as the glancing angle (Ө) is varied due to the potential for neighbouring colloids to shadow the line of sight path of the metal. (b) If colloidal coverage is sufficiently sparse, changing the glancing angle, θ, will not affect the deposited cap shape which will remain hemispherical. (c) Top section: At a fixed glancing angle, the orientation of the colloidal crystal (α) relative to the metal source will produce variations in the

deposited cap shape. The resulting deposited metal pattern on the red-sphere is shown below, light green spheres are responsible for the shadowing effects. Bottom section: The effect of varying glancing angle for a fixed crystal orientation is depicted. As the glancing angle is reduced, the patch coverage is reduced, and the perimeter shape is also altered

The colloidal surface coverage of the glass substrates was examined by optical microscopy. Figure 4.2(a) shows the colloidal spread resulting from the spin coating of dilute suspensions. The sparse colloidal spread was sufficient to give the spacing between the colloids, several times greater than their diameter. Very few incidents of colloids with direct ‘touching’ neighbours were observed, therefore satisfying the control criteria of eliminating the effects of shadowing.

High percentge coverage of close packed colloids were shown to be achieved by the self-assembly method described by Weekes et,al[17] The colloidal monolayer was produced in dimensions of several orders of magnitude greater than the colloid diameter (coverage typically between 1 to 2 cm^2). Figure 4.2(b) reveals the typical micro-structure of the colloidal crystals. While a high percentage of close packed colloids were achievable, long range ordering of crystalites however, were rare with the overall structure being poly-crystaline in structure. An important consequence of this is in lack of the control over the crystal orientation (α). Results from these self-assembled crystals would therefore represent an averaged α value.

Defect sites are also present, with minor random defects of missing colloids appearing as a small percentage of the structure, seen as bright dots where light transmits through. Larger defects occuring as tears in the structure as seen in Figure 4.2 (b) were also noted but were rare. Defect sites will each produce a number of unobstructed, unshadowed colloids. The number of colloids at a defect site compared to those in the continous array were considered acceptably small as a percentage.

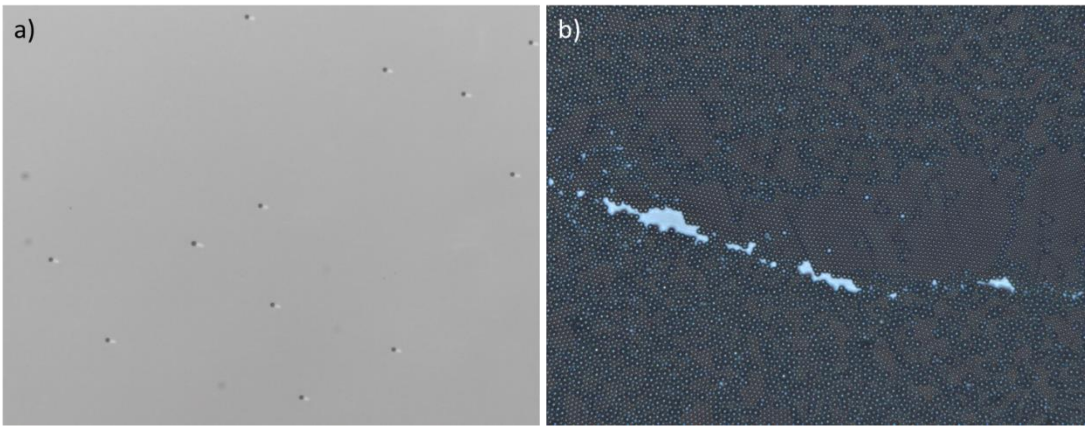

Figure 4.2. Microscopy images of 1.9 µm carboxylated latex colloids dispersed on to a glass substrate (a) sparsely via spin coating with low percentage coverage (b) close packed with a high percentage coverage.

The SEM images in Figure 4.3(a) confirm the expected symmetrical distribution of coated platinum for each particle in the ($\theta=90^0$) colloidal crystal when viewed from the top down. In these back scattered images, regions covered by platinum metal appear brighter than the uncoated silicon colloids. To further verify the perimeter shape of the cap, the contents of each colloidal crystal were dispersed into water, then, re-deposited and re-examined by SEM, to randomise the viewing angle. Figure 4.3(f) shows randomly orientated colloids from the ($\theta=0^0$) crystal, and for the indicated colloids lying “sideways” on a smooth equatorial cap boundary is observed.

Figure 4.3 (b-e) shows the effect of increasing the glancing angle viewed from the top down SEM images for colloidal crystals. As glancing angle increases, the bright contrast indicating the distribution of platinum metal across each colloid becomes visibly asymmetric, indicating more platinum has accumulated at one side of the colloid than the other. This asymmetry is aligned across the entire colloidal crystal (and does not rotate with the scan direction, ruling out charging artefacts), and is orientated along the tilt axis used to generate the glancing angle (marked by arrows). At higher glancing angles, the asymmetry is increasingly pronounced as more of the directional metal vapour is shadowed by a given colloids neighbours. While Figure 4.3(b-e) depicts single crystal regions of colloidal crystal, the colloidal crystal regions generated by the float method are polycrystalline over larger areas. When particles are re-suspended for swimming experiments, this will result in many different crystalline domains being sampled, leading to the crystal orientation angle being uncontrolled and randomised in this current experiment. Figure 4.3(g-j) show back scattered images for suspended and re-deposited colloids, allowing the perimeter of the cap to be clearly discerned. At the lowest glancing angle, 70^0, small deviations in the equatorial cap perimeter line are seen for some particles, where near neighbours have shadowed the metal deposition. Other particles lying at different randomised orientations display smooth equatorial perimeters. This is as expected, because, each individual Janus particle will have one side facing towards the metal source which is strongly shadowed by neighbouring colloids, whereas the other side of the caps shape is masked by the particle itself. As the glancing angle is increased, the deviations in perimeter on the side facing the evaporation source become more pronounced, however again some the smoother, trailing edge perimeter can be seen at other orientations. In summary, these images show that as glancing angle increases, increasing asymmetry is being introduced into the platinum cap, due to masking of near neighbours on one side of the deposited coating.

However, from a top down view, the visible portion of the hemisphere will decrease with increasing θ simply due to a shifting orientation of the coated hemisphere. Once removed from the slide the orientation of the cap would cease to be relative to the slide and therefore all active colloids prepared from spun coat samples would be expected to be equivalent in nature regardless of θ.

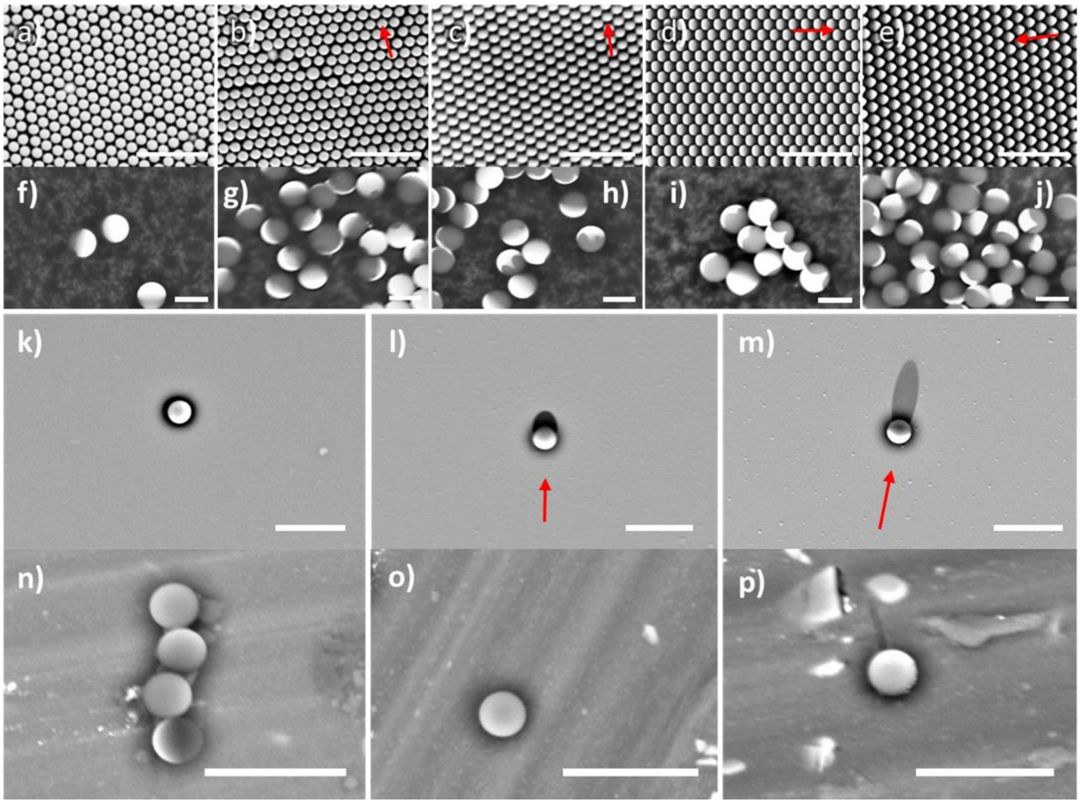

Figure 4.3 Backscattered SEM images following glancing angle platinum deposition onto a colloidal crystal of 1.9 µm diameter silica particles. (a-e), Pt coated colloidal crystals after evaporation at angles of 90°, 70°, 50°, 30° and 10°, (a-e) respectively where the scale bar represents 10 µm. Red arrows are used to mark the direction of the incoming platinum vapour where it was apparent. (F-j) colloids prepared at glancing angles 90°, 70°, 50°, 30° and 10° after dispersal and re-deposition of the colloidal crystals shown in (a-e) , the scale bars represent 2 µm. (k-m) show Pt coated colloids at glancing angles of 90°, 40° and 10° respectively for individual particles with no near neighbours (prepared by spin coating), the scale bars represents 5 µm.

4.3.2 Motion analysis

Initial qualitative observations of the Janus active colloids generated using this glancing angle colloidal deposition approach by suspension in 10 % H_2O_2 aqueous solutions, showed an obvious difference in behaviour, with increasing glancing angles introducing a very apparent increasing amount of spin to the propulsive trajectories. Frame by frame tracking of the position of the colloid in these videos was used to produce x y trajectory plots, with representative examples shown in Figure 4.4(a). For normal ($\theta=90^0$) deposition, the trajectories resemble those reported previously for similar sized Janus swimmer colloids, exhibiting enhanced motion significantly exceeding the displacements observed for unfuelled colloids in water. The trajectories show ballistic runs, followed by direction changes, which have been previously explained by the finding that propulsive thrust direction is correlated to swimmer orientation, subject to Brownian rotational diffusion[5]. However, as the glancing angle increases, a dramatic change in trajectory character is observed: increasingly tight spiralling is induced. This suggests that the structural asymmetry features introduced by shadowing effects are resulting in the introduction of increasing amounts of angular propulsive velocity. In contrast, the sparsely coated spin coated colloids do not show significant variation in trajectory as a function of glancing angle.

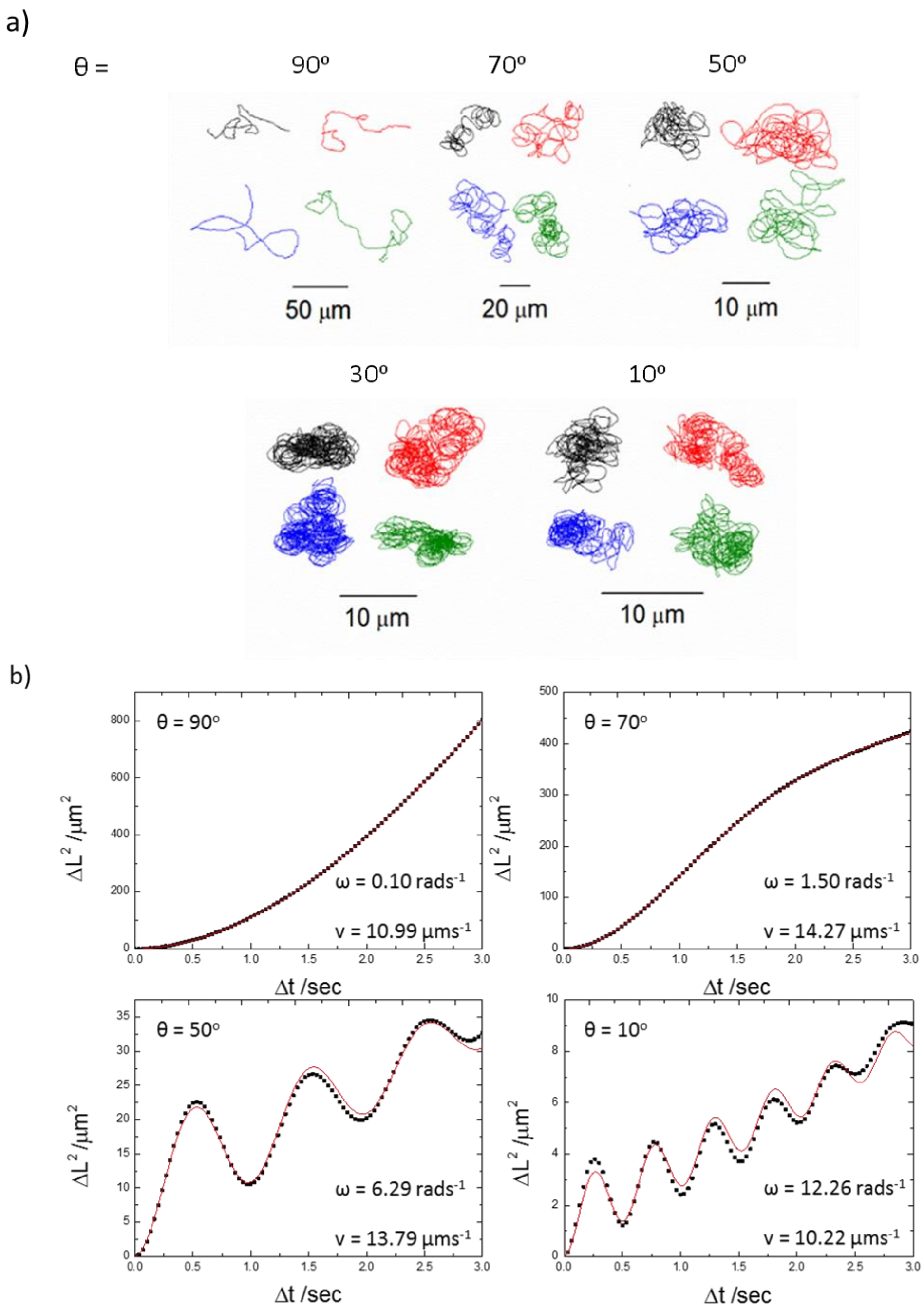

Figure 4.4 (a) Representative x y plot trajectories (30 seconds) for 1.9 μm diameter Janus colloids re-dispersed into 10 % H_2O_2 solutions after platinum evaporation onto a colloidal crystal at a range of glancing angles. (b) Representative MSD plots from Δt = 0.0 to 3.0 seconds for active colloids prepared from colloidal crystals at 90°, 70°, 50° and 10° θ, a-d respectively. Black points represent experimental data and the red line is generated from equation 1 to find ω and V

It has been previously shown that for the case of a freely diffusing colloid producing both angular and rotational velocity, mean squared displacements as a function of time step are given by Equation 4.1, containing the Brownian translational diffusion coefficient (D), and rotational diffusion constant (D_r) in addition to the translational (v) and the angular velocity (ω) which can be given by fitting a mathematical model described by equation 4.1 [18]. Therefore, to quantify both the angular velocity and the translational velocity, mean squared displacement (MSD) plots for each recorded trajectory were generated, with typical examples and associated fit and fit parameters displayed in Figure 4.4. For samples prepared by normal evaporation, MSD plots fits to Equation 4.1 with a ω value at or close to zero, reflecting that there are no driven rotational changes, and that MSD evolution is simply determined by the Brownian diffusion properties and translational velocity magnitude. However, as glancing angle increases, oscillations in the MSD are seen which increase in frequency, and are well fitted with increasing values of ω.

$$\Delta L^2(t) = 4Dt + \frac{2v^2 D_r t}{D_r^2 + \omega^2} + \frac{2v^2(\omega^2 - D_r^2)}{(D_r^2 + \omega^2)^2} + \frac{2v^2 e^{-D_r^2}}{(D_r^2 + \omega^2)}\left[(D_r^2 - \omega^2)cos \cdot \omega t - 2\omega D_r sin \cdot \omega t\right]$$

Equation 4.1

V and ω were determined using this method for many trajectories (3 sets of 30 tracks for the colloidal crystals and 3 sets of 20 tracks for the spun coat samples at each glancing angle), and the average values are shown in Figure 4.5 and Figure 4.6 respectively. The average translational velocity for colloidal crystal prepared active colloids is 16.48 (±4.40) μms^{-1}, while sparse coverage spin coated prepared samples give a mean value of 12.28 (±0.69) $\mu m\ s^{-1}$. For the spun coat samples there is a tight spread in these velocity values which appear to be unaffected by glancing angle. However, while some of the glancing angle depositions onto colloidal crystals produce similar translational velocities to the sparse coverage set, significantly higher velocities are observed for some samples, particularly for theta in the range 40°-20°. Considering average rotational velocity's, Figure 4.6, an increase in ω with glancing angle from 1.16 to 16.46 rads^{-1} (0.25 to 2.62 Hz) peaking at θ=20 ^{o} is observed. These maximal ω values are considerable higher than those previously achieved by the self-assembly of symmetrically coated Janus units [18]. Spun coat prepared samples give a mean ω of 1.32 (±0.28) rads^{-1} (0.21 Hz) and the glancing angle makes no significant change to ω. Due to the variations in translational velocity as a function of glancing angle for colloidal crystal samples, it is instructive to also consider the derived parameter, $\mathrm{R} = \frac{\omega}{v}$. R represents the number of radians turned per translational distance travelled and gives a measure of how tightly spinning the trajectory of an average colloid prepared under a give condition is, irrespective of the absolute magnitudes of ω and v. Figure 4.7, shows that R increases monotonically with θ, whereas for spun coat samples there is no link between R and θ. This demonstrates the potential to accurately tune the degree of spiralling present in a given trajectory by altering the glancing angle during colloidal deposition. Further to this, Figure 4.8 shows the frequency distribution of the R values showing that while there is a distribution the peaks are clearly separated, suggesting a high level of controllability.

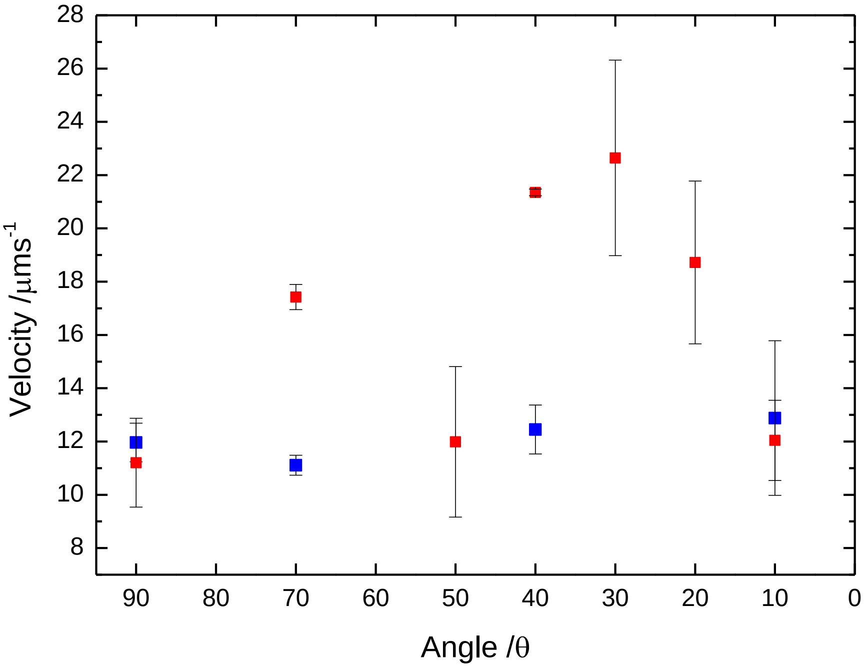

Figure 4.5 Velocity (v) profile of active colloids prepared from colloidal crystals (red) and sparsely spun coat colloids (blue) for a range of angles from θ =90° to 10°.

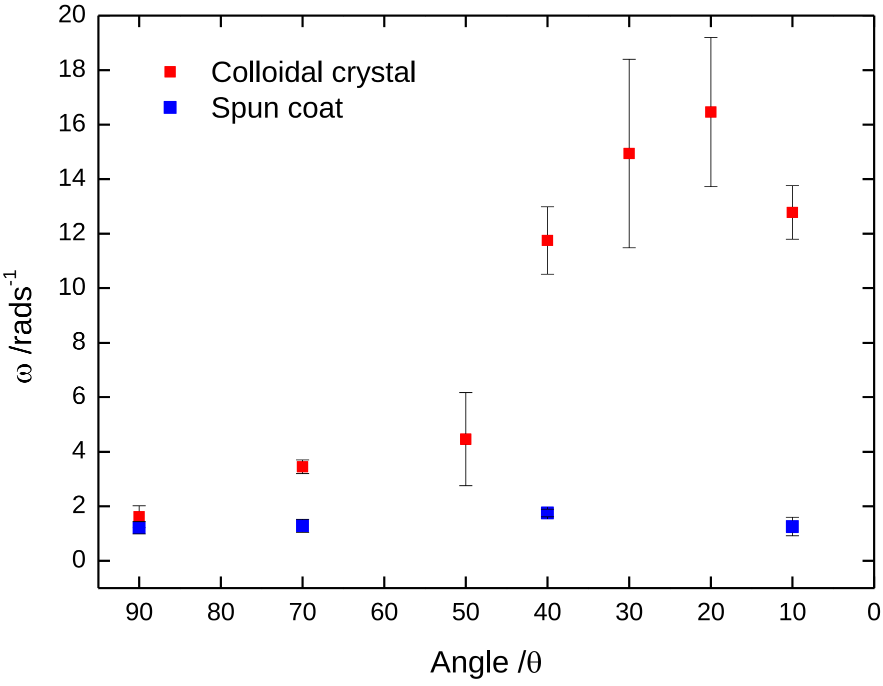

Figure 4.6 Angular velocity (ω) profile of active colloids prepared from colloidal crystals (red) and sparsely spun coat colloids (blue) for a range of angles from θ= 0° to 80°.

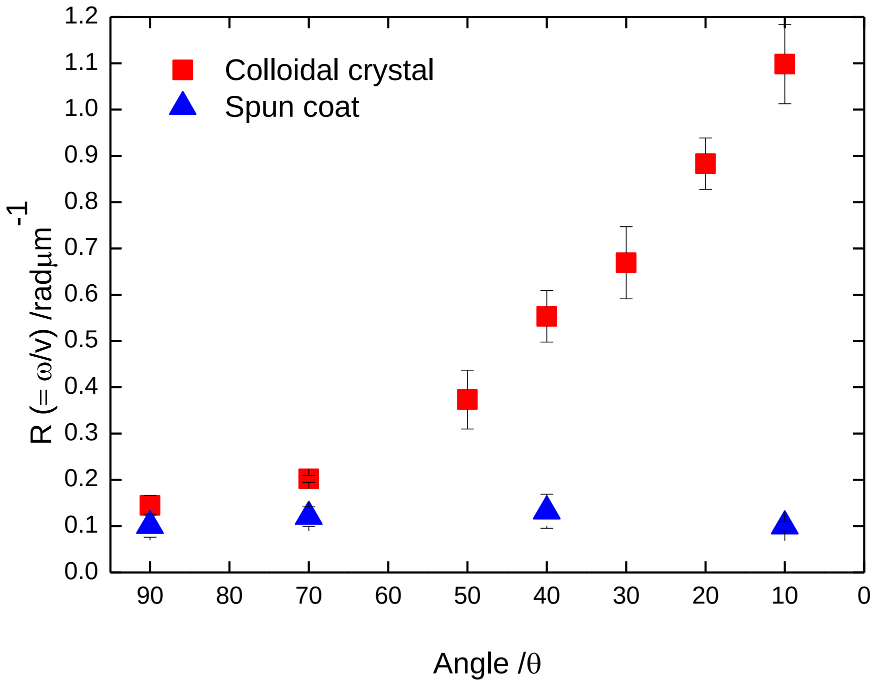

Figure 4.7 Ratio between ω and v for active colloids prepared from colloidal crystals (red) and sparsely spun coat colloids (blue) for a range of angles from θ= 90° to 10°

Figure 4.9 shows a detailed R value distribution comparison for active colloids prepared from spin coating and colloidal crystals both at 90° glancing angle. This data reveals that active clloids prepared by spin coating have slightly lower R values, indicating more persistent trajectories, compared to those prepared from a colloidal crystal, despite the equivalence in coating direction. In any case, both samples possess appreciable angular rotation (1 rad s^{-1}) suggesting that more precise control of cap asymmetry may be required to access truly Brownian rotation limited trajectories.

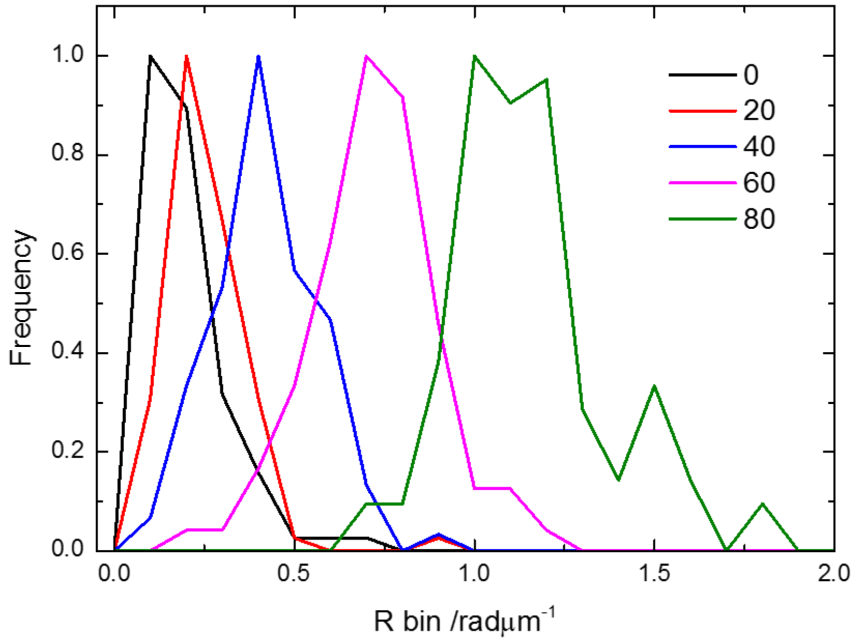

Figure 4.8 R value distribution of active colloids prepared from colloidal crystals for angles of θ=90° (black), 70° (Red), 50° (blue), 30° (pink) and 10° (green) .

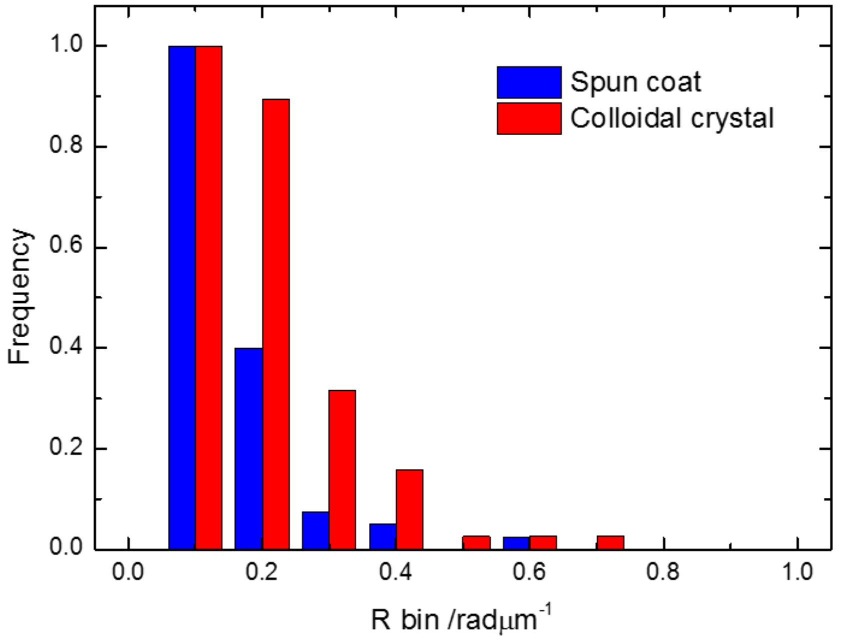

Figure 4.9 R value distribution of active colloids prepared from spin coating (blue) and colloidal crystals (red) at θ=90 °

As explanation to the observed effects, the asymmetrical distortion of the rotational symmetry of the platinum cap is clearly key. Two different models have been used to explain the phoretic phenomena in Janus catalytic active colloids as discussed in chapter 1.4. The chemical gradient induced diffusion phoresis[19],[6] and the self-generated electrical field electrophoresis[20], are discussed here in context of the results presented from this chapter.

4.3.2 Diffusiophoresis

The diffusiophoretic model states that in a standard case of a full hemispherical active cap, motion is generated due to an osmotic pressure resulting from a self-generated concentration gradient with the force being proportional to the concentration of a generated product at the surface of the catalyst (C) in comparison to the concentration of the product in the bulk solution C_∞.

The rate of generation of the catalytic products at the surface of the catalytic hemisphere is not equal. This is due to the gradient of thickness in the deposited platinum, modelled geometrically in Figure 4.10(a), and the knowledge that in the regime 0-10 nm, rate of reaction increases monotonically with platinum thickness[20]. However, as shown in Figure 4.10(a) the cap thickness variation are rotationally symmetrical resulting in a likely symmetrical fluid flow across the cap.

When $\theta < 90°$ however the rotational cap symmetry is broken, which in turn breaks the balance of flow across the active cap resulting a net flow away from the shadowed region Figure 4.10(d). A gradient of concentration results across the active cap creating a secondary contributing flow across the particle creating the additional angular velocity.

The rate of the secondary flow would be dependent on the ratio of generated products across the line of symmetry broken on the active cap.

4.3.3 Electrophoresis

Ebbens et al proposed that the mechanism of motion of active colloids is electrophoretic in nature, caused by a gradient of thickness in the deposited platinum from the pole to the equator of the hemisphere cap[20]. A result of this is a difference in reaction rate across the active cap (based on the thickness of the cap) and therefore based on the mechanism of catalytic decomposition of hydrogen peroxide which involves an electron transfer to coordinated peroxide species, would produce a gradient of electrons in the cap due to spatially defined reaction rate. An electron gradient then causes electron flow from the lowest towards the highest sites of activity and therefore an electric field results which pushes charged species around its surface generating phoretic motion.

For a full hemisphere the electron flow is predicted to be from the equator (thinnest and lowest reaction rate) towards the pole (thickest and therefore fastest reaction rate) creating symmetrical field lines resulting in an even flow of charged species across the active cap.

As the theta angle is decreased and shadowing effects are increased, the flow lines across the cap become increasingly imbalanced and the net flow line becomes increasingly directional across the active cap resulting in an additional angular velocity as can be seen in Figure 4.10(c) where the thickness plot is symmetrical about the peak $\Phi = 0$, (d) shows the progression as one side of the cap is shadowed and hence the electron flow from thinnest to thickest becomes increasingly one sided and therefore gives an increasingly directional flow across the cap giving rise to a self-generated rotating electric field.

The increasing net directionality may also explain the counter intuitive velocity increase of the particles despite a reduction in the platinum patch size as the generated electric field becomes increasingly coherent up to $\theta = 30^{o}$, after which it could be speculated that the coherence gain becomes smaller than the detrimental loss of platinum and resulting drop in reaction rate.

Figure 4.10e shows schematically why the crystal orientation impacts on the cap shape due to the position of the shadowing colloids relative to the source of deposition. The unwrapped cap thickness data for Figure 4.10e shows graphically that the crystal orientation (α) changes the shadow pattern but does not dramatically change the rotational symmetry, nor does it significantly change the total area of platinum as seen in Figure 4.11, suggesting the crystal orientation has low impact on the resulting rotational frequency, in line with the mono-modal population spread shown in Figure 4.5. There is scope for future work to test this, through the growth of large monocrystaline colloidal crystals as opposed to the polycrystalline regions obtained in this work. Such work may further still refine the level of control over the angular velocity by narrowing the distribution of rotational frequencies.

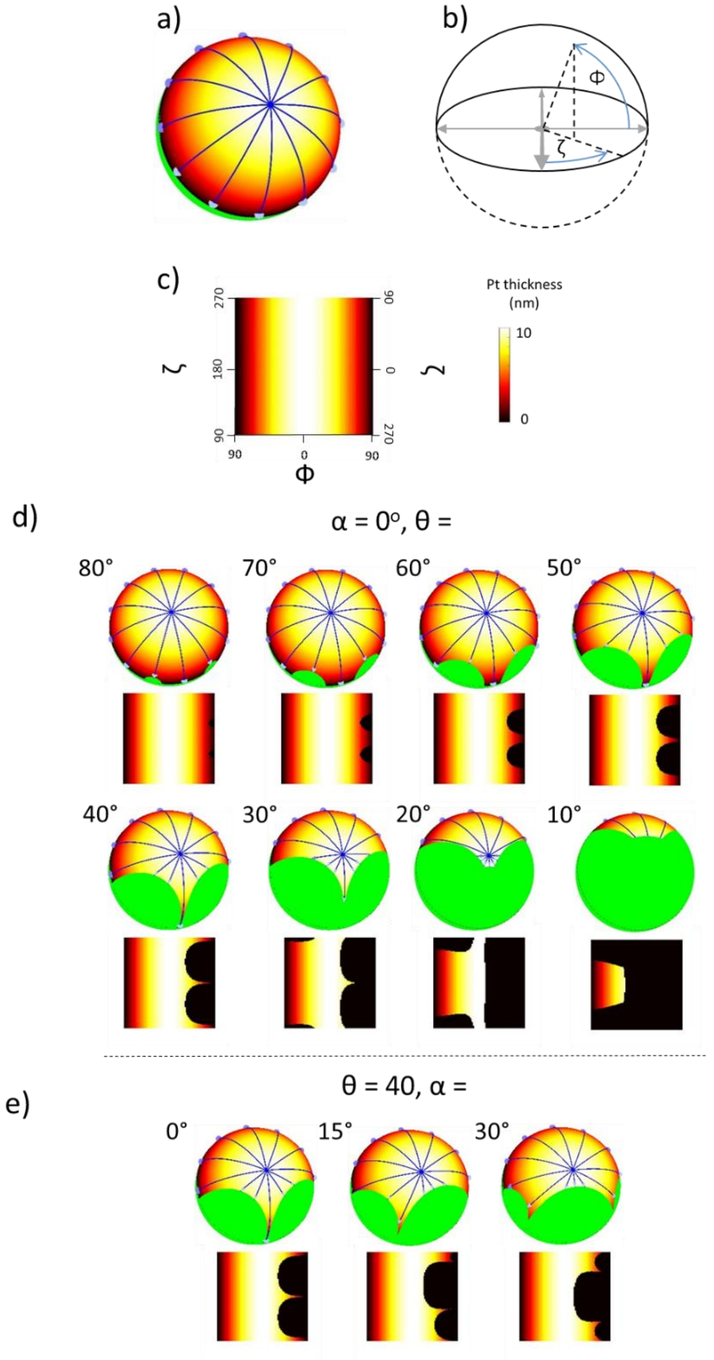

Figure 4.10 (a) 3D model of a Janus swimmer without shadowing. (b) Schematic representation of the altitude Φ and azimuthal ζ angles (c) Schematic representation of the altitude Φ and azimuthal ζ angles. (d) 3d and 2d representation of the cap (same format as a,c) for θ = 80 to 10° at α =0. (e) 3d and 2d representation of the cap (same format as a,c) for α= 0, 15 and 30° at θ =40. Figure provided by Dr. Andrew Campbell using mathematical algorithm given by Pawar and Kretzschmar [16].

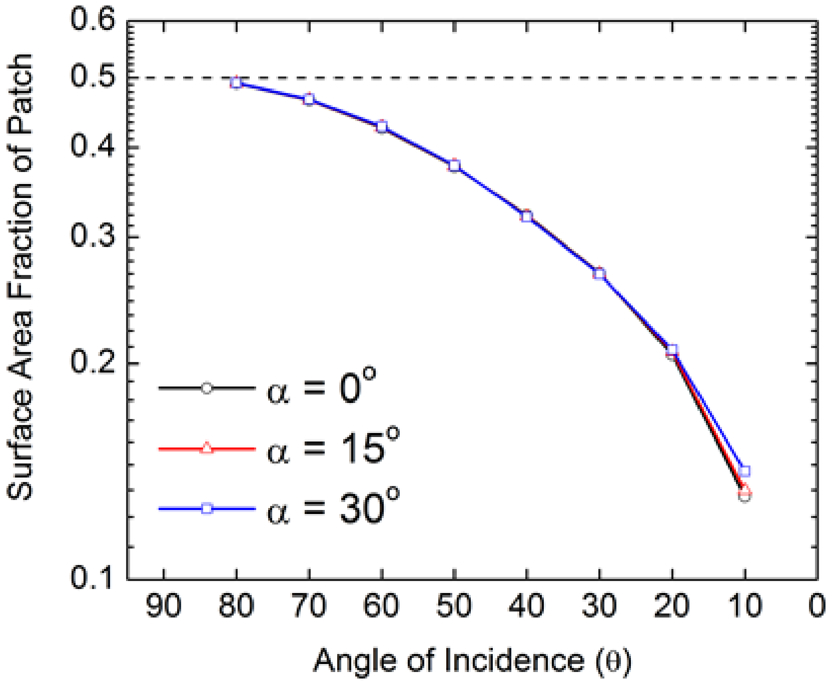

Figure 4.11 Graphical representation of overall patch area coverage with ϑ for apha (0, 15 and 30). Figure provided by Dr. Andrew Campbell using mathematical algorithm given by Pawar and Kretzschmar [16].

4.4 Conclusion

The results presented in this chapter show the rotational frequency of 2 µm diameter microswimming devices can be controlled from 0.25 to 2.62 Hz by changing the orientation of planar colloidal crystals with respect to a directional platinum vapour source (e-beam). Through SEM and geometric analysis it appears likely that this angular velocity is generated due to asymmetry in the active catalytic hemisphere of the Janus colloids, generated through shadowing of colloids by their neighbours due to the tilt angle.

This study adds weight to claims made by Howse et al that an increase in rotational diffusion in active colloids with full hemispherical coating is due to imperfections in the Pt cap during manufacture.

While the objective of this work was to induce angular velocity in a controlled manor, conversely this informs experimental procedures wanting to avoid an increase in rotational diffusion and maximising displacement. Ideal circumstances to achieve this goal being no tilt angle with respect to the platinum vapour and low colloid density.

This work can be considered as a step towards analogous motion of running (swimming) and tumbling (spinning) found in bacteria[21] however our artificial systems cannot currently switch between these types of motion. For bacteria this is an important mechanism for survival, for synthetic devices it is proposed that this could be a basis for study on a wide range of rotational phenomena.

Future work will build on the idea of an asymmetric imbalance across the active hemisphere causing spin. Specifically, if the imbalance can be switched off or on in response to a trigger by using a second catalytic site which reacts only with a second ‘fuel’ source. Such a system would represent a truly biomimetic, chemotactic runner and tumbler.

4.4 References

[1] J. Burdick, R. Laocharoensuk, P. M. Wheat, J. D. Posner, and J. Wang, “Synthetic nanomotors in microchannel networks: Directional microchip motion and controlled manipulation of cargo,” *J. Am. Chem. Soc.*, vol. 130, no. 26, pp. 8164–8165, 2008.

[2] S. Sundararajan, P. E. Lammert, A. W. Zudans, V. H. Crespi, and A. Sen, “Catalytic motors for transport of colloidal cargo,” *Nano Lett.*, vol. 8, no. 5, pp. 1271–1276, 2008.

[3] S. Balasubramanian, D. Kagan, C.-M. J. Hu, S. Campuzano, M. J. Lobo-Castañon, N. Lim, D. Y. Kang, M. Zimmerman, L. Zhang, and J. Wang, “Micromachine-enabled capture and isolation of cancer cells in complex media.,” *Angew. Chem. Int. Ed. Engl.*, vol. 50, no. 18, pp. 4161–4, Apr. 2011.

[4] D. Patra, S. Sengupta, W. Duan, H. Zhang, R. Pavlick, and A. Sen, “Intelligent, self-powered, drug delivery systems.,” *Nanoscale*, vol. 5, no. 4, pp. 1273–83, Feb. 2013.

[5] S. J. Ebbens and J. R. Howse, “Direct Observation of the Direction of Motion for Spherical Catalytic Swimmers,” *Langmuir*, vol. 27, no. 20, pp. 12293–12296, 2011.

[6] J. Howse, R. Jones, A. Ryan, T. Gough, R. Vafabakhsh, and R. Golestanian, “Self-Motile Colloidal Particles: From Directed Propulsion to Random Walk,” *Phys. Rev. Lett.*, vol. 99, no. 4, p. 048102, Jul. 2007.

[7] K. Kim, X. Xu, J. Guo, and D. L. Fan, “Ultrahigh-speed rotating nanoelectromechanical system devices assembled from nanoscale building blocks.,” *Nat. Commun.*, vol. 5, p. 3632, 2014.

[8] F. Kümmel, B. Ten Hagen, R. Wittkowski, I. Buttinoni, R. Eichhorn, G. Volpe, H. Löwen, and C. Bechinger, “Circular motion of asymmetric self-propelling particles,” *Phys. Rev. Lett.*, vol. 110, no. 19, pp. 1–5, 2013.

[9] T. Wu, T. a. Nieminen, S. Mohanty, J. Miotke, R. L. Meyer, H. Rubinsztein-Dunlop, and M. W. Berns, “A photon-driven micromotor can direct nerve fibre growth,” *Nat. Photonics*, vol. 6, no. 1, pp. 62–67, Dec. 2011.

[10] M. Domenech, I. Marrero-Berrios, M. Torres-Lugo, and C. Rinaldi, “Lysosomal membrane permeabilization by targeted magnetic nanoparticles in alternating magnetic fields.,” *ACS Nano*, vol. 7, no. 6, pp. 5091–101, Jun. 2013.

[11] A. van Reenen, A. M. de Jong, and M. W. J. Prins, “Accelerated particle-based target capture--the roles of volume transport and near-surface alignment.,” *J. Phys. Chem. B*, vol. 117, no. 5, pp. 1210–8, Mar. 2013.

[12] A. Nourhani, P. E. Lammert, A. Borhan, and V. H. Crespi, “Chiral diffusion of rotary nanomotors,” *Phys. Rev. E*, vol. 87, no. 5, p. 050301, May 2013.

[13] S. van Teeffelen, U. Zimmermann, and H. Löwen, “Clockwise-directional circle swimmer moves counter-clockwise in Petri dish- and ring-like confinements,” *Soft Matter*, vol. 5, no. 22, p. 4510, 2009.

[14] S. J. Ebbens, G. A. Buxton, A. Alexeev, A. Sadeghi, and J. R. Howse, “Synthetic running and tumbling: an autonomous navigation strategy for catalytic nanoswimmers,” *Soft Matter*, vol. 8, no. 11, p. 3077, 2012.

[15] S. Fournier-Bidoz, A. C. Arsenault, I. Manners, and G. a Ozin, “Synthetic self-propelled nanorotors.,” *Chem. Commun. (Camb).*, no. 4, pp. 441–3, Jan. 2005.

[16] A. B. Pawar and I. Kretzschmar, “Patchy particles by glancing angle deposition.,” *Langmuir*, vol. 24, no. 2, pp. 355–8, Jan. 2008.

[17] S. M. Weekes, F. Y. Ogrin, W. a Murray, and P. S. Keatley, “Macroscopic arrays of magnetic nanostructures from self-assembled nanosphere templates.,” *Langmuir*, vol. 23, no. 3, pp. 1057–60, Jan. 2007.

[18] S. Ebbens, R. a. L. Jones, A. J. Ryan, R. Golestanian, and J. R. Howse, “Self-assembled autonomous runners and tumblers,” *Phys. Rev. E*, vol. 82, no. 1, p. 015304, Jul. 2010.

[19] R. Kapral, “Perspective: Nanomotors without moving parts that propel themselves in solution,” *J. Chem. Phys.*, vol. 138, no. 2, 2013.

[20] S. Ebbens, D. A. Gregory, G. Dunderdale, J. R. Howse, Y. Ibrahim, T. B. Liverpool, and R. Golestanian, “Electrokinetic Effects in Catalytic Pt-Insulator Janus Swimmers,” pp. 1–5, 2013.

[21] G. H. Wadhams and J. P. Armitage, “Making sense of it all: bacterial chemotaxis.,” *Nat. Rev. Mol. Cell Biol.*, vol. 5, no. 12, pp. 1024–37, Dec. 2004.

Chapter 5:

Solution based synthesis of active Janus colloids

5.1 Introduction

As discussed in chapter 1, active Janus colloids have generated interest due to potential applications ranging from microfluidic transport in lab on a chip devices[1][2][3], rapid environmental decontamination[4], and directed drug delivery[5]. As evidence of the growing scope for real world applications for these devices, a recent report showed improved delivery of a model drug *in vivo***.**[6] In addition, self-motile swimming devices also provide a route to experimentally verify a wide range of phenomena that have been predicted for colloidal systems. One area of interest is the potential for high volume fractions of interacting motile colloids to display a rich variety of emergent behaviour including self-organising effects such as clustering[7]. However, despite this interest, the current methods by which synthetic catalytic swimming devices are manufactured remain cumbersome and have significant drawbacks, such as the requirement for specialised equipment. This limits catalytic Janus colloid availability and viability of proposed applications, as well as hampering extensive experimental research effort into active colloid phenomena, particularly at higher volume fractions.

The prominent examples of self-phoretic active colloids discussed in chapter 1, which rely on chemical reactions to produce motion requires a specific distribution of catalyst, are critically reliant on producing chemical gradients which can only be generated by asymmetrical catalyst distributions. Taken together, the requirement for both metallisation and asymmetry generation has resulted in the current manufacturing methods being typically low yielding, owing to a reliance on physical vapour deposition (PVD) techniques to deposit the catalyst which as discussed in chapter 2, is a high energy process which takes place in a confined space. For the aforementioned examples in chapter 1, bimetallic rods synthesis requires a combination of PVD and electroplating into porous membranes for each required metal, microrockets require PVD of multiple metals onto sacrificial polymer films which when etched away cause the metal films to roll into the required tubular structure, while active Janus colloids require platinum PVD onto spherical colloids[8][9][10]. The PVD requirement restricts all these processes to 2D planar batch fabrication and the requirement in PVD for high vacuum environments creates scalability issues and high energy demands to vaporise the source material.

The focus of this chapter is to develop an alternative manufacturing route that can produce high yields of swimming devices, to both provide a viable route to scale-up to meet the requirements of emerging applications, and to allow straightforward synthesis of lab-scale batches of active colloids to aid investigation of active colloid phenomena. Additionally such a synthetic route would contribute to the discussion on the phoretic mechanism as the current reported theory for single metal active colloids requires a gradient in the metal thickness, the formation of which is not expected for the chemical functionalisation methods described here[11].

The new methods developed in this chapter focus specifically on making spherical Janus colloids. Spherical Janus colloids have been reported to display a wide range of interesting colloidal phenomena, including autonomous guidance effects (gravitaxis[12], chemotaxis[13] and boundary steering[14]), and has also been the subject of many currently untested theoretical proposals for high volume fraction collective phenomena. An advantage of Janus spheres as a system to explore emergent behaviour, is that they move without producing bubbles and so their interactions via chemical “wakes” and hydrodynamics are amenable to being analysed and experimentally observed, whereas nanotubes produce considerable convective flow due to bubble release[15]. In addition, in contrast to nanorods, Janus spheres can also be studied in 3D bulk solution as their body can be neutrally buoyant, whereas metallic nanorods undergo rapid sedimentation.

For current Janus sphere synthesis, PVD is used to both deposit the platinum catalyst and generate the required asymmetry. Asymmetry is introduced due to the directionality of the metal deposition process (chapter 2), resulting in the underside of the colloid not receiving any platinum. Against this background, the aim of this chapter is to instead chemically deposit platinum on colloids asymmetrically in solution to give a low energy, highly scalable alternative route to micron scale self-motile active colloids.

The strategy used here is to partially mask colloids during the solution deposition of platinum. This is achieved by a Pickering emulsion technique described by Hong *et al*. and Perro *et al*. where the colloidal bodies are trapped between an oil and water interface which on cooling solidifies the oil phase to create an impermeable barrier encompassing the oil submerged portion of the body. The protruding portion can then be chemically modified[16][17]. This technique is deployed here to grow platinum films on the protruding portion to create the catalytically active Janus structure. Further to this, reports of the ability to control the percentage portion masked by changing the hydrophobicity of the colloidal spheres would offer unprecedented control over the percentage of the surface platinated[18].

This study uses silica as the body material for the active colloids due to the ease in producing large scales of monodisperse colloids with controllable diameters as previously mentioned in chapter 2.2 and demonstrated in chapter 3[19][20]. Silica offers other potential advantages in controllable porosity. Mesoporous silica is well documented and easily produced with tuneable pore sizes through small modifications to the Stober-Like processes used to make silica hard spheres[21]. Mesoporous silica has been extensively studied for its potential use in drug storage and delivery which is also a potential application for active Janus particles[22]. Also the ready ability to functionalise silica surfaces via Silanes[23] assists the chemical deposition of platinum, but also aids additional selective chemical modifications of the inactive side of the colloid.

While platinum films have been reportedly grown using electroless chemical deposition, such systems often rely on harsh chemicals such as hydrazine or elevated temperatures unsuitable for use with silica and wax masking[24]. Inspired by the ability to chemically grow gold shells on colloids, here a seed and growth method is employed using a platinum salt pre-cursor[25]. This method relies on the electrostatic adhesion of negatively charged metallic nanoparticles formed from rapid reduction of platinic acid using sodium borohydride to a positively charged aminopropyl silane (APS) modified surface chemistry of the colloid[26]. From these initial surface bound particles the potential to control further addition to the surface through the slow reduction of platinic acid to its base metal using the mild reducing agent formaldehyde is investigated. This step aims to allow Pt(0) to join the existing seeds, eventually forming thicker more continuous shells[27]. The potential to control platinum thickness without creating a thickness gradient which occurs with PVD, is of interest as it would contribute to the discussion of the propulsion mechanism mentioned in chapter 1.4.3[11]. A further advantage of this approach, is that after platinum deposition and release from the Pickering mask, the catalytically inactive side of the silica colloid displays amine surface functionality, widely used for biological binding of proteins and antibodies which could potentially allow biological recognition and specific targeting applications.[28][29].

To test the effectiveness of the chemically prepared active colloids, propulsion velocity, rotational behaviour and salt tolerance are benchmarked against equivalent conventionally PVD manufactured Janus particles[30]. In addition, batches of chemically prepared colloids with varying concentrations of platinum salt added during the seed growth stage of the protocol are compered. In order to understand the effect of the growth conditions on active colloids performance, the physical structure of the platinum coating is characterised using Scanning Electron Microscopy (SEM) and Atomic Force Microscopy (AFM).

5.2 Experimental

5.2.1 Materials

Tetraethyl orthosilane (TEOS, 98%), Ammonia (25% wt), Paraffin wax, Sodium Borohydride (99%), Sodium dodecylsulfate (SDS, 98%), cetyltrimethylammonium bromide (CTAB, 98%), Hexachloroplatinic acid hexahydrate (>37.5 % Pt basis), hydrogen peroxide (30% wt), and methanol (99.6%) were purchase from Sigma Aldrich. Aminopropyl silane (APS, 97%), and Formaldehyde (37% wt) were purchased from Alfa Aesar. All materials were used as received. Deionised (DI) water was obtained from an Elga Purelab Option filtration system (15 MΩ cm).

5.2.2 Silica colloids

Mono-disperse silica colloids were prepared by a Stober-like method, based on the procedures by Nozawa *et al.* and Wang *et al*. as discussed in chapter 3[20][31].

Briefly, a TEOS solution (1:1 in 2-propanol, v/v %) was drip fed via syringe pump (Aladdin NE-1000) into a magnetically stirred solution containing 2-propanol, water and ammonia, at a controlled rate of 2.5 ml hr^{-1} at 4 ^{o}C to a final concentration of 1.24 M, 7.16 M, 0.141 M, TEOS, H_2O and NH_3OH respectively.

The formed colloids were washed in ethanol by centrifugation and removal of the supernatant to remove excess TEOS, washed in water by centrifugation to remove ammonia (confirmed by pH) and finally washed and re-suspended in a small amount of ethanol to remove the water and dried at 80 ^{o}C

5.2.3 Silanization

Surface functionality is given through self-assembled monolayer silanization techniques which do not significantly alter the size or size dispersity of the colloids. Prepared silica colloids were dispersed in toluene (2.3 wt %) by ultra-sonication with excess aminopropyl silane (APS, 3.4 mmols m^{-2} of silica) and refluxed for 24 hours. Figure 5.1a.

APS treated colloids are then washed in ethanol by centrifugation and finally dried 80 °C.

5.2.4 Pickering emulsion

Pickering emulsions were prepared as described by Perro *et al*. where bare silica colloids in conjunction with certimonium bromide (CTAB) cationic surfactant are used to stabilise an emulsion of wax (mpt. 60-70 °C) in its molten liquid state, through adsorption at the oil/water interface. Upon cooling the wax solidifies and traps the silica between the oil and water interface Figure 5.1b.

Due to the use of APS modified silica, sodiumdodecyl sulfate (SDS) was used as an anionic surfactant to complement the colloid surface charge and hydrophobize the silica sufficiently to facilitate emulsion stabilisation[17]. The concentration of SDS was varied to attempt to control the Janus balance. Additionally the ratio of silica to wax is also varied to optimise the emulsion system.

The SDS solution, wax and Stober-like synthesised silica is sonicated together for 15 minutes before heating to 75 °C and rapid stirring for 2 hours, after which the stirring was stopped and the emulsion was taken off heat and allowed to cool to room temperature solidifying the wax after which the solid phase was filtered and washed in cold methanol to remove surfactant without affecting the wax.

5.2.5 Seeding

Platinum seeds were prepared by the rapid reduction of hexachloroplatinic acid (31.25 µM) in methanol by the addition of sodium borohydride (0.066 M).

A prepared seed solution of 40 ml was then rapidly added to 0.1 g of washed Pickering emulsion powder and the solution was gently agitated over 30 minutes. The powder would change from a pristine white to pale grey indicating the attachment of the seeds. The seeded solid was then filtered and washed with cold methanol. Figure 5.1c

5.2.6 Metal growth

The Pt seeded embedded silica powder (0.1 g) was placed in a 1 % formaldehyde solution containing water and ethanol (1:1) and hexachloroplatinic acid (at 0, 2.11, 4.23, 8.46 and 16.92 x10^{-9} mols of platinum per cm^2 of silica based on the starting mass of silica colloids used) and gently agitated over 72 hours. Figure 5.1d.

5.2.7 Particle release

The platinated particles were dispersed in dichloromethane and centrifuged at 3000rpm (1811 RCF) to liberate the colloids from the wax mask, this was repeated three times to ensure complete removal of the wax. Figure 5.1e.

Colloids were then washed in ethanol by centrifugation to remove DCM, this was repeated 3 times and then further washed in water by centrifugation to remove salts, repeated 3 times. The final product was kept suspended in water until use.

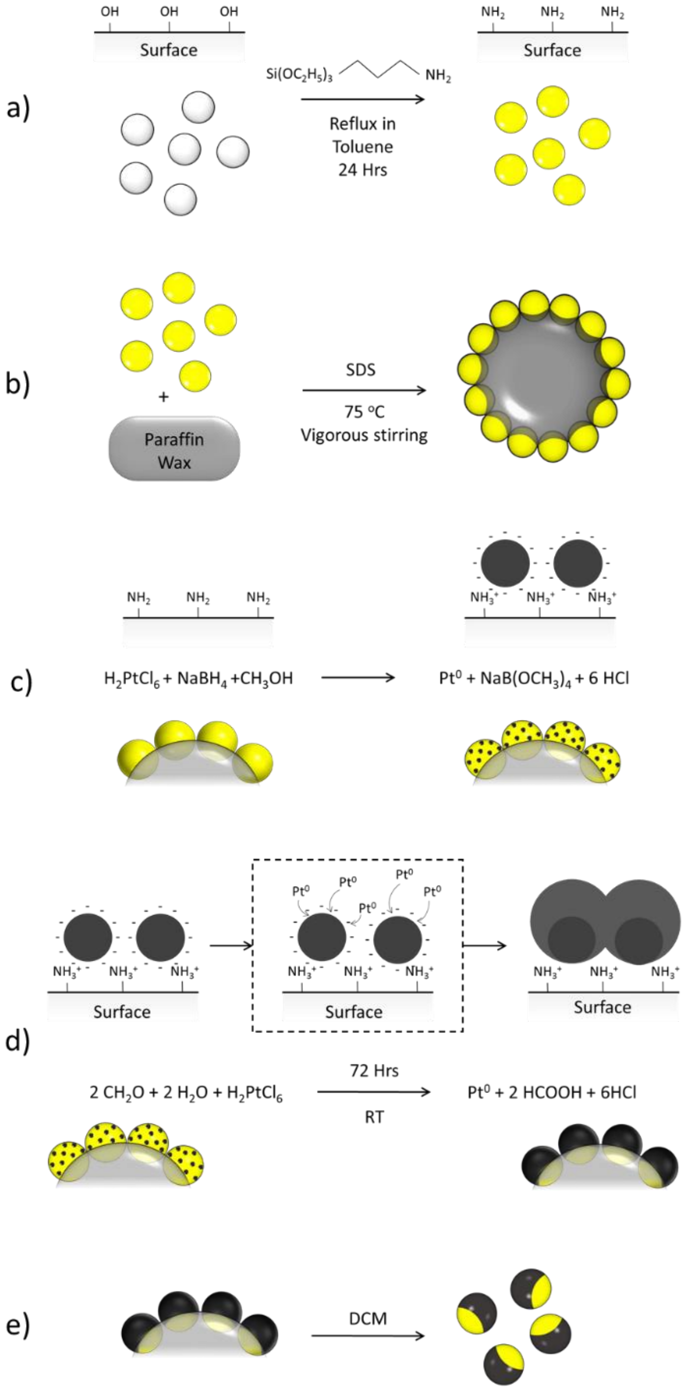

Figure 5.1 Schematic showing steps to create active Janus colloids through solution synthesis. a) silica are refluxed in toluene with APS to aminate the surface b) The aminated silica colloids are hydrophobized with SDS and emulsified with the melted wax to form the Pickering emulsion c) The trapped aminated silica is seeded with platinum nanoparticles d) The seeded particles are grown using platinic acid and formaldehyde over 3 days. e) The colloids with grown platinum are released using DCM to dissolve the wax.

5.2.8 Pt thickness estimation

The thickness of the solution grown platinum shell is estimated on the basis of the 2/3rds coverage which allows an easy conversion by simply reducing the available surface area by 1/3rd. The final thickness is then calculated by converting the number of moles per cm^2 to mass per cm^2 and using the known density of platinum (21.45 g cm^{-3}) to calculate the depth (i.e thickness) of the volume for the given area of known mass.

5.2.9 Yield efficiency

Yields were obtained by microscopy observation of the number of colloids in a known volume. The stock solution of active Janus colloids was diluted to 0.25% of the original concentration and the diluted solution was placed into a cuvette. Due to the focal point only allowing a thin section of the solution to be analysed at any one time, the colloids in the cuvette were allowed to sediment from the bulk to the bottom surface for 24hrs to bring the colloids to the same focal point. After the complete sedimentation, images of several sections of the bottom interface were taken and the number of colloids recorded. The volume was calculated using the known 2D image area and the depth of the cuvette used to convert to volume. Figure 5.2.

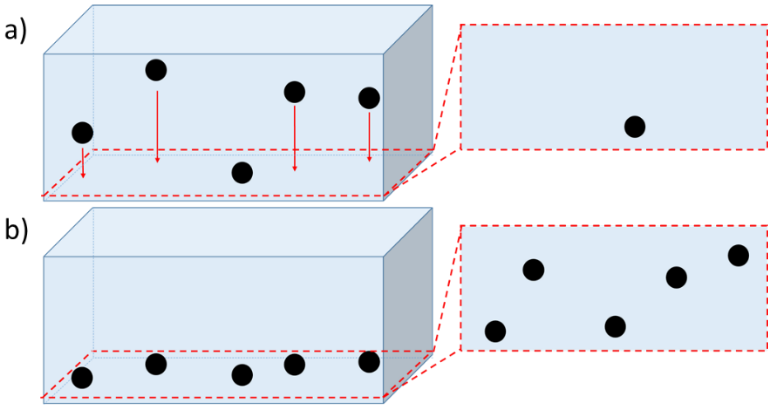

Figure 5.2 Representation for a dispersion of colloids in a volume of solution and the observable section highlighted by red dashed line, for (a) well dispersed colloids (b) sedimented colloids.

5.2.10 Physical vapour deposition (PVD)

Platinum thin films were deposited by e-beam evaporation of platinum metal (99.995%) using a Moorfield Minilab 80 evaporator under high vacuum ($1x10^{-9}$ bar), on to glass slides containing low density arrangements of the silica colloids, prepared by spin coating (2000 RPM) low concentration of colloids dispersed in ethanol. Platinum thickness was measured using a quartz crystal monitor.

5.2.11 2D tracking

Platinum coated colloids were transferred to a hydrogen peroxide solution (15 wt%), sonicated for 5 minutes and left standing for a further 25 minutes to remove trace surface contaminants, after which the solution is further diluted to 10% H_2O_2 by weight in which the measurements will take place.

Nikon eclipse inverted microscope coupled to a Pixelink PL-B742F camera was used to capture a kinetic image series of 800x600 pixels at 33 frames per second for 30 seconds. Multiple tracks were recorded for each set of samples (≥ 25 videos). A custom LabVIEW program was used to analyse the trajectories and generate the Mean Squared Displacement and velocity.

5.2.12 Reaction rate analysis

Reaction rates were obtained from known concentration of active Janus colloids in 10% H_2O_2 under magnetic stirring.

UV/Vis absorption measurements were taken at 240 nm wavelength every 30 minutes for a total of 180 minutes. The reaction rate could then be determined from the gradient using the molar extension coefficient as stated by the manufacturer Sigma Aldrich (43.6 m^2 mol^{-1}).

5.3 Results and Discussion

5.3.1 Chemical Synthesis of Active Janus Colloids

Silica colloids grown by a Stober-like process (1.1 µm diameter, confirmed by Nanoparticle Tracking Analysis (NTA)) were surface modified with APS using the well-known anhydrous reflux technique to introduce amine functionality across the entire particle surface. SEM and NTA were used to evaluate the size and surface morphology of the resulting APS modified silica colloids as presented in Figure 4.*3*. It is shown that monodisperse silica colloids with smooth surfaces were produced.

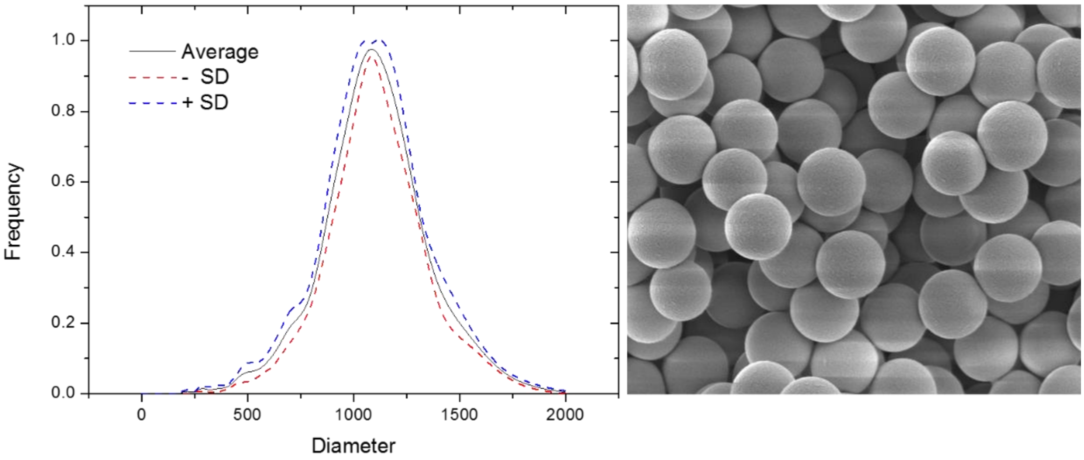

Figure 4.3 Left: Normalised frequency distribution for synthesised silica colloids. Right: SEM image of synthesised colloids.

Before solution deposition of platinum was attempted, these APS modified silica colloids were added to a molten wax in water Pickering emulsion. This stage is intended to partially mask the APS colloid surface.

APS modified silica colloids were found to be too hydrophilic to stabilise the wax without the addition of additional SDS surfactant. SDS was added to the APS-silica suspensions to final concentrations of 0.21 mM, 0.41 mM, 0.82 mM, 1.23 mM, 1.60 mM and 2.05 mM.

SDS concentrations at 0.21 mM and 2.05 mM did not result in an emulsion. SDS concentrations at 0.41 mM, 0.82 mM and 1.60 mM caused visible aggregation of the APS-silica colloids in water, indicating a change in hydrophobicity, at these concentrations the Pickering emulsions successfully formed. To assess the penetrative depth of the silica in the wax at the stated SDS concentrations, the separated and dried emulsified wax was gold-coated by argon sputtering and SEM images were taken at defect sites on the wax, were the colloidal monolayer was incomplete. These defect sites allow a view of the silica-wax interface and a qualitative assessment of the penetrative depth to be assessed. SEM results for the successfully formed emulsions are given in Figure 5.4. it can be seen that for Figure

5.4a and b. where SDS concentration is at 0.41 mM and 0.82 mM respectively, the penetrative depth is slightly less than one third of the diameter of the colloid. For Figure 5.4c and d. at SDS concentration of 1.23 mM and 1.60 mM respectively, the penetrative depth appears to be slightly greater at approximately one third of the diameter.

The difference in penetrative depth however appears to be very low and not significant enough to allow for significant a range of catalytically active coverages.

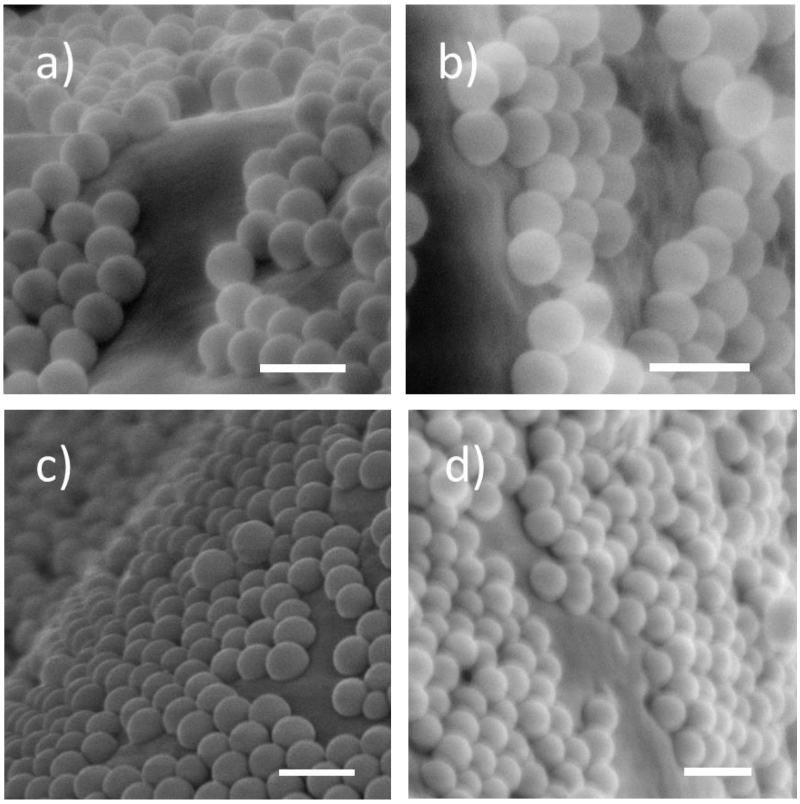

Figure 5.4 SEM of Pickering emulsion surface at SDS concentrations of 0.41 mM, 0.82 mM, 1.23 mM, 1.60 mM, a-d respectively. Scale bars represent 2µm.

The ratio of wax to silica was also investigated to assess the effects on the efficiency on the emulsion formation. Increasing the wax percentage increased the size of the emulsion as can be seen from Figure 5.5 a,c and e, but had no observable effect of the penetrative depth of the silica into the wax as shown in Figure 5.5 b, d and f. The quantity of wax used in this study produced no obvious changes in the process, other than the size and morphology of the emulsion but had no impact for the purpose of masking. The highest ratio of wax to silica (1: 0.0556) was selected as the standard going forward simply due to ease of handling.

Emulsions formed with approximately 84% yield with respect to mass of initial wax, the remaining 16% did not emulsify and instead coated the reaction vessel walls, this minor wax portion appeared to contain no embedded silica by SEM observations, nor was any significant quantity of silica colloids found outside of the emulsified wax after completion of the solidified emulsion. All non-embedded silica colloids would be lost during washing stage after the formation of the solidified wax, removing the potential for secondary non-Janus functionalised particles. The resulting solidified and washed Pickering emulsion was then observed by SEM. The wax contained a densely packed arrangement of silica colloids partially embedded into the wax surface with the exception of defect sites where silica is more sparsely populated. These defect sites are used for SEM imaging as the wax-silica interface is observable.

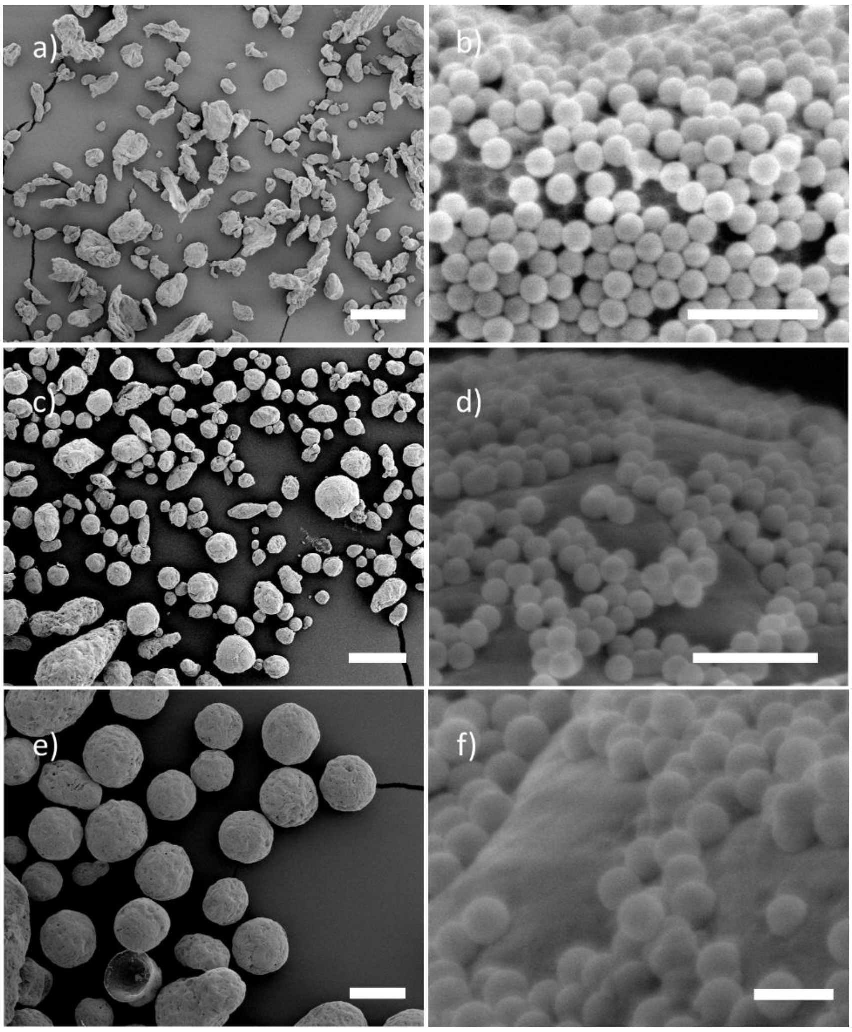

Figure 5.5 Wax to silica ratio of (a-b) 1 : 0.04 scale bars, 200 µm and 5 µm respectively (c-d) 1: 0.01 scale bars, 200 µm and 5 µm respectively (e-f) 1 : 0.005 scale bars, 200 µm and 2 µm respectively.

Having established that the masking stage required to introduce asymmetry had been successful, a variety of batches of colloids were chemically modified with platinum, using the two stage seeding and growth approach discussed above. The first rapid reduction stage to generate the platinum seeds was carried out with a constant amount of platinum salt added, while the second growth stage was performed with a varying amount of salt, Table 5.1.

EDS elemental mapping was used to verify the presence of platinum and its location relative to that of the silica colloids. Figure 5.6 gives location intensity profiles for silicon, oxygen and platinum. It can be easily seen that the silicon and oxygen as expected, overlays with the location of silica colloids as presented by the secondary electron scan in Figure 5.6a. Figure 5.6d shows a platinum composition map which although displays a lower signal to noise ratio (due to the low concentration of platinum in comparison to the abundant silica), still clearly gives peak intensities which overlay with the location of silica. This is taken as confirmation that platinum has been successfully attached to the surface of the APS-silica.

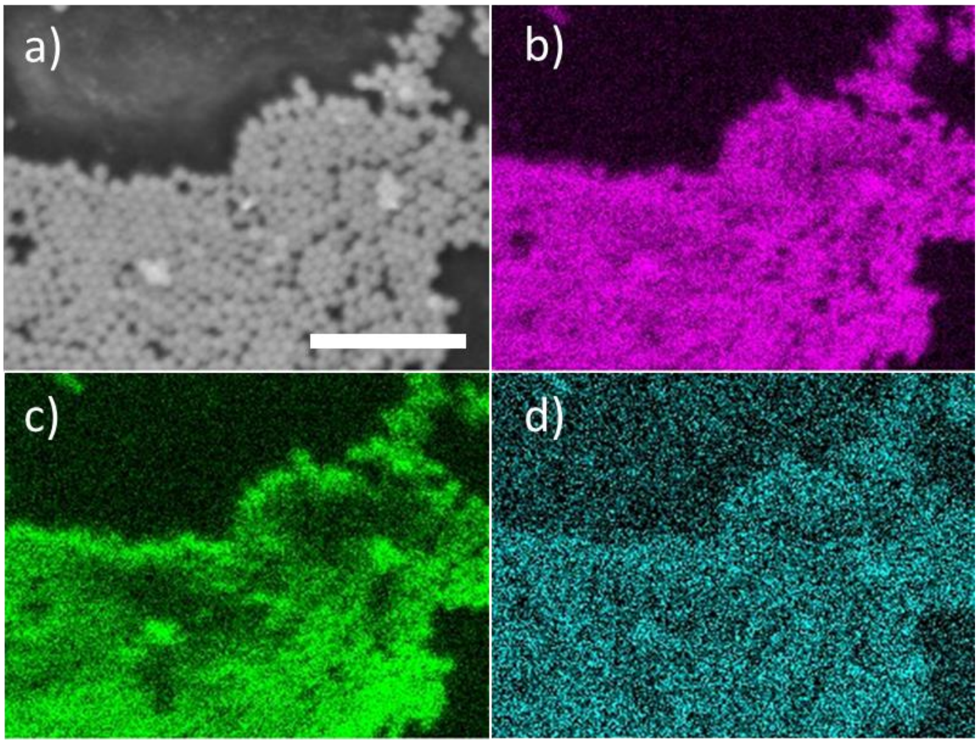

Figure 5.6 EDS mapping scan. (a) Secondary electron scan of area analysed (b) silicon (c) oxygen and (d) platinum.

After completion of platinum growth, the colloids were separated from the wax by using DCM to dissolve the away the protective wax. The particles were washed as outlined above in the methods section. The washed colloids then were dispersed onto an aluminium stub for SEM analysis.

Figure 5.7 a and b. show backscattered SEM images of a typical batch of randomly orientated colloids (10.69 nmols of platinum per cm^2 during growth stage). The surface distribution of platinum can clearly be seen as a bright contrast in comparison to the silica. This contrast is due to the relatively heavy Pt nuclei strongly backscattering incident electrons giving high signal intensity compared to the lowed mass silica body. The presence of a material with a heavy nuclei in comparison to silica, located on the colloid exposed to the platinic acid indicates that platinum has been successfully deposited. The platinum is revealed to cover approximately 2/3rds of the spherical colloids in a continuous shell. This is consistent with the SEM observation of the wax embedded colloids being submerged by approximately 1/3rd. There is also some apparent variance in coverage and cap shape given that the exposed section is not in all cases symmetrical. Each batch of colloids prepared with varying amounts of platinum salt added during the growth stage showed a qualitatively similar distribution of platinum after release from the Pickering emulsion. Table 5.1 also contains an estimate of the expected corresponding maximum deposited platinum thickness for each batch, based on the assumption of 2/3rds coverage. Back-scattered contrast in SEM images correlated with the expected deposited thickness, with brighter contrast for samples prepared with higher platinum salt concentrations.

For comparison, Figure 5.7 c-d, show backscattered SEM images for randomly orientated silica colloids coated with a platinum hemisphere using the conventional physical vapour deposition method. As expected, due to the line of sight shadowing effect that introduces the asymmetry in this preparation method, the cap is shown to be highly consistent with 50% platinum coverage, and the cap shape shows little variation. In addition, the platinum shells prepared by PVD appear qualitatively to be smoother than those prepared by chemical reduction of platinum pre-cursors as evident by comparing Figure 5.7 b and Figure 5.7 d.

The substrate supporting the colloids has a bright grainy appearance. It is noted that the grain pattern appears brighter in Figure 5.7 a-b than Figure 5.7 c-d, due to the higher contrast used in imaging a-d. This also fits with the calculated thickness difference of the solution prepared Janus colloids to the relatively heavy coating of the PVD prepared Janus colloids.

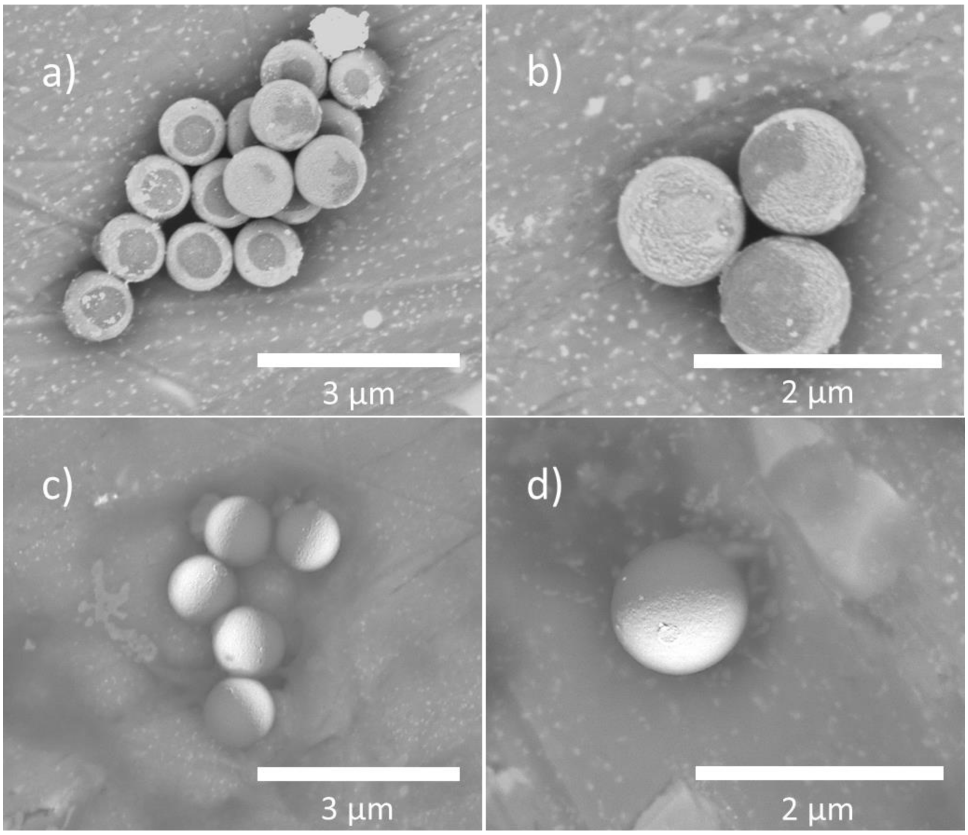

Figure 5.7 (a-b) Backscatter images of Pt coated silica after release from the wax. (c-d) backscatter images showing Pt coated silica prepared by PVD

Table 5.1. Platinum thickness and yield for Janus colloids grown from given concentrations of chloroplatinic acid

H_2PtCl_6 in Seed Sol	H_2PtCl_6 in Growth Sol	H_2PtCl_6 in Total	Estimated thickness	Yield
nmol cm^{-2}	nmol cm^{-2}	nmol cm^{-2}	nm	%
8.46	0.00	8.46	1.15	29.7
8.46	2.11	10.57	1.44	58.1
8.46	4.23	12.69	1.73	56.5
8.46	8.46	16.92	2.31	53.4
8.46	10.69	19.15	3.46	41.9

5.3.2 Catalytic swimming behaviour

Both PVD prepared colloids, and the chemical grown catalytically active Janus colloids were dispersed into a 10 % wt/vol hydrogen peroxide solution and their motion was observed and recorded via optical microscopy as described previously in chapter 2.3. Figure 5.8 a and b respectively show examples of trajectories for propulsive Janus colloids prepared by PVD (10 nm coating thickness) and solution based synthesis (3.5 nm thickness). The nature of the trajectories are consistent with previous reports whereby active colloids displaying short term ballistic type trajectories which are randomised due to rotational diffusion of the colloid as a result of the directionality of the propulsion vector being fixed in relation to the catalyst distribution[32]. While the platinum distribution is different between the two synthesis methods the resulting enhanced motion is strikingly similar, this indicates the clear potential to use the solution based fabrication method to make active colloids.

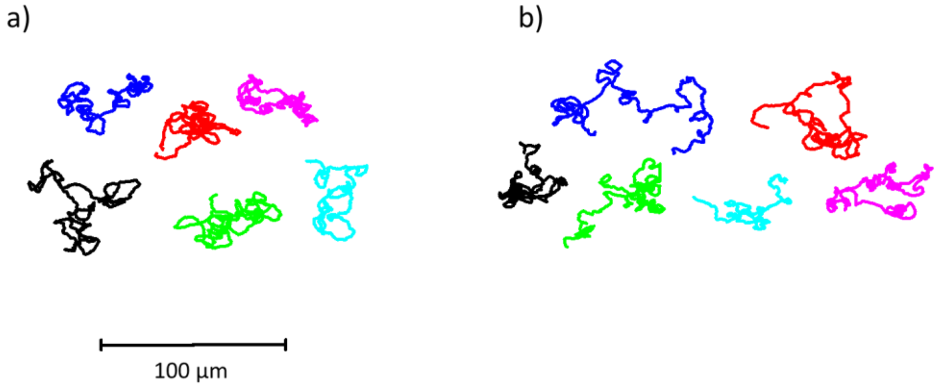

Figure 5.8 . Representative x,y plots of particles displaying enhanced motion, extracted from 30 second videos at 33 fps for active colloids prepared from a) PVD to 10 nm thickness and b) Solution based growth of Pt from H_2PtCl_6 to a thickness of 3.46 nm.

To assess the effect of changing platinum salt concentration during the solution platinum growth stage on active colloid behaviour, trajectories were recorded for colloids prepared according to the conditions detailed in Table 1. Velocity (V) and rotational diffusion coeffiecient (τ_R) were calculated from the mean squared displacement (MSD) using equation 2.9 (fitted to the quadratic section from 0 to 0.25 seconds, well below the rotational diffusion time) and equation 2.13 (fitted to the linear section from 2 to 3 seconds, well above rotational diffusion time) respectively[10].

A similar analysis was applied to batches of colloids prepared using the PVD method with increasing platinum thickness. Figure 5.9 a and b shows the translational velocity comparison for PVD and solution prepared active colloids respectively. It is apparent that the solution prepared colloids show a plateau in translational velocity (10.40 ± 3.74 µm s^{-1}) at a thickness of just 2.31 nm, at a similar maximum thickness, the PVD prepared samples show a much slower velocity of approximately 3 µm s^{-1}, however these velocities increase monotonically up to 13.83 µm s^{-1} (± 2.43 µm s^{-1}) at 10 nm of platinum. Figure 5.9 c and d show the rotational diffusion time for the PVD and solution based preparations. In both cases τ_R is close to the theoretical value (1.01 seconds at 21 °C), marked as a dashed line on the graph, at low velocities but decreases with higher velocities, a trend reported previously for PVD Janus colloids[10]. However, no evidence for regular spiralling behaviour was seen in the trajectories or MSD plots, suggesting that the colloids were not producing a constant propulsive angular velocity vector, as is the case for PVD prepared Janus colloids with rotationally asymmetric catalytic activity[33]. Figure 5.9 e also gives translational velocity histogram data for the fastest PVD and solution based active colloids produced here. The solution based velocities show a slightly wider spread, which is not unexpected due to the variation in platinum distribution revealed by SEM.

In most models for phoretic self-propulsion, there is a link between translational propulsion velocity and reaction rate as described in chapter 1.5, and so it is likely that features of the platinum coating that increase reaction rate will also effect propulsion speed.

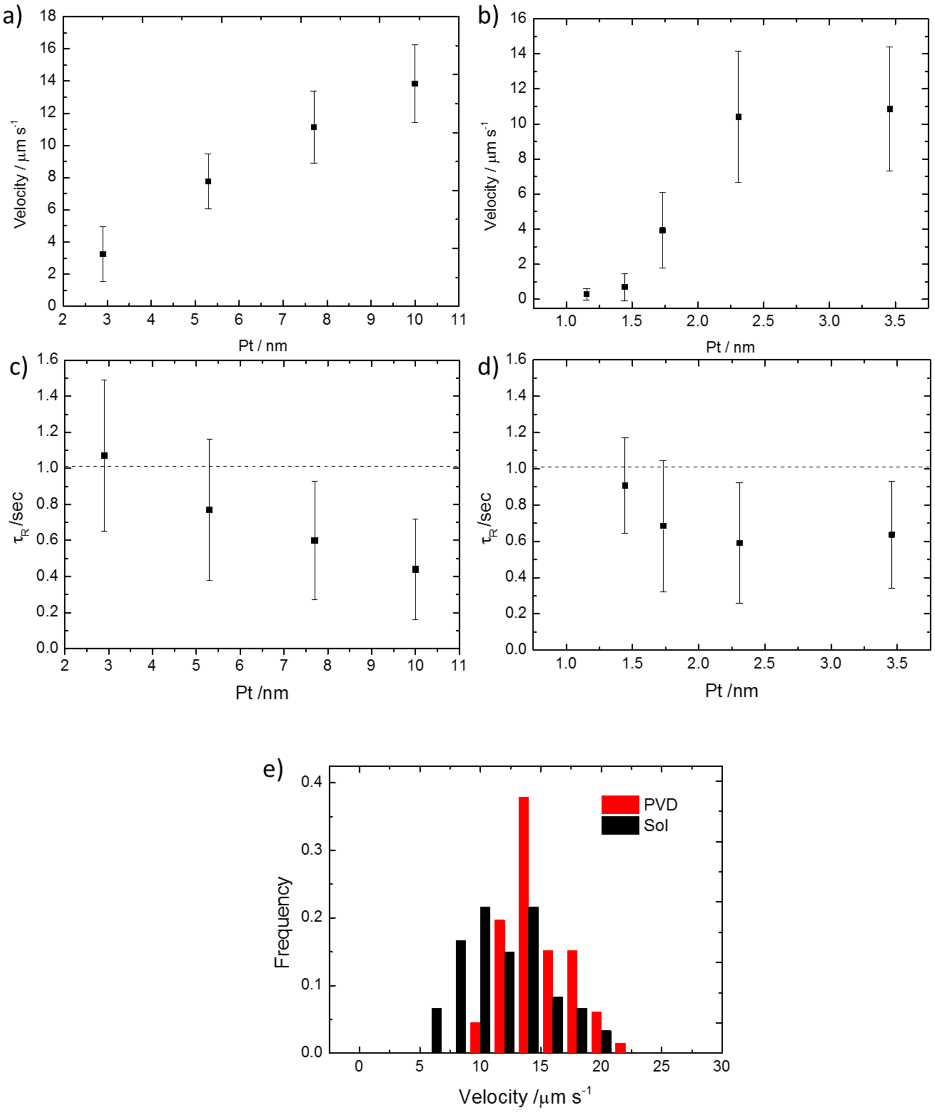

Figure 5.9 (a) Translational velocity of active colloids prepared by PVD to platinum thicknesses of 2.9, 5.3, 7.7 and 10 nm (b) Translational velocities of active colloids prepared by solution growth of platinum to thicknesses of 1.15 , 1.44, 1.73, 2.31 and 3.46 nm (c) Rotational diffusion of active colloids prepared by PVD to platinum thicknesses of 2.9, 5.3, 7.7 and 10 nm (d) Rotational diffusion of active colloids prepared by solution growth of platinum to thicknesses of 1.44, 1.73, 2.31 and 3.46 nm (e) Histogram of relative velocity frequency at platinum thickness of 10 nm and 3.46 nm for PVD (red) and solution grown (Black) platinum.

To further understand the origin in the differences in velocity versus platinum thickness curves for PVD and solution prepared active colloids, Atomic Force Microscopy (AFM) was used to examine the surface morphology of analogous surfaces. Flat silica substrates were subject to equivalent platinum coatings to those performed on the active colloids, Figure 5.10. Quantification of Root Mean Squared (RMS) surface roughness was also performed. Figure 5.10 a and b show that Silane modification of the surface with APS does not significantly change the surface topography or roughness, as is expected for monolayer assemblies. Figure 5.10 c shows that the initial seeding stage of platinum deposition does change the surface topography, due to the surface adhesion of platinum nanoparticles. As the platinum is grown onto the seeds, the roughness increases further as shown in Figure 5.10 d (final RMS roughness = 3.08 nm). In comparison, PVD deposition of a 10 nm thick platinum film results in a RMS roughness of 0.25 nm, similar to that of the APS modified glass slide before seeding Figure 5.10 e.

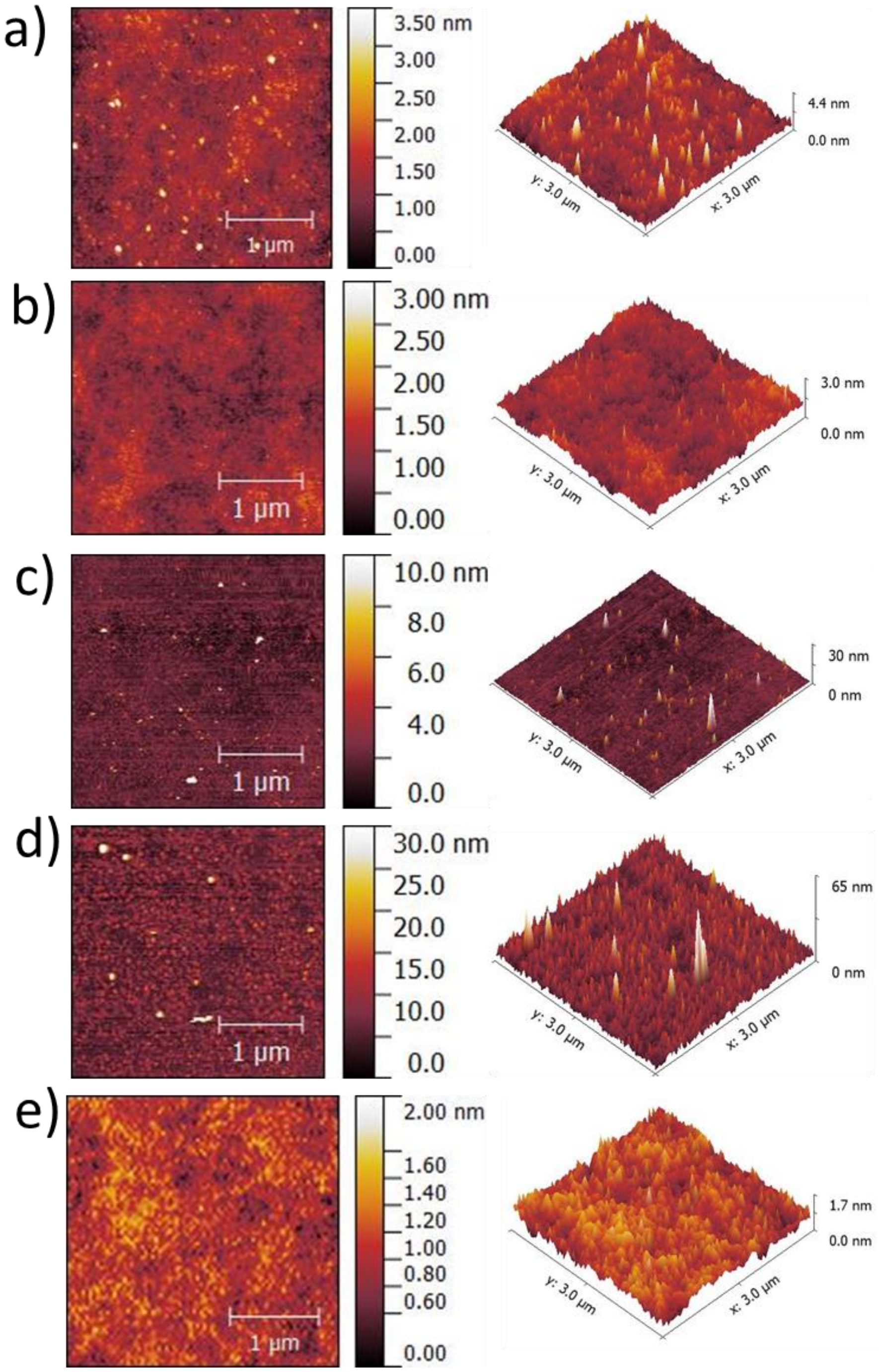

Figure 5.10 AFM measurement of (a) unmodified glass surface, RMS 0.34 (b) Glass surface modified with monolayer of APS, RMS 0.25 nm (c) APS modified glass washed with platinum seed solution, RMS 0.88 nm. (d) Pt seeded surface after 3 day exposure to growth solution, RMS 3.08 nm. (e) Glass surface after PVD of platinum (10nm), RMS 0.25 nm.

Through both SEM and AFM, it has been shown that the solution prepared colloids have a rough surface. Rough surfaces typically indicate an increase in surface area and therefore an increase in reactivity for catalytic surfaces.

Obtaining such large numbers of active Janus colloids has allowed sufficient concentrations to significantly change the H_2O_2 concentration in the volumes required for spectrophotometry analysis, allowing reaction rate measurements for the colloids themselves.

Figure 5.11 shows the reaction rate of H_2O_2 decomposition per active surface area. This was generated by dividing the reaction rate obtained by UV-Vis spectroscopy by the expected surface area of platinum calculated by the known concentration of active Janus colloids. Data is reported in this format to allow assessment of the individual reaction rate required to produce enhanced motion for an active Janus colloids. For the platinum thicknesses given there is a linear relationship between catalyst thickness and the rate of H_2O_2 decomposition.

This data is presented alongside data given by Ebbens *et al.* [11]. It is shown that the reactivity for the solution grown active colloids is strikingly similar to that reported for the PVD prepared active colloids despite the difference in surface roughness.

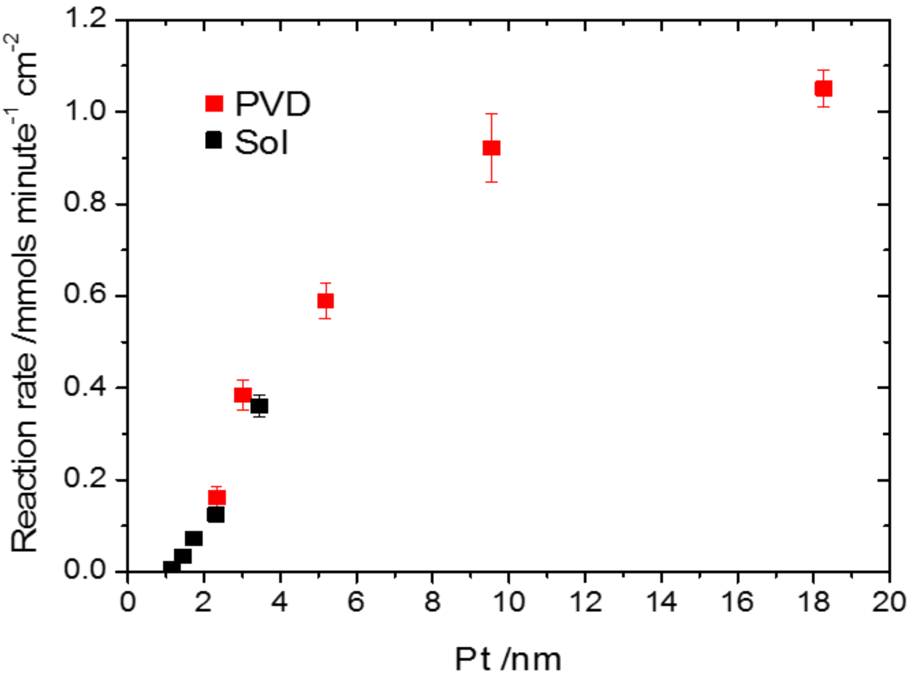

Figure 5.11 Reaction rate of decomposition of H_2O_2 per colloid active surface area for active Janus colloids prepared in solution (Sol) and by vapour deposition (PVD). Data points for PVD are taken from Ebbens *et al.*[11].

Due to the interest in deciphering the mechanism of motion in active colloids the effect of salt, specifically KNO_3, on velocity was investigated, presented in Figure 5.*12*. It is shown that, as reported for PVD prepared colloids, solution grown active colloids are also salt sensitive, with an inverse logarithmic dependency.

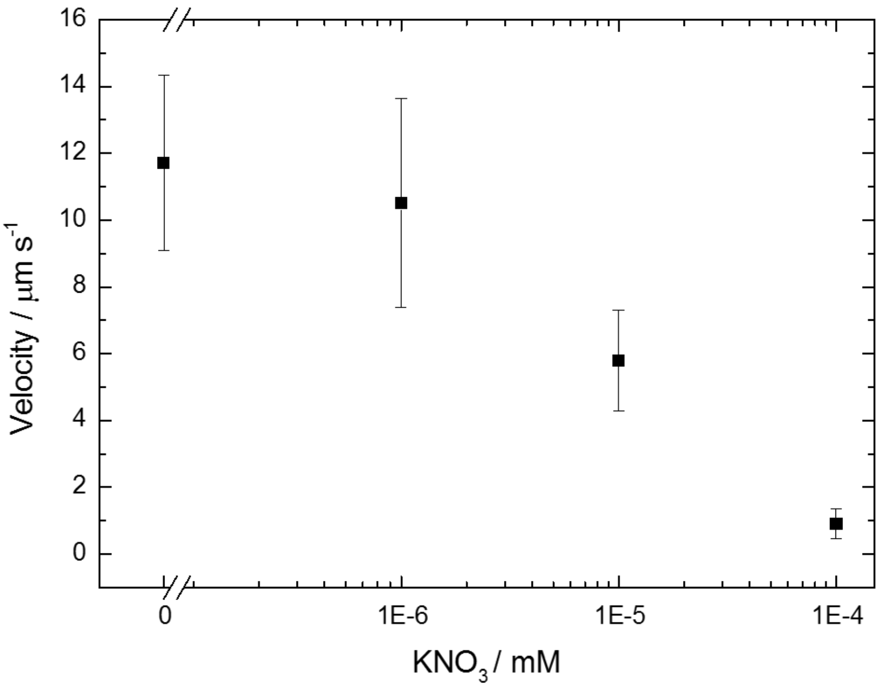

Figure 5.12 Velocity profile for solution prepared active colloids at a platinum thickness of 3.5 nm, in the presence of KNO_3

5.4 Conclusions

5.4.1 Synthesis

The use of silica here is advantageous due to the simplicity of producing large scales of monodisperse colloids with controllable diameters through control of initial starting conditions [19][20]. The required amine surface chemistry can be introduced through simple silanization techniques with APS, however a large library of silanes are commercially available allowing future studies to see the effect of surface functional groups on the platinum morphology[23].

While Pickering emulsions can be prepared from unmodified or APS modified Silica through selection of the complementary cationic/anionic surfactant, this dictates the surface chemistry of the masked, unmodified section. In this study APS modified colloids were used to form Pickering emulsions, the result is the amine surface functionality on the inactive exposed section that does not contain platinum. The motivation for this is the widespread use of amine functionality in biological binding such as for proteins, a prerequisite for the proposed mass transport applications and antibodies which could potentially allow biological recognition and specific targeting[28][29].

Silica offers other potential advantages in controllable porosity. Mesoporous silica is well documented and easily produced with tuneable pore sizes through small modifications to the Stober-Like processes used to make silica hard spheres[21]. Mesoporous silica has been extensively studied for its potential use in drug storage and delivery which is also a potential application for active Janus particles[22].

Despite the large number of steps, middling yield efficiency and use of solvents in comparison to PVD preparation of active Janus colloids, the synthesis route here offers easy scalability to the gram scale and a more efficient use of platinum potentially lowering costs and increasing accessibility for these devices to be utilised in emerging applications.

The surface roughness is reported here to be advantageous. Control of the topographical morphology could easily be manipulated though the initial chemical modification, with electrostatic binding of nanoparticles leading to a sparser coverage than a thiol chemical bonding [26]. It can be reasonably expected that the size and coverage of the initial seeds will affect the morphology after further growth. This could be exploited in future work to further enhance efficiency.

The penetrative depth of the silica in the Pickering emulsion was highly consistent to an approximate 1/3rd colloid submersion allowing 2/3^{rds} to be chemically modified. There are published reports controlling the penetrative depth of the silica, known as the "Janus balance" from the 1/3rd submersion observed here to approximately 2/3^{rds}

submersion[18][34]. This opens potential future work to explore the effect of the cap coverage on the enhanced motion at coverages <50 %.

5.4.2 Enhanced motion

Previously published reports on the phoretic mechanism of single metal Janus active colloids have proposed an electro-kinetic mechanism as the dominant force, in brief, this is suggested to be caused by a reactivity gradient in the metal cap due to an inherent thickness gradient from pole to equator generated by the line of sight PVD deposition on curved surfaces (chapter 1.4.3)[11].

In this solution based technique all exposed surface during synthesis has equal chance of metal addition and thus no such thickness gradient can be generated. Despite this, both qualitative assessment of the x,y displacement plots and quantitative analysis of the MSD and subsequent translational velocity we find no significant differences. This does not rule-out this being an electro-kinetic phenomena, as some recent theoretical models consider the electrokinetic effect to develop simply from charge separation. The electrophoretic argument is further enhanced by the susceptibility of the solution grown active colloids to salt. While electrophoresis cannot be ruled out, from the results found in this work, the thickness gradient in the cap does not seem to be essential.

While the surface morphology appears to make no difference in the phoretic mechanism, it is interesting to note that the solution prepared active colloids can be considered as more efficient, plateauing in velocity at around 2.3 nm of platinum. While this was initially thought to be caused by the comparatively roughened surface giving higher surface area and therefore increased reaction rate, direct comparison of reactivity per active surface area (Figure 5.11) revealed a similar activity for solution and PVD prepared coatings. This could be explained by the PVD thin film already having a large surface area to volume ratio. However the reason for the high velocity to reaction rate for the solution prepared active colloids in comparison to the PVD prepared active colloids remains an unanswered point of interest. The role of morphology on this is unclear.

5.4.3 Trajectory analysis

Howse *et al.* noticed that that the rotational diffusion (τ_R) of Janus active colloids prepared by PVD, decreased with increasing velocity (V), this was suggested to be caused by small induced angular velocities due to surface imperfections in the active cap. Here there is a striking similarity in the τ_R value between the solution based and the PVD prepared active colloids. The similarity in τ_R is found despite the surface morphological differences between the two preparation techniques. This suggests well documented reduction in τ_R for enhanced motion, is not structural in origin as first thought by Howse *et al.* [10]. Mathematically τ_R is given by Equation 5.1, in which we see the rotational diffusion is effected by the temperature T, viscosity η and the colloid radius R.

$$\tau_R = \frac{(8\pi\eta R^3)}{K_B T}$$

Equation 5.1

With the radius being fixed and assuming the solution is a Newtonian fluid, therefore discounting the possibility of viscosity changes due to Janus colloid velocity generated shear, τ_R is possibly reduced due to localised changes in T and subsequently η through the exothermic decomposition of H_2O_2. However this would require a local increase of 20 ^oC to solely account for the observed decrease of τ_R. Additional contributing factors such as a structure unrelated reaction non-uniformity on the catalyst surface causing imbalances on the resulting flow field could be present.

5.4.4 Reaction rate

The high yielding solution based preparation has allowed the production of sufficient concentrations of active Janus colloids to directly observe of the rate of reaction per colloid, as opposed to using flat substrates supported catalyst. More importantly this gives a benchmark for the necessary rate of reaction for enhanced displacement to occur for micron scale colloids and allows the assessment of potential catalytic reactions for suitability.

The reactivity of the active Janus colloids prepared by solution based synthesis increases near linearly with the estimated platinum thickness. Interestingly the velocity plateaus despite the increasing rate of reaction. This then shows an interesting state where velocity has seemingly changed from being linearly dependent on the rate of reaction to independent of the rate of reaction. Such limitations have been previously reported by Ebbens *et al.* who theorized different regimes for velocity exist based on the rate of reaction ($\frac{k1C_\infty}{k2}$) and the size of active colloid (R), [35]. These regimes are given in Figure 5.*13*, where it can be seen that with increasing reaction rate, a threshold is crossed (from regime I to II) where the velocity is no longer dependant on the reaction rate as the term for hydrogen peroxide concentration in the bulk (C_∞) is removed.

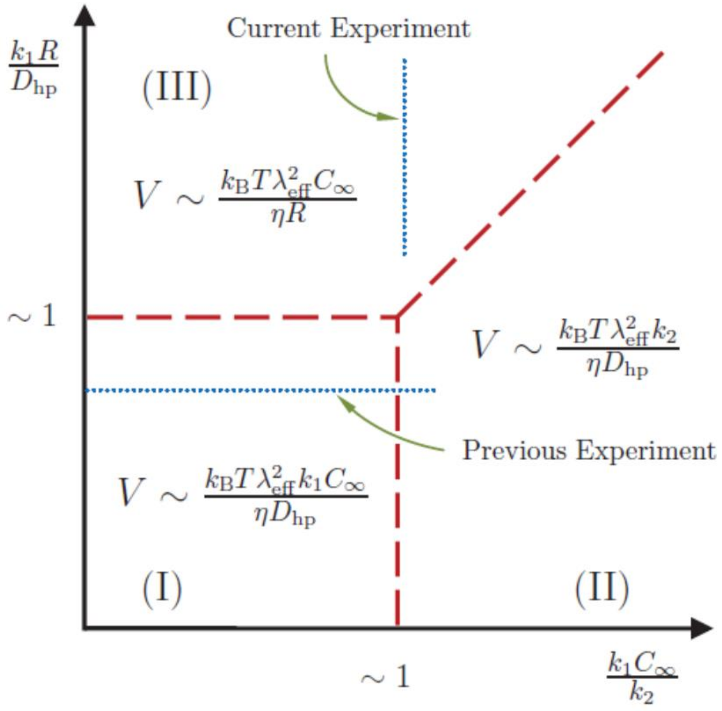

Figure 5.13 Theoretical velocity dependency regimes. Taken from [35]

5.4.4 Summary

This chapter presents a new solution based preparation method for active Janus colloids whose translational motion and enhanced displacement are highly comparable to PVD prepared Janus colloids. While the product percentage yield is middling due to the multiple steps involved and associated transfer losses, the high efficiency in the platinum usage and easy scalability make this an attractive alternative to PVD.

A thickness gradient across the active hemisphere, previously proposed as a propulsion producing mechanism, appears to be not essential for motion generation in the colloids produce here, and that the enhanced translational velocity has a linear dependence on the reaction rate but eventually plateaus and becomes independent of the reaction rate. The implication of this leads to the possibility of using any catalytic reaction for diffusiophoretic based enhanced displacement on the provision of a sufficient rate of reaction. The quantitative analysis of the reaction rate gives an indication of the catalytic reaction rate required to give enhanced displacement allowing catalytic reactions to be assessed for suitability causing enhanced displacement.

5.5 References

[1] J. Burdick, R. Laocharoensuk, P. M. Wheat, J. D. Posner, and J. Wang, “Synthetic nanomotors in microchannel networks: Directional microchip motion and controlled manipulation of cargo,” *J. Am. Chem. Soc.*, vol. 130, no. 26, pp. 8164–8165, 2008.

[2] S. Sundararajan, P. E. Lammert, A. W. Zudans, V. H. Crespi, and A. Sen, “Catalytic motors for transport of colloidal cargo,” *Nano Lett.*, vol. 8, no. 5, pp. 1271–1276, 2008.

[3] S. Balasubramanian, D. Kagan, C.-M. J. Hu, S. Campuzano, M. J. Lobo-Castañon, N. Lim, D. Y. Kang, M. Zimmerman, L. Zhang, and J. Wang, “Micromachine-enabled capture and isolation of cancer cells in complex media.,” *Angew. Chem. Int. Ed. Engl.*, vol. 50, no. 18, pp. 4161–4, Apr. 2011.

[4] W. Gao, X. Feng, A. Pei, Y. Gu, J. Li, and J. Wang, “Seawater-driven magnesium based Janus micromotors for environmental remediation.,” *Nanoscale*, vol. 5, pp. 4696–700, 2013.

[5] D. Patra, S. Sengupta, W. Duan, H. Zhang, R. Pavlick, and A. Sen, “Intelligent, self-powered, drug delivery systems.,” *Nanoscale*, vol. 5, no. 4, pp. 1273–83, Feb. 2013.

[6] W. Gao, R. Dong, S. Thamphiwatana, J. Li, W. Gao, L. Zhang, and J. Wang, “Artificial Micromotors in the Mouse’s Stomach : A Step toward in Vivo Use of Synthetic Motors,” *ACS Nano*, no. 1, pp. 117–123, 2015.

[7] S. Saha, R. Golestanian, and S. Ramaswamy, “Clusters, asters, and collective oscillations in chemotactic colloids,” *Phys. Rev. E - Stat. Nonlinear, Soft Matter Phys.*, vol. 89, pp. 1–7, 2014.

[8] B. R. Martin, D. J. Dermody, B. D. Reiss, M. Fang, L. A. Lyon, M. J. Natan, and T. E. Mallouk, “Orthogonal self-assembly on colloidal gold-platinum nanorods,” *Adv. Mater.*, vol. 11, no. 12, pp. 1021–1025, 1999.

[9] Y. Mei, G. Huang, A. a. Solovev, E. B. Ureña, I. Mönch, F. Ding, T. Reindl, R. K. Y. Fu, P. K. Chu, and O. G. Schmidt, “Versatile approach for integrative and functionalized tubes by strain engineering of nanomembranes on polymers,” *Adv. Mater.*, vol. 20, no. 21, pp. 4085–4090, 2008.

[10] J. Howse, R. Jones, A. Ryan, T. Gough, R. Vafabakhsh, and R. Golestanian, “Self-Motile Colloidal Particles: From Directed Propulsion to Random Walk,” *Phys. Rev. Lett.*, vol. 99, no. 4, p. 048102, Jul. 2007.

[11] S. Ebbens, D. A. Gregory, G. Dunderdale, J. R. Howse, Y. Ibrahim, T. B. Liverpool, and R. Golestanian, “Electrokinetic Effects in Catalytic Pt-Insulator Janus Swimmers,” pp. 1–5, 2013.

[12] A. I. Campbell and S. J. Ebbens, “Gravitaxis in spherical Janus swimming devices.,” *Langmuir*, vol. 29, no. 46, pp. 14066–73, Nov. 2013.

[13] L. Baraban, S. M. Harazim, S. Sanchez, and O. G. Schmidt, "Chemotactic behavior of catalytic motors in microfluidic channels," *Angew. Chemie - Int. Ed.*, vol. 52, no. 21, pp. 5552–5556, 2013.

[14] S. Das, A. Garg, A. I. Campbell, J. R. Howse, A. Sen, D. Velegol, R. Golestanian, and S. J. Ebbens, "Boundaries can steer active Janus spheres," *Nat. Commun.*, vol. 6, no. 8999, 2015.

[15] J. Orozco, B. Jurado-Sánchez, G. Wagner, W. Gao, R. Vazquez-Duhalt, S. Sattayasamitsathit, M. Galarnyk, A. Cortés, D. Saintillan, and J. Wang, "Bubble-propelled micromotors for enhanced transport of passive tracers," *Langmuir*, vol. 30, no. 18, pp. 5082–5087, 2014.

[16] L. Hong, S. Jiang, and S. Granick, "Simple Method to Produce Janus Colloidal Particles in Large Quantity," no. 12, pp. 9495–9499, 2006.

[17] A. Perro, F. Meunier, V. Schmitt, and S. Ravaine, "Production of large quantities of 'Janus' nanoparticles using wax-in-water emulsions," *Colloids Surfaces A Physicochem. Eng. Asp.*, vol. 332, no. 1, pp. 57–62, 2009.

[18] S. Jiang and S. Granick, "Controlling the geometry (Janus balance) of amphiphilic colloidal particles.," *Langmuir*, vol. 24, no. 6, pp. 2438–45, Mar. 2008.

[19] W. Stober and A. Fink, "Controlled Growth of Monodisperse Silica Spheres in the Micron Size Range," *J. Colloid Interface Sci.*, vol. 26, pp. 62–69, 1968.

[20] K. Nozawa, H. Gailhanou, L. Raison, P. Panizza, H. Ushiki, E. Sellier, J. P. Delville, and M. H. Delville, "Smart control of monodisperse Stöber silica particles: effect of reactant addition rate on growth process.," *Langmuir*, vol. 21, no. 4, pp. 1516–23, Feb. 2005.

[21] K. Zhang, L.-L. Xu, J.-G. Jiang, N. Calin, K.-F. Lam, S.-J. Zhang, H.-H. Wu, G.-D. Wu, B. Albela, L. Bonneviot, and P. Wu, "Facile large-scale synthesis of monodisperse mesoporous silica nanospheres with tunable pore structure.," *J. Am. Chem. Soc.*, vol. 135, no. 7, pp. 2427–30, Feb. 2013.

[22] I. I. Slowing, J. L. Vivero-Escoto, C.-W. Wu, and V. S. Y. Lin, "Mesoporous silica nanoparticles as controlled release drug delivery and gene transfection carriers," *Adv. Drug Deliv. Rev.*, vol. 60, no. 11, pp. 1278–1288, 2008.

[23] S. a Kulkarni, S. B. Ogale, and K. P. Vijayamohanan, "Tuning the hydrophobic properties of silica particles by surface silanization using mixed self-assembled monolayers.," *J. Colloid Interface Sci.*, vol. 318, no. 2, pp. 372–9, Feb. 2008.

[24] C. R. K. Rao and D. C. Trivedi, "Chemical and electrochemical depositions of platinum group metals and their applications," *Coord. Chem. Rev.*, vol. 249, no. 5–6, pp. 613–631, 2005.

[25] C. Graf and A. Van Blaaderen, "Metallodielectric Colloidal Core - Shell Particles for Photonic Applications," vol. 563, no. 19, pp. 524–534, 2002.

[26] B. S. Flavel, M. R. Nussio, J. S. Quinton, and J. G. Shapter, “Adhesion of chemically and electrostatically bound gold nanoparticles to a self-assembled silane monolayer investigated by atomic force volume spectroscopy,” *J. Nanoparticle Res.*, vol. 11, no. 8, pp. 2013–2022, 2009.

[27] Y. Jin, X. Kang, Y. Song, B. Zhang, G. Cheng, and S. Dong, “Controlled nucleation and growth of surface-confined gold nanoparticles on a (3-aminopropyl)trimethoxysilane-modified glass slide: A strategy for SPR substrates,” *Anal. Chem.*, vol. 73, no. 13, pp. 2843–2849, 2001.

[28] X. Liu, J. Xing, Y. Guan, G. Shan, and H. Liu, “Synthesis of amino-silane modified superparamagnetic silica supports and their use for protein immobilization,” *Colloids Surfaces A Physicochem. Eng. Asp.*, vol. 238, no. 1–3, pp. 127–131, May 2004.

[29] S. K. Vashist, E. Lam, S. Hrapovic, K. B. Male, and J. H. T. Luong, “Immobilization of antibodies and enzymes on 3-aminopropyltriethoxysilane-functionalized bioanalytical platforms for biosensors and diagnostics,” *Chem. Rev.*, vol. 114, no. 21, pp. 11083–11130, 2014.

[30] G. Dunderdale, S. Ebbens, P. Fairclough, and J. Howse, “Importance of particle tracking and calculating the mean-squared displacement in distinguishing nanopropulsion from other processes.,” *Langmuir*, vol. 28, no. 30, pp. 10997–1006, Jul. 2012.

[31] X.-D. Wang, Z.-X. Shen, T. Sang, X.-B. Cheng, M.-F. Li, L.-Y. Chen, and Z.-S. Wang, “Preparation of spherical silica particles by Stöber process with high concentration of tetra-ethyl-orthosilicate.,” *J. Colloid Interface Sci.*, vol. 341, no. 1, pp. 23–9, Jan. 2010.

[32] S. J. Ebbens and J. R. Howse, “Direct Observation of the Direction of Motion for Spherical Catalytic Swimmers,” *Langmuir*, vol. 27, no. 20, pp. 12293–12296, 2011.

[33] R. J. Archer, A. I. Campbell, and S. Ebbens, “Glancing Angle Metal Evaporation Synthesis of Catalytic Swimming Janus Colloids with Well Defined Angular Velocity,” *Soft Matter*, vol. 11, pp. 6872–6880, 2015.

[34] M. Williams, N. J. Warren, L. a. Fielding, S. P. Armes, P. Verstraete, and J. Smets, “Preparation of double emulsions using hybrid polymer/silica particles: New pickering emulsifiers with adjustable surface wettability,” *ACS Appl. Mater. Interfaces*, vol. 6, no. 23, pp. 20919–20927, 2014.

[35] S. Ebbens, M.-H. Tu, J. R. Howse, and R. Golestanian, “Size dependence of the propulsion velocity for catalytic Janus-sphere swimmers,” *Phys. Rev. E*, vol. 85, no. 2, p. 020401, Feb. 2012.

[36] R. a. Pavlick, S. Sengupta, T. McFadden, H. Zhang, and A. Sen, “A polymerization-powered motor,” *Angew. Chemie - Int. Ed.*, vol. 50, no. 40, pp. 9374–9377, 2011.

Chapter 6:

Influence of the active layer shape and coverage on the motion of active Janus colloids.

Chapter 6. Influence of the active layer shape and coverage on the motion of active Janus colloids.

6.1 Introduction.

In the production of single metal, active Janus colloids, the active region is typically a complete hemispherical coating. This is largely due to methods of production being limited by simple line of sight coating. Throughout this thesis however we have already observed an effect caused by change in the shape of the active layer. Chapter 4, demonstrated that changing the active cap shape had dramatic effects on the resulting trajectory.

In chapter 5, solution prepared colloids were approximately 2/3rds coated in platinum and with no expected thickness gradient in the active layer that occurs with e-beam deposition. The solution prepared active colloids with higher coverage of active catalyst were found to be more efficient in their reaction rate to resulting velocity. Following on from the discovery that the higher coverage coating led to more efficient self-phoretic colloids, in this chapter, an attempt is made is explore the effects of different coverages of the active surface layer, and observe the effects this has on the self-phoretic motion. This experimental work will tie in to several theoretical studies which have predicted the effect of active layer coverage on propulsion.

Theoretical models have already been used to describe idealised surface reactivity distributions. For both diffusiophoresis and electrophoretic models, Kreissl *et al*. have described the most efficient systems as being those with reactions concentrated at the poles as opposed to the full hemispherical coverage typically achieved through PVD (Figure 6.1). However it was acknowledged that the rate of reaction for pin point localisation would be impossibly high[1]. Despite this practical limitation, it establishes the idea that hemispherically platinum patterned active colloids used throughout this thesis are not in an optimised configuration.

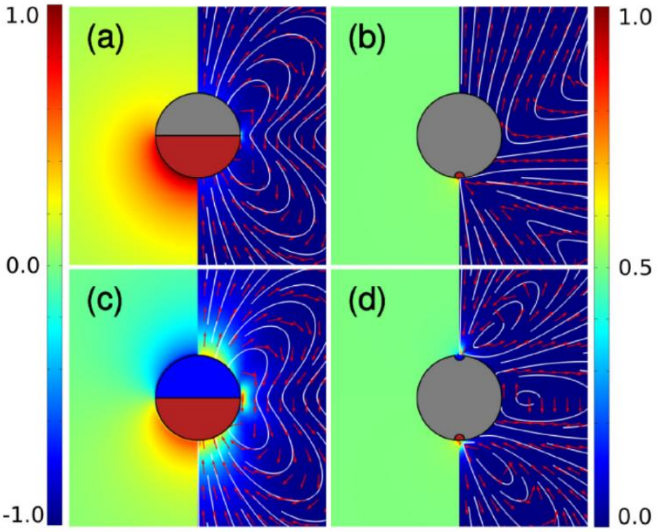

Figure 6.1 Concentration field and flow line diagrams for diffusiophoretic models (a and b) and electrophoretic models (c and d), for active Janus colloids with different active area coverage. Taken from Kreissl *et al.* [1].

Extending from the theory that increasing efficiency is inversely correlated to the area coverage of the active surface, Kreissl stated an assumption that fully coated, uniformly reactive colloids would produce no motion. This notion comes from the idea of uniform activity producing equal and opposite forces. However, this argument applied to simple thermal energy would not allow for even Brownian motion which arises in an energetically balanced system.

It is already reported that non-Janus, uniformly reactive particles can theoretically achieve motion under conditions where the symmetry is broken through other means. Michelin and Lauga described mathematically that homogenously reactive particles can still produce motion through geometric asymmetry. Colloids with geometric asymmetry produce an asymmetric concentration gradient across the body, additionally, differentially exposed surface area results in a net force effect which allows for phoresis[2].

Yoshinaga calculated the motion of uniformly active particles where the generated propulsive behaviour was granted through body deformation of a swimmer resulting in geometric asymmetry[3].

Even chemically and geometrically isotropic colloids have been shown mathematically to be able to undergo phoretic motion if their solute shell is disturbed by an impermeable barrier which again breaks the symmetry across the colloidal body[4].

Golestanian however reported that isotropic, axially symmetrical reactive colloids could still enter an anomalous 'super-diffusive' regime, triggered by the stochastic fluctuations of the reactants and products across the interface of the active colloid resulting in motion akin to an enhanced Brownian motion without being truly propulsive. However, it was stated that this anomalous super-diffusive regime would be a fleeting effect, only existing on the same time scale as the diffusion coefficient of the solute molecules around the active colloid, Figure 6.2 [5].

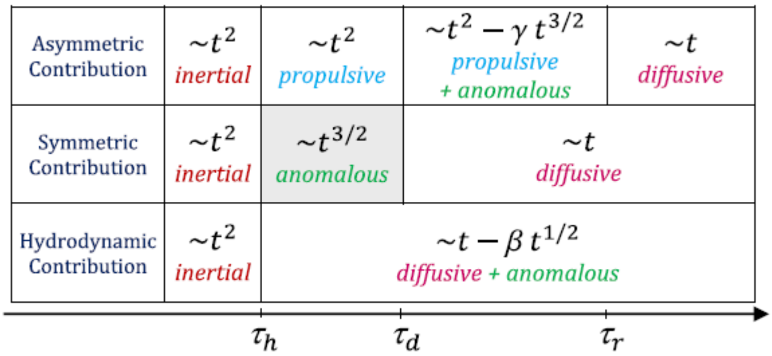

Asymmetric Contribution	$\sim t^2$ inertial	$\sim t^2$ propulsive	$\sim t^2 - \gamma\, t^{3/2}$ propulsive + anomalous	$\sim t$ diffusive
Symmetric Contribution	$\sim t^2$ inertial	$\sim t^{3/2}$ anomalous	$\sim t$ diffusive	
Hydrodynamic Contribution	$\sim t^2$ inertial	$\sim t - \beta\, t^{1/2}$ diffusive + anomalous		

Figure 6.2. Motion regiemes for active assymetric and symmetric colloids based on the time scale of the hydrodynamic relaxation time of the fluid (τ_h) diffusion coefficient of solute particles (τ_d) and rotational diffusion coeffciceint of the colloid (τ_r). Taken from Golestanian[5].

Another theoretical model from Michelin *et al*. proposes that for homogenously reactive, isotropic colloids, propulsive motion is still possible through 'spontaneous symmetry breaking' in the fluid caused by an instability in the solute advection.[6]

In this chapter experimental evidence is presented to contribute to the discussions of self-phoretic motion against the coverage of the active surface as described in the mathematical models presented above. Two different methods are utilised to control the coverage of available active cap area to study the effect on the velocity and efficiency of active Janus particles.

Firstly, sputter deposition is used for the physical vapour deposition of platinum as an alternate method to e-beam evaporation used in the preceding chapters. The key difference between e-beam and sputter deposition is the chamber pressure used in the process. As stated in chapter 2, e-beam deposition is conducted under extremely low pressures to limit the number of collisions the evaporated material experiences between the source and the substrate giving the highest mean free path (MFP) possible. This results in a line of sight coating which is typically exploited for catalytic Janus colloids. Sputter deposition however is conducted under an argon atmosphere and the MFP decreases accordingly[7]. It is expected that a decrease in the mean free path would allow a greater randomisation of the platinum path and therefore a higher chance of penetration into areas outside of the 'line of sight'. This principle is exploited by conducting coatings under a range of chamber pressures to influence the distribution of coating on the underside of the colloids. The aim is to compare the resulting velocity with platinum distribution profiles to test the theory of efficiency as described by Kreissil *et al*.[1]. According to the theory of Kreissl, an inverse relationship between increasing platinum distribution and velocity would be expected.

A major drawback to the sputter deposition in respect to the analysis of cap shape, is the limitation of coverage. As the colloid is situated on a substrate, the area at the interface between the colloid and the substrate is inaccessible and therefore will always result in an incomplete and asymmetrical coating.

As PVD techniques inherently result in asymmetrically modified particles the fabrication of symmetrically reactive colloids must come from a solution based synthesis where the surface of the colloids are equally exposed to platinum addition. As seen in chapter 5, asymmetry must in fact be purposely induced by masking. Successfully synthesised symmetrically reactive colloids are suspended in hydrogen peroxide and tested for any enhanced motion. This work contributes experimental work to the theoretical discussions by Golestanian and Michelin[5][6].

Experimental observations can also contribute to the discussion of the efficiency of active surface coverage. It is noted that the colloids prepared by sputter deposition cannot be directly compared to those prepared by chemical synthesis. To control the active surface coverage in the solution prepared colloids, PVD is used to deposit a hemisphere of inert, non-reactive material to create a mask and restore asymmetry.

6.2 Experimental

6.2.1 Materials

5 µm diameter polystyrene beads coated with platinum were supplied by Kisker-Biotechnology. Fluoromax beads 4.8µm diameter were supplied by Thermo Fisher Scientific. Platinum sputter target was supplied by Agar Scientific, hydrogen peroxide (30 wt%). Hexachloroplatinic acid hexahydrate (>37.5 % Pt basis), Ethanol (99.8 %), Formaldehyde (37 wt%) were supplied by Sigma Aldrich. Deionised (DI) water was obtained from an Elga Purelab Option filtration system (15 MΩ cm). Silica evaporation source was bought from Kurt J Lesker.

6.2.2 Sputter deposited active colloids.

Fluoromax colloids (4.8 µm) were suspended in an ethanol solution and spun coated onto a pre-cleaned glass substrate Figure 6.3a.

Sputter deposition was conducted using an Agar Scientific manual sputter coater. Sputter depositions were run at 0.04 mA, and at three different pressures (0.04 mbar, 0.08 mbar and 0.1 mbar argon atmosphere), between 5 and 15 seconds. The sputter coating unit does not contain a QCM or any method of directly quantifying the amount of deposited material. The deposition profile can however be measured on the platinum deficient 'holes' left on the substrate after removing the colloids by the previously mentioned scraping method discussed in chapter 2, to assess the platinum penetration into the areas hindered by the presence of the colloid.

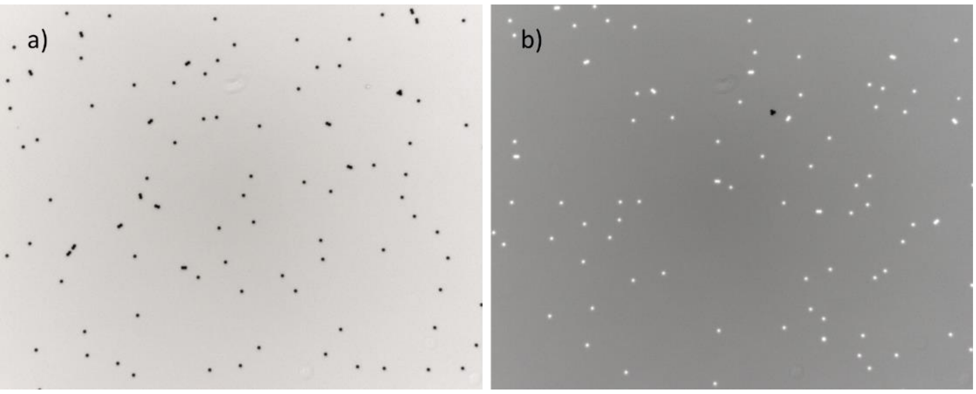

Figure 6.3. Optical image for a) spun coat 4.8um polystyrene colloids dispersed on a glass substrate before platinum deposition and b) colloids removed after platinum deposition revealing bright holes due to less obstruction in the transillumination where platinum layer is thinner due to shadowing by the colloids.

Atomic Force Microscopy (AFM) was used to quantify the thickness of the deposition layer AFM measurements were taken using a Bruker Dimension Icon AFM. The thickness was taken as being the difference between the fully exposed substrate and a zero point at the centre of the hole where no platinum is expected due to the contact between the colloid and the substrate during deposition.

An assumption was made that the thickness profile on the glass substrate directly correlates to the thickness profile on the colloid given that the glass substrate and colloid are equally exposed and should have an equal probability of the platinum interacting with the interface. The platinum distribution on the underside of the colloid is therefore inferred from height profile across the diameter of the shadowed hole where the penetration of the platinum is equally limited. An example of a height profile of a glass slide sputter coated with platinum is given in Figure 6.4. The dark region in the middle shows where a colloid has shadowed the deposition. The platinum distribution on the topside of the colloid is assumed to be of the same thickness as that of the flat substrate as both interfaces are equally fully exposed.

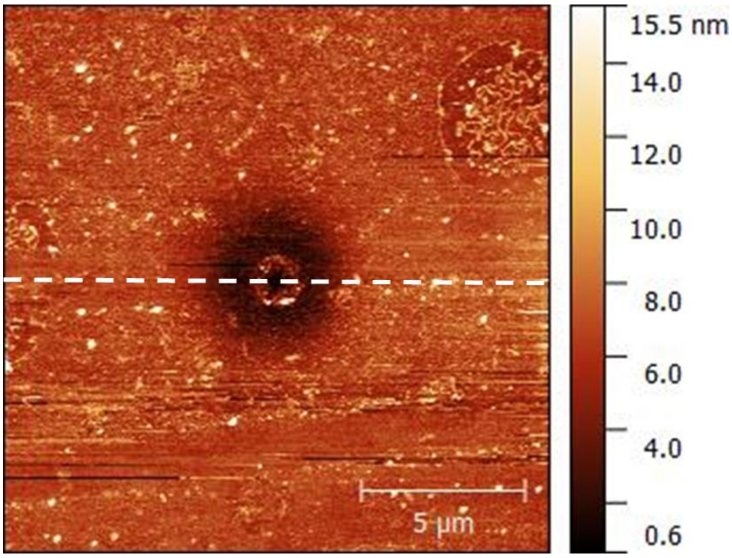

Figure 6.4. AFM profile of glass substrate coated in platinum by sputter deposition at 0.04 mbar argon chamber pressure for 7 seconds. The white dashed line indicates where the 2D height profile is recorded.

6.2.3 Symmetrically active colloids

Polystyrene beads (5 µm) with a homogenous platinum shell chemically deposited were supplied by Kisker-Biotech. Further platinum growth was conducted using the chemical synthesis method as discussed in chapter 5. Briefly, platinic acid (25 mM, 10 µL, 20 µL and 40 µL) was reduced by formaldehyde (2 % wt) in the presence of the Kisker supplied colloids. No seeding step was required due to the existing presence of platinum.

The thickness of the platinum shell of the colloids supplied by Kisker-Biotechnology was unknown, therefore the subsequent growth steps were also unknown. Sedimentation rate analysis is used to quantify the amount of platinum using Stokes' law equation for terminal velocity, Equation 6.1 Where V is the settling velocity, ρ' is the density of the colloid, ρ is the density of the fluid, η is the viscocity of the fluid, g is acceleration due to gravity and R is the radius of the settling colloid. Extremely dilute concentrations of colloids were used to prevent colloid-colloid interactions through backflows and treat each colloid as in isolated system for the purpose of calculating the velocity due solely to settling[8]. The colloid settling rates were recorded optically using a horizontal microscope set up and a Pixelink camera at 33 fps for 30 seconds and tracked as described in chapter 2.

$$V = \frac{2}{9}\frac{(\rho' - \rho)}{\eta} g R^2$$

Equation 6.1

Asymmetry was introduced by e-beam evaporation of a SiO_2 layer which is unreactive towards hydrogen peroxide. The symmetrically active Kisker beads and Kisker beads with further platinum growth were spun coat on to a glass substrate and coated as described in chapter 2. SiO_2 was chosen as the masking material must be non-conductive to prevent formation of electrochemical cell such as that produced by Paxton *et al*.[9].

6.2.4 Particle tracking

All particle tracking was conducted as described in chapter 2.

6.3 Results and Discussion

6.3.1 Surface coverage by sputter deposition.

AFM profiles were produced by measuring 5 to 6 holes across the surface of the substrate from platinum films deposited at 0.04, 0.08 and 0.10 mbar of argon,presented below in Figure 6.5, Figure 6.6 and Figure 6.7 respectively. The height profiles were aligned by their lowest value (zero point) and averaged to produce averaged profiles. The profiles of the individual data were highly consistent. Deposition rate was highest for the higher argon pressures of 0.08 and 0.1 mbar

The diffusion of the platinum to the underside of the colloid appears to be unaffected by the pressure as the gradient in the height profile between the highest level (the flat substrate) and the lowest, zero height point appears to be equal for argon pressures of 0.04, 0.08 and 0.1mbar, shown in Figure 6.5, Figure 6.6 and Figure 6.7 respectively. However such a gradient suggests penetration to the underside does occur though at a lessened rate compared to the fully exposed substrate. Active colloids with active surface areas greater than 50% are therefore successfully produced.

The aim of using different pressures during deposition of platinum was to create a significant difference in surface coverage, however this was not achieved. Differences between the depositions conducted at different pressure appears to come from an unexpected phenomena. Significant height peaks occur at either side of the zero point, representing a ring of platinum build up around the base of the bead, highlighted below in Figure 6.5, Figure 6.6 and Figure 6.7 by black arrows. While these peaks occur for all pressures they grow faster with higher pressures, reaching 8 nm in height for the deposition at 0.01 mbar.

This unusual accumulation of platinum around the base of the colloid may stem from an unusual diffusion of the platinum in the gas. The base of the colloid would likely act as a narrow cavity where the chance of interaction between the diffusing platinum and the interfaces increases rapidly. Figure 6.8 shows schematically how the platinum build over time on the substrate around the colloid and the resulting colloid coverage expected is presented on the right hand side.

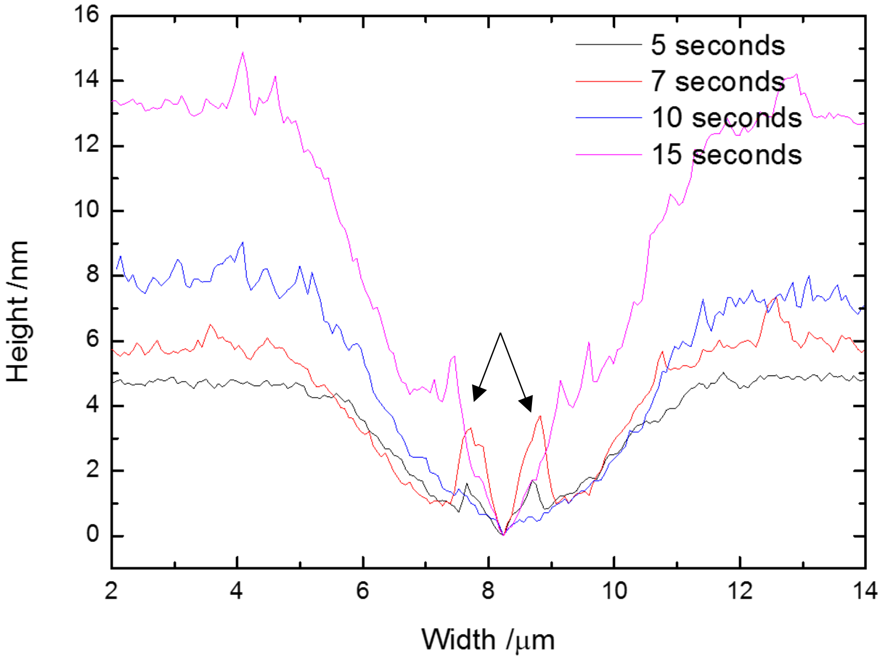

Figure 6.5. AFM height profiles over the 5 µm colloid shadowed hole at argon pressure of 0.04 mbar. Black arrows indicate a platinum build up around the contact point between the colloid and the glass slide.

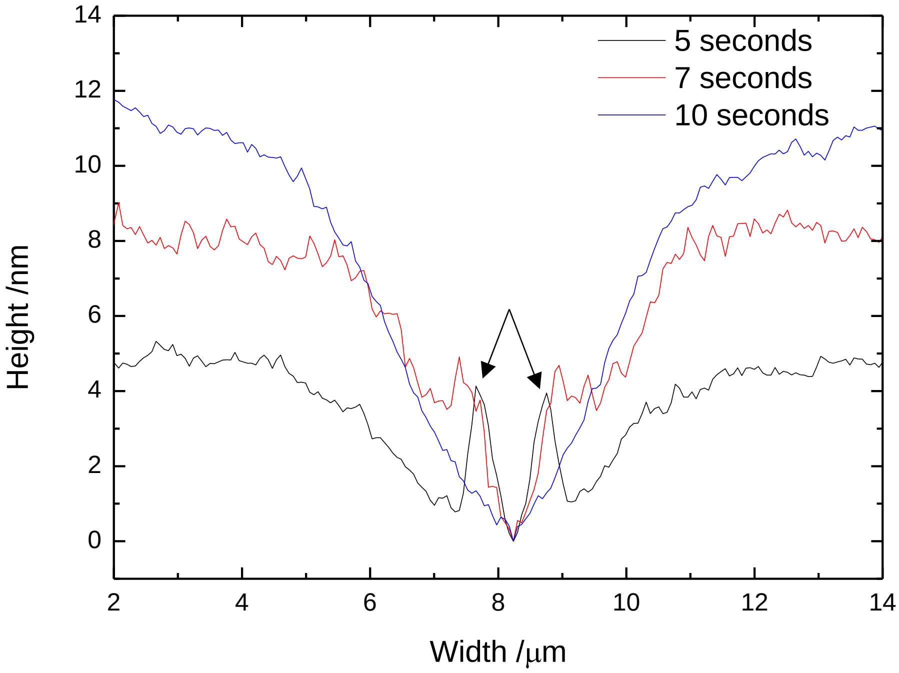

Figure 6.6 AFM height profiles over the 5 µm colloid shadowed hole at argon pressure of 0.08 mbar. Black arrows indicate a platinum build up around the contact point between the colloid and the glass slide.

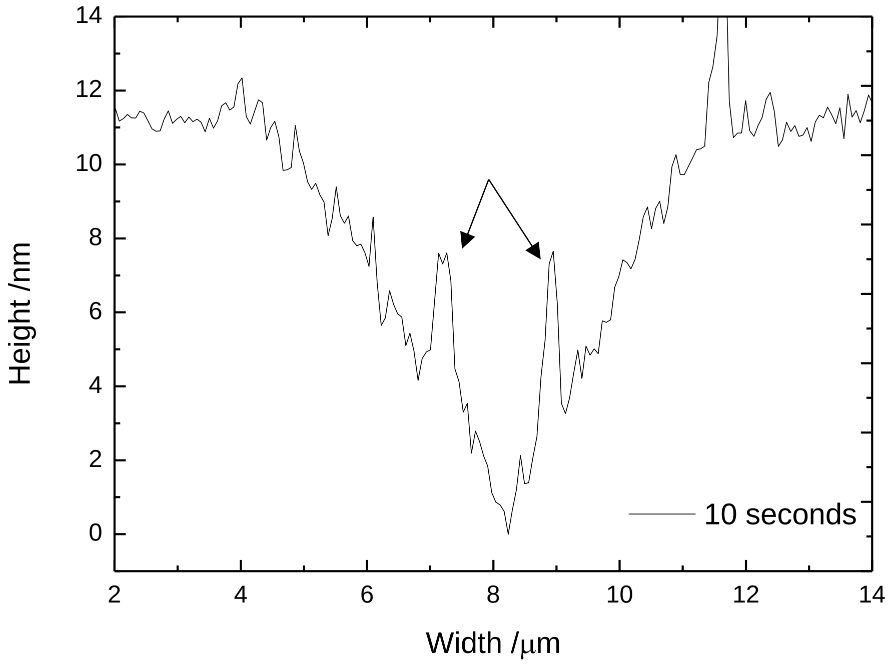

Figure 6.7 AFM height profile over the 5 µm colloid shadowed hole at argon pressure of 0.10 mbar. Black arrows indicate a platinum build up around the contact point between the colloid and the glass slide.

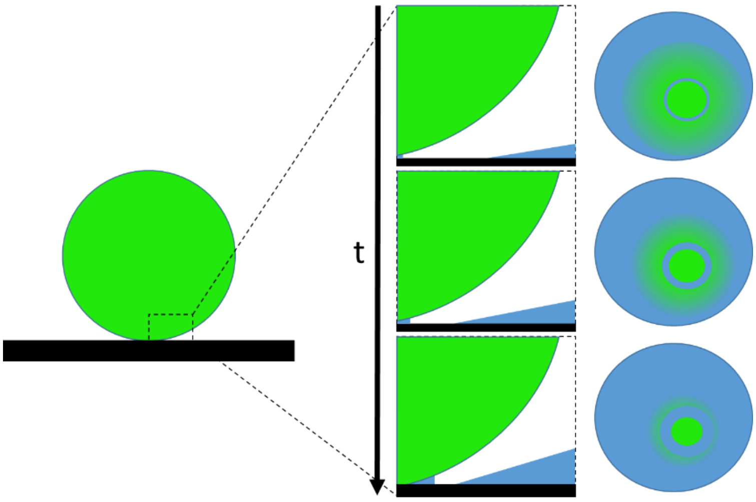

Figure 6.8. Schematic of how platinum (blue) grows under the shadowed region over time and the resulting colloid coverage suspected is shown on the right. The base colloid is shown in green and the glass slide in black.

Two factors which are known to influence the propulsion velocity for catalytic swimmers are the platinum thickness and the roughness of the active platinum layer[10],[11]. Here the velocity is plotted against the platinum thickness, Figure 6.9, and the surface roughness, Figure 6.10, as calculated through AFM on the unobstructed platinum coated substrate.

Figure 6.9 Shows that the velocity of active colloids in 10 wt% H_2O= increases linearly with platinum thickness, up to a thickness of 8 nm. A linear dependence of velocity on the platinum thickness is expected as previously published work by Ebbens, *et al.* has reported [10]. However, an unexpected decrease in velocity occurs with platinum thicknesses beyond 8 nm.

Figure 6.10 shows the velocity of active colloids in 10 wt% H_2O_2 increasing linearly with the surface roughness. The trend correlates well across the entire series of results. The positive gradient between roughness and velocity appears to be slightly higher for the active colloids prepared under argon atmospheres of 0.08 mbar as opposed to 0.04 mbar.

From these results it would appear that surface roughness is the main measurable parameter of the catalytic coating that correlates consistently to propulsion speed.

To further illustrate this, the platinum thickness was plotted against the surface roughness, given in Figure 6.11. Figure 6.11 overlaps with Figure 6.9 nearly identically. The only exception appear to be in the platinum films at 8nm prepared at 0.04 and 0.08 mbar with the former producing a rougher film than the latter but the velocity of the active colloids produced under these conditions are not significantly different. These results are in agreement with the previously found, higher efficiency of active colloids produced by solution synthesis as opposed to e-beam prepared active colloids, discussed in chapter 5, where the solution synthesised platinum film was found to be rougher then the e-beam deposited film.

Figure 6.11 also shows that the surface roughness of the sputter deposited platinum films appears to be determined by film thickness, and largely unaffected by chamber pressure.

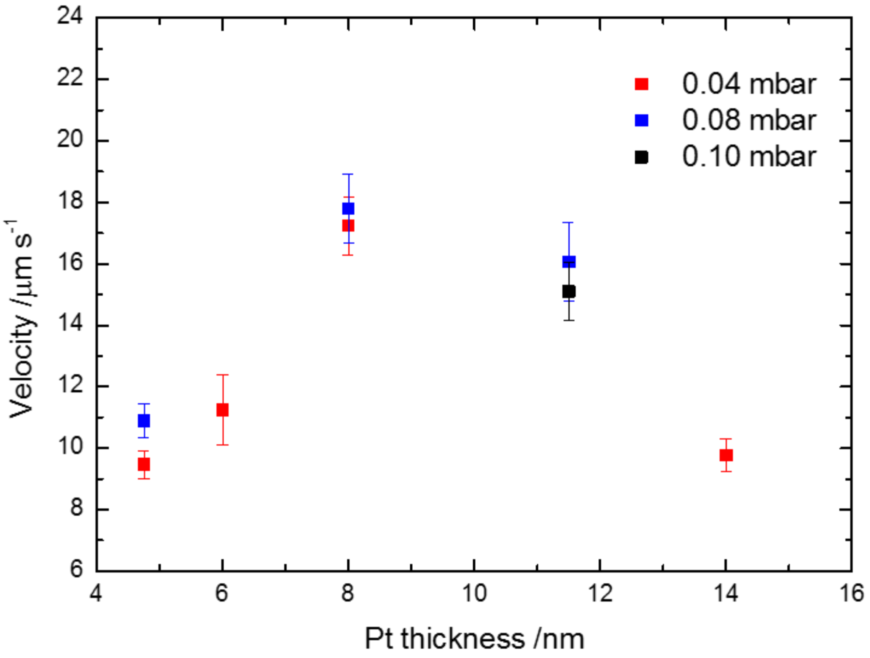

Figure 6.9 Velocity of active colloids (5 µm) plotted against the platinum thickness for sputter deposition run at 0.04, 0.08 and 0.10 mbar.

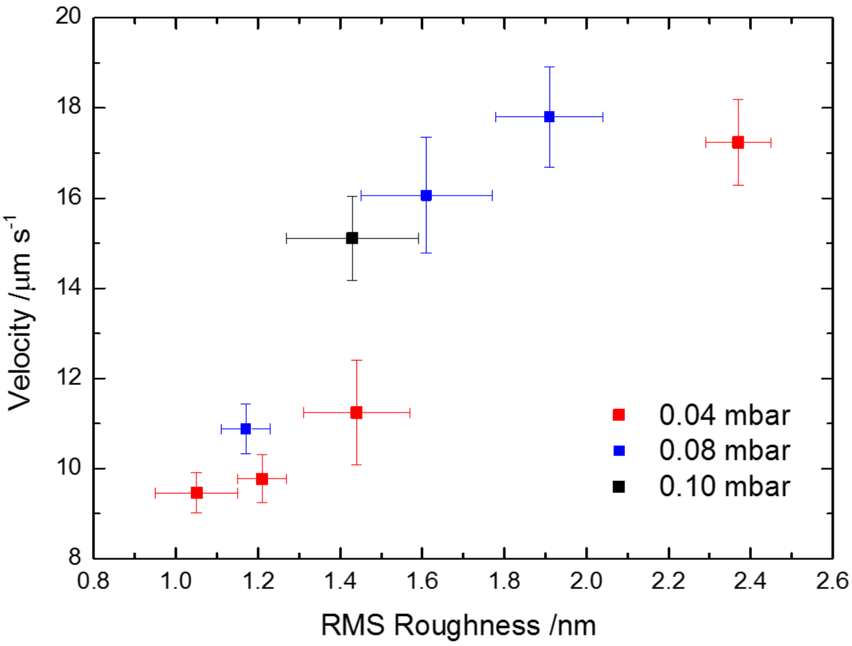

Figure 6.10. Velocity of active colloids (5 µm) plotted against surface roughness for sputter deposition run at 0.04, 0.08 and 0.10 mbar

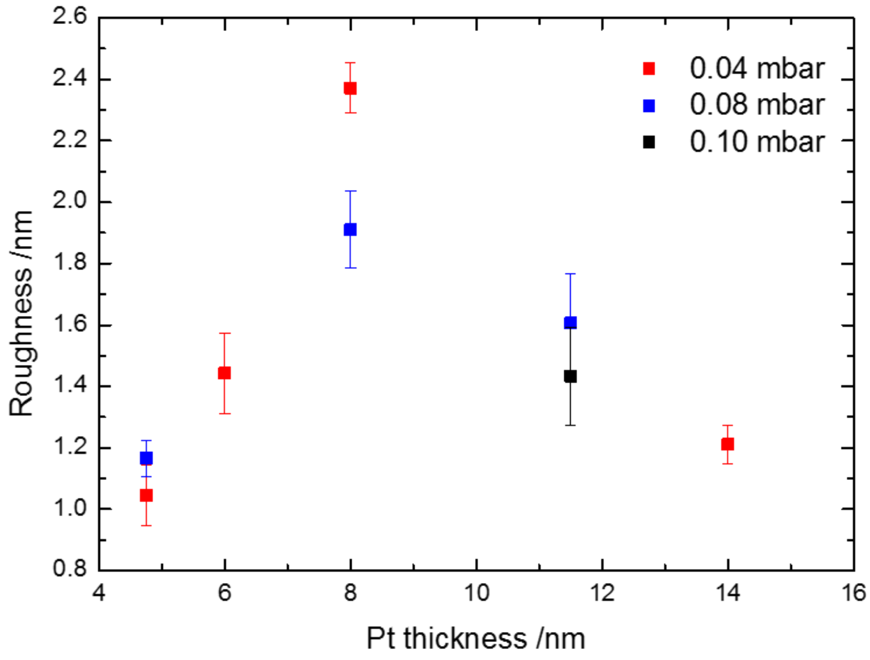

Figure 6.11. Roughness plotted against platinum thickness for sputter deposition run at 0.04, 0.08 and 0.10 mbar.

While the surface roughness appears to be the dominating factor in the resulting velocity of the active colloids, it is also useful to compare the platinum distribution on the colloids.

Figure 6.12 gives the AFM profile of the hole after sputter coating for five seconds under 0.04 and 0.08 mbar of argon. After five seconds, the Pt thickness is built up to approximately 4.75 nm in both cases. A slight difference in roughness is acknowledged with the films having a calculated RMS roughness of 1.05 (±0.1) and 1.17 (±0.06) nm for 0.04 and 0.08 mbar respectively.

The peak thickness around the zero point is considerably higher for the deposition at 0.08 mbar with the ring reaching approximately 4.0 nm, a similar thickness to the unobstructed film. The peak ring at the base of the zero point for deposition at 0.04 mbar reaches only approximately 1.5 nm.

As shown in Figure 6.11, the deposition at 0.08 mbar produces slightly rougher films than those produced at 0.04 mbar at platinum thickness of 4.75 nm. From Figure 6.10, we would then expect the active colloids produced at 0.08 mbar to be have a slightly higher velocity than those produced at 0.04 mbar. This is in line with the observed slight higher velocity for the 0.08 mbar produced active colloids to the 0.04 mbar produced colloids at 4.75 nm.

The difference in velocity between the active colloids produced between 0.04 mbar and 0.08 mbar to a thickness of 4.75 nm can be explained by surface roughness alone. The presence of the more defined, built up ring on the underside of the colloids produced under 0.08 mbar in comparison to 0.04 mbar therefore makes no apparent difference to the velocity at a platinum thickness of 4.75 nm.

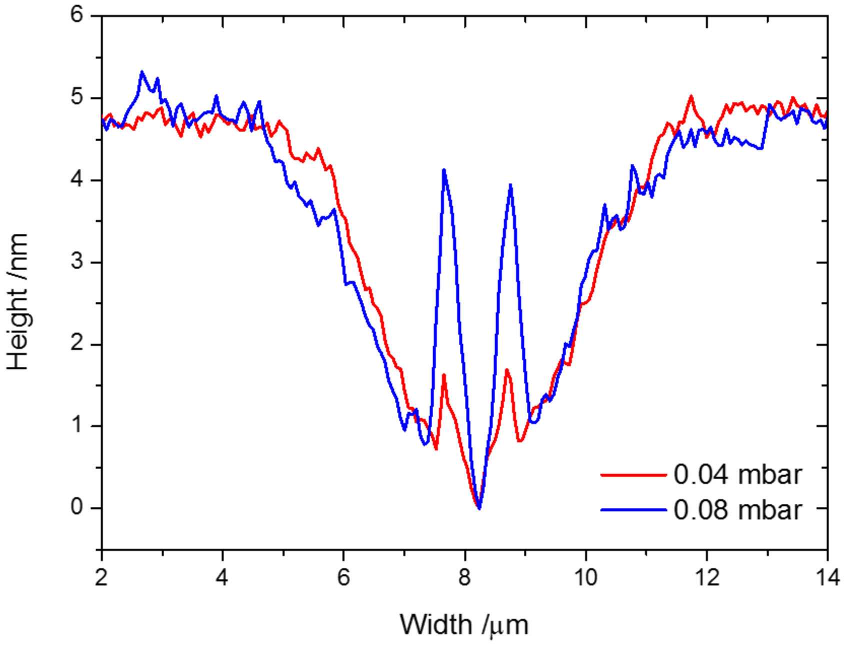

Figure 6.12 AFM height profile over the colloid shadowed hole for deposition at 0.04 and 0.08 mbar for 5 seconds.

Figure 6.13 gives the AFM profile of the hole after sputter coating for 10 and 7 seconds under 0.04 and 0.08 mbar of argon respectively. The resulting Pt layer is approximately 8 nm thickness on the unobstructed substrate.

As can be seen from Figure 6.11, the roughness difference between films produced at 0.04 and 0.08 mbar is significantly different at 2.37 (±0.08) and 1.91 (±0.13) nm.

The AFM profiles of the holes show an obvious difference in the coverage between the two chamber pressures. At 0.04 mbar, the thickness raised ring around the base is no longer visible, the reason for this is unclear as all other iterations contain this raised profile. Speculatively, it could be present but harder to detect if it has not grown but the overall thickness has nearly doubled. Contributing to this argument is the raised profile around the base at 0.08 mbar has not increased in height from 4.75 to 8 nm film growth on the substrate. The raised profile around the base at 0.08 mbar has seemingly rather grown outwards becoming less defined as a separate spike, has began to blend into the overall profile.

The velocity of the active colloids deposited with platinum at 10 and 7 seconds under a chamber pressure of 0.04 and 0.08 mbar respectively are not significantly different at 17.23 and 17.80 μms^{-1} for 0.04 and 0.08 mbar respectively.

This may be a surprising result given the significantly higher roughness for the film produced at 0.04 mbar.

This may be a subtle indication that rather being counterproductive the additional platinum has led to an increase in efficiency.

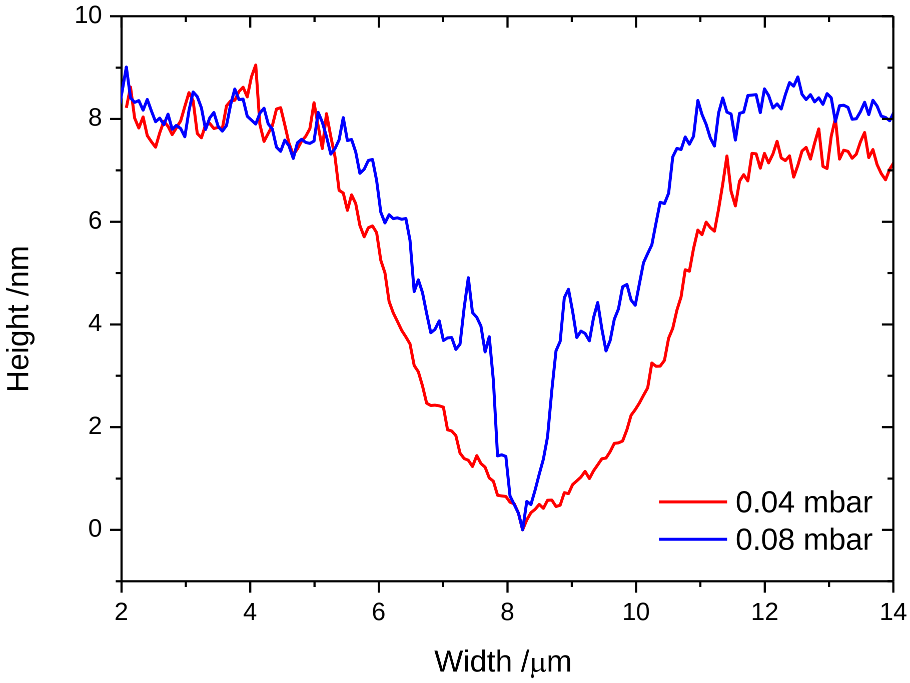

Figure 6.13 AFM height profile over the colloid shadowed hole for deposition at 0.04 and 0.08 mbar for 10 and 7 seconds respectively.

Figure 6.14 gives the AFM profile of the hole after sputter coating for 10 seconds under 0.08 and 0.10 mbar of argon. The resulting Pt layer is approximately 11.5 nm thick on the unobstructed substrate.

The roughness profile of the two deposited films are similar at 1.61 (±0.16) and 1.43 (±0.16) nm for 0.08 and 0.10 mbar respectively as illustrated in Figure 6.11.

Again, the most striking difference between the two prepared films is the presence of the raised profile around the base of the zero point for the deposition at 0.10 mbar and the absence of these peaks at 0.08 mbar. The reason for the absence of the peaks around the base at 0.08 mbar is unknown but again may be explained by the relative height difference as the unobstructed substrate grows in height but the peaks around the base do not.

The velocity profile of the active colloids at 11.5 nm prepared at 0.08 and 0.10 mbar are similar at 16.06 (±1.28) and 15.1 (±0.93) μms^{-1} respectively. The small difference in these velocities correlates with the small difference in the roughness profile

From these results it cannot be concluded that the cap shape makes any clear difference to the velocity.

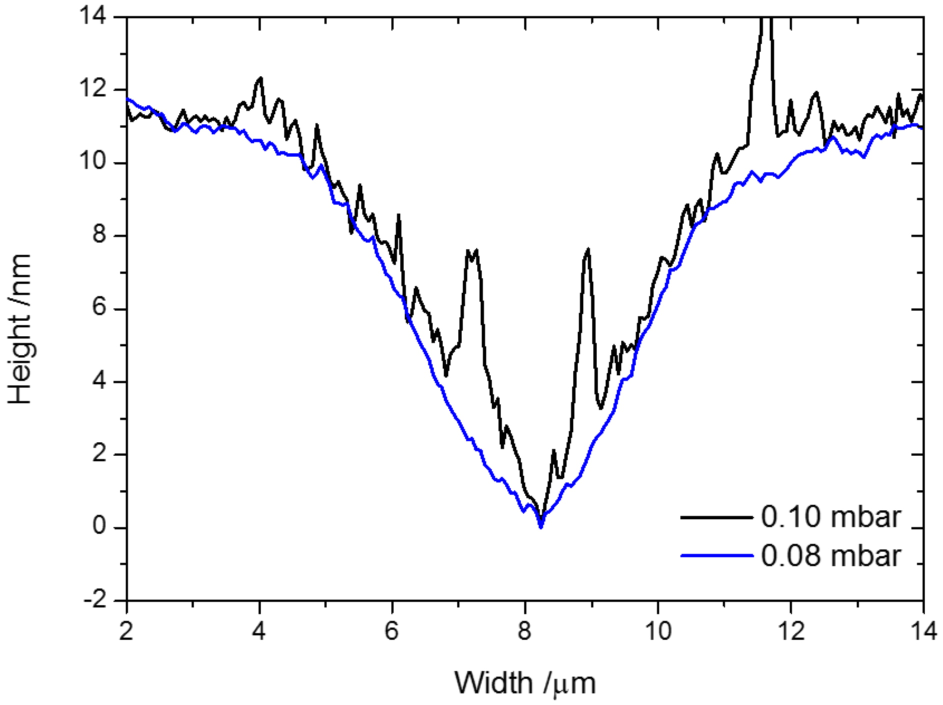

Figure 6.14. AFM height profile over the colloid shadowed hole for deposition at 0.08 and 0.10 mbar for 10 seconds.

6.3.2 Symmetrically reactive colloids.

Symmetrically reactive colloids supplied by Kisker-Biotech, were confirmed to be symmetrically deposited with platinum by backscatter SEM, Figure 6.15. The backscatter allows a high contrast between the base polystyrene and the platinum shell allowing defect sites to be highly visible. It is noted a small percentage of the colloids did have small defect sites as are visible in Figure 6.15a, resulting in a small portion of non-symmetrically reactive colloids.

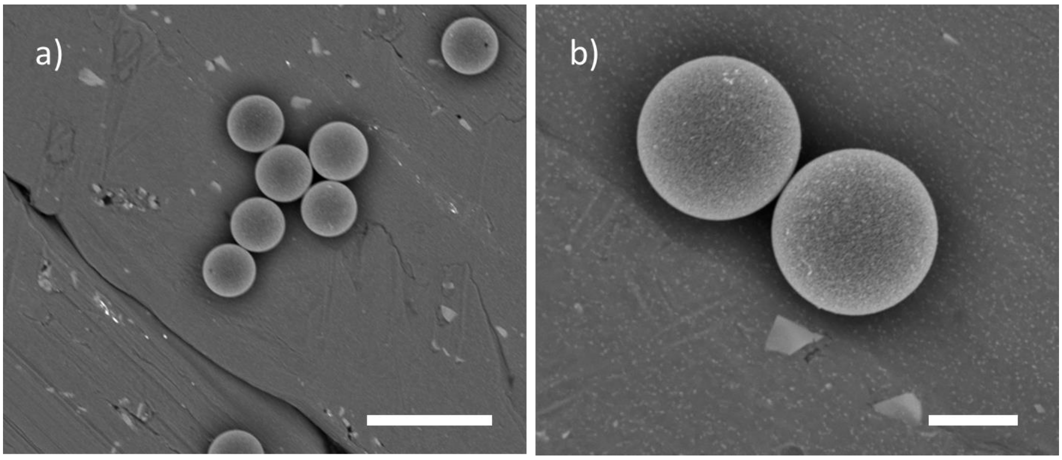

Figure 6.15.Symmetrically platinum coated colloids supplied by Kisker-Biotechnology. Scale bar represents 10 and 2.5 µm a and b respectively.

The unknown quantity of platinum on the Kisker beads was assessed by settling analysis by Stoke's equation as stated in the method section above. To show the validity of the experimental analysis, settling analysis was conducted on polystyrene colloids of known size (4.8 µm diameter) and the settling velocity was compared to the theoretical value of 0.77 µm s^{-1}. Figure 6.16 gives the experimentally observed settling velocity of 0.79 (±0.083) µm s^{-1} compared to the theoretical value which are in good agreement. With the validity of the settling rate method confirmed, the settling rate velocity of the Kisker supplied colloids and the Kisker supplied colloids grown with a further 10, 20 and 40 µL of 25 mM H_2PtCl_6 reduced on to the surface were found to be 1.30 (± 0.055), 1.51 (± 0.11), 1.86 (± 0.087) and 2.23 (± 0.094) µm s^{-1} respectively, Figure 6.17.

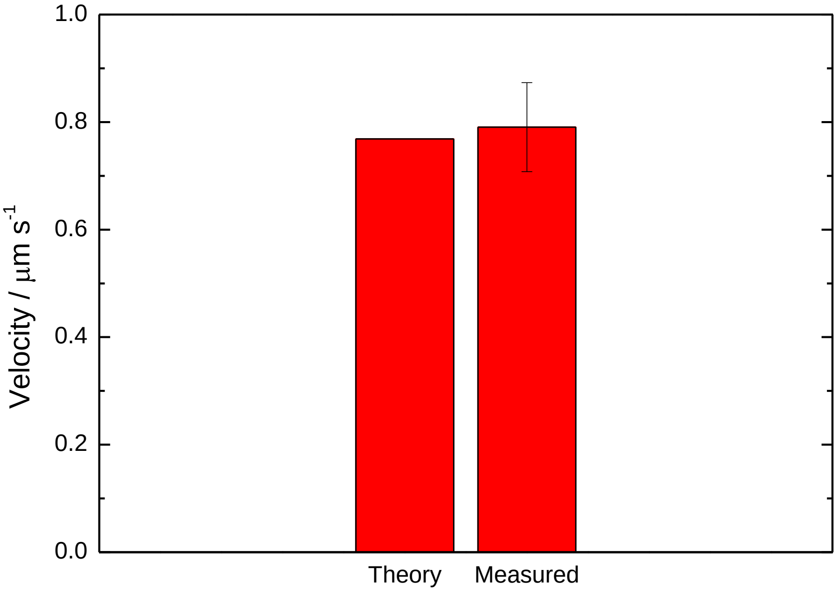

Figure 6.16. Settling velocity calculated by Stoke's law (theory) and experimentally measured for polystyrene colloids at 4.8 μm diameter.

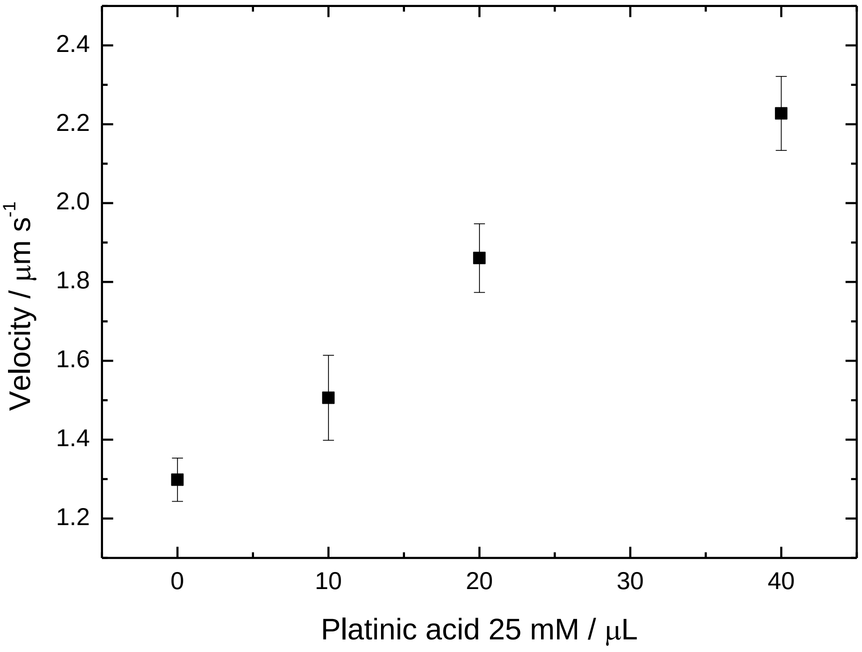

Figure 6.17. Settling velocities for Kisker-Biotech supplied 5μm diameter, platinum coated colloids with further grown platinum layer colloids.

The growth of the platinum layer has two effects, both increasing the radius and the density. As both these values contribute to the velocity according to the Stokes' equation. To convert the experimentally found settling velocity to the thickness of the platinum shell the relationship between the two is calculated using the theoretical output from Stoke's equation between 0 and 10 nm, Figure 6.18. The associated increase in density due to platinum is calculated from the increase in volume for the new radius and the density of platinum (21.45 g cm^{-3}). The new radius and density is used to calculate the settling velocity and a linear fit applied. Using the linear fit equation (y=a+bx) the experimental velocity can be converted to the associated platinum thickness, presented in Table 1.

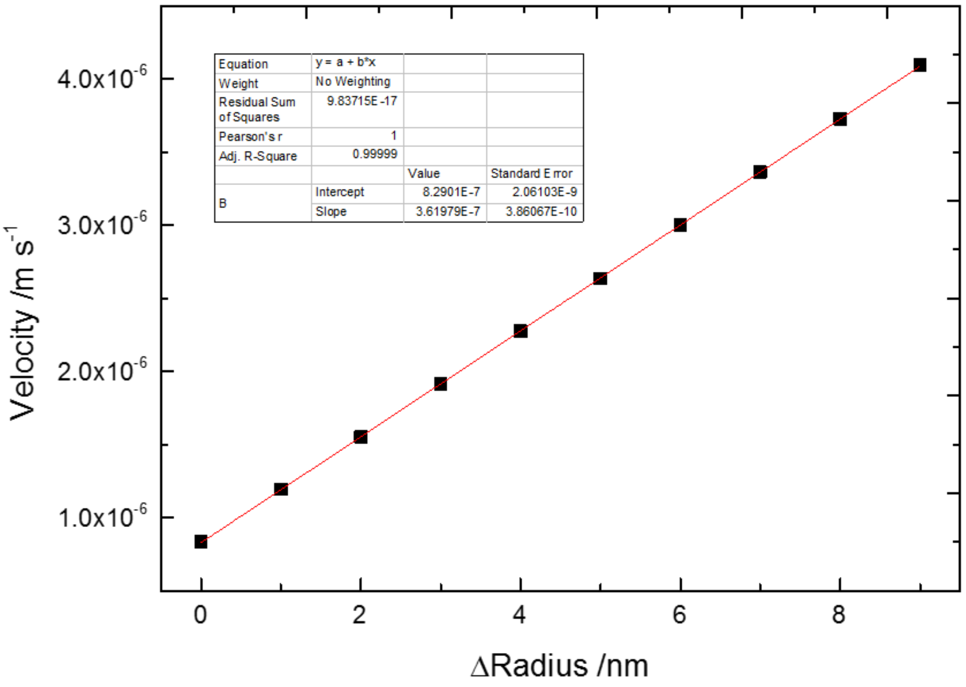

Figure 6.18 Calculated relationship between the change in radius due to platinum and the settling velocity.

Table 1. Pt shell thickness calculated from settling velocity and respective standard error (SE)

H_2PtCl_6 (µL)	Settle Velocity (µm s^{-1})	Settle velocity SE (µm s^{-1})	Pt Thickness (nm)	Pt thickness SE (± nm)
0	1.30	0.05	1.30	0.15
10	1.51	0.11	1.87	0.30
20	1.86	0.09	2.85	0.24
40	2.23	0.09	3.87	0.26

The validity of the masking experiments to restore asymmetry by depositing an inert layer over the catalyst was tested on 2 µm diameter Janus colloids coated hemispherically with platinum (10 nm) by e-beam deposition with masked sets followed by deposition of SiO_2 (40 nm) directly on top of the platinum active layer. The velocity of the active colloids with and without the masking SiO_2 layer was recorded in a solution of 10 wt% H_2O_2. The velocity of the unmasked self-phoretic colloids was found to be 10.25 (± 0.32) µm s^{-1} and with the masking layer deposited a significant reduction in velocity to 2.30 (± 0.18) µm s^{-1} was found, representing a reduction in velocity of 77.6 %, Figure 6.19. It is surprising however that any velocity remains to which it must be concluded that the SiO_2 is not completely impermeable, however the reduction is significant enough for the masking layer to be considered a relevant method for breaking the symmetrical reactivity of the Kisker supplied colloids.

The base Kisker supplied colloids with no further platinum growth were found to only undergo Brownian motion in hydrogen peroxide (10 wt%). The Kisker supplied colloids with further platinum growth were found to undergo self-phoretic motion with velocities proportional to the platinum thickness. From these results we can conclude that symmetrically active colloids can indeed undergo propulsive behaviour. The velocity of these symmetrically reactive colloids reaches up to 4.06 (± 0.30) µm s^{-1} at a platinum thickness of 3.87 nm. While this velocity is significantly lower than that prepared by platinum sputter deposition at 4.75 nm (Figure 6.9), the difference in thickness and the unknown surface roughness of the Kisker supplied colloids makes any direct comparison with the sputter prepared colloids invalid.

The Kisker supplied colloids with and without additional platinum growth, masked with 40 nm of SiO_2, found that the velocity decreased by approximately 60 %, 63 % and 20 % for platinum shells of 1.87 nm, 2.85 nm and 3.87 nm respectively, Figure 6.20. The lower reduction in velocity as compared to the e-beam prepared active colloids is not unexpected as only half of the available active area can be masked.

Example x,y tracks are presented in Figure 6.21 to show the self-phoretic motion is not caused by flow: which exhibit a continuous unidirectional motion[12].

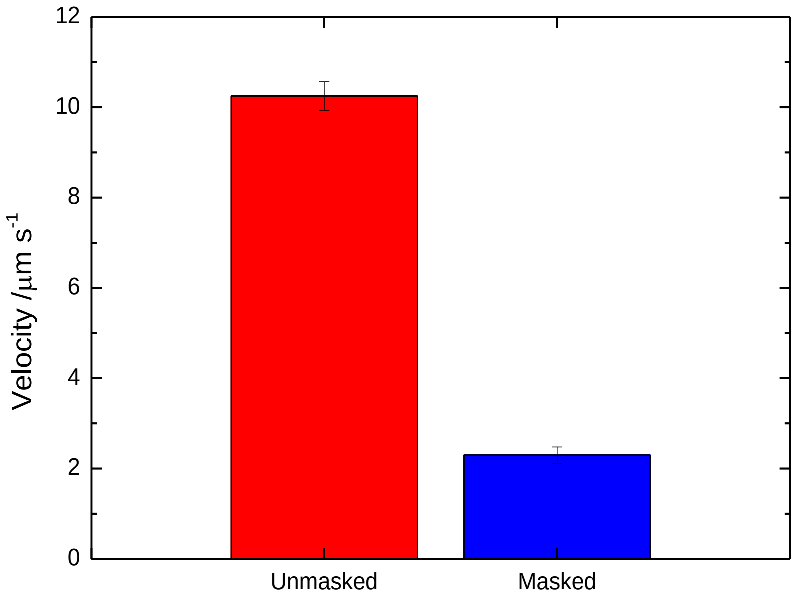

Figure 6.19. Velocity for active colloid coated with 10 nm of platinum by e-beam deposition without (unmasked) and with (masked) a 40 nm SiO_2 inert masking layer directly deposited on top of the platinum active layer.

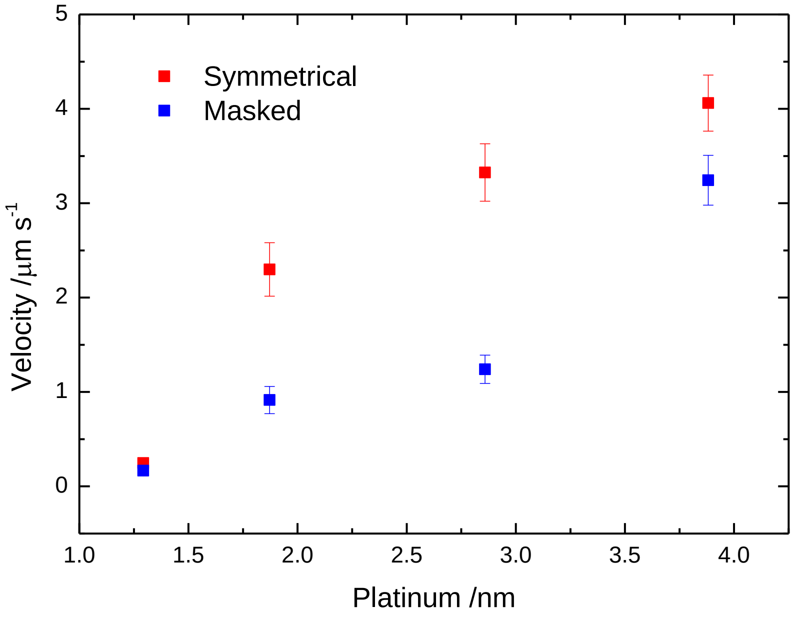

Figure 6.20. Velocity profile of uniformly active Kisker colloids with increasing platinum shell thickness (symmetrical) and Velocity profile after depositing a 40nm SiO_2 hemisphere.

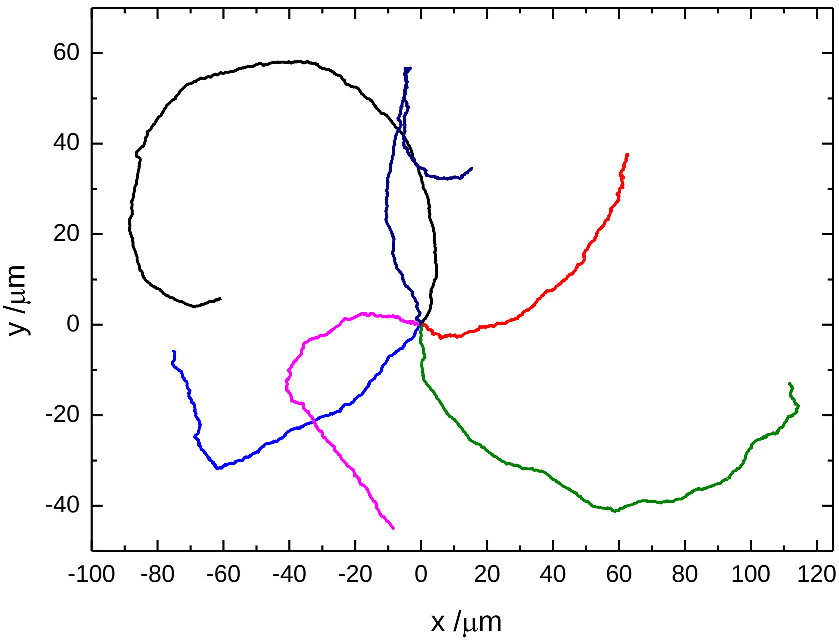

Figure 6.21 Example x,y plots of Kisker colloids with a platinum shell of 3.87 nm in 10 wt % H_2O_2 over 30 seconds.

It can be easily seen from Figure 6.21 that the symmetrically reactive active colloids undergo changes in their trajectory direction. For the active Janus colloids discussed in this thesis, the changes in their trajectories arise from Brownian rotation of the colloid as discussed in chapter 1, as the propulsive vector is relative to the orientation of the active hemisphere[13]. For the fully coated, symmetrical Kisker beads observed in this work, the change in trajectory over time is in itself an interesting observation as this implies a relative orientation to the colloids. The rotational diffusion time (τ_R), for the kisker colloids with grown platinum layer which displayed enhanced motion in 10 % hydrogen peroxide, was calculated from the gradient of the MSD as previously used in section chapter 5 and are presented in Figure 6.22. The experimental τ_R value of approximately 30 radians^2 s^{-1} far lower than the Stokes-Einstein rotational diffusion time for a colloid of 5 µm diameter of 95.4 radians^2 s^{-1}. However this is not out of line with previously reported τ_R values being lower for self-phoretic colloids than the natural rotational diffusion of the colloid[14]. Howse *et al.* discussed the reduction in rotational diffusion in terms of imperfections in the active layer producing a small angular velocity. Unlike in the findings by Howse *et al*. and the findings reported in this thesis in chapter 5 where the τ_R value is inversely correlated with velocity, the τ_R value here does not significantly change for the symmetrically reactive colloids, but does seemingly reduce for the masked colloids for the highest velocity recorded only.

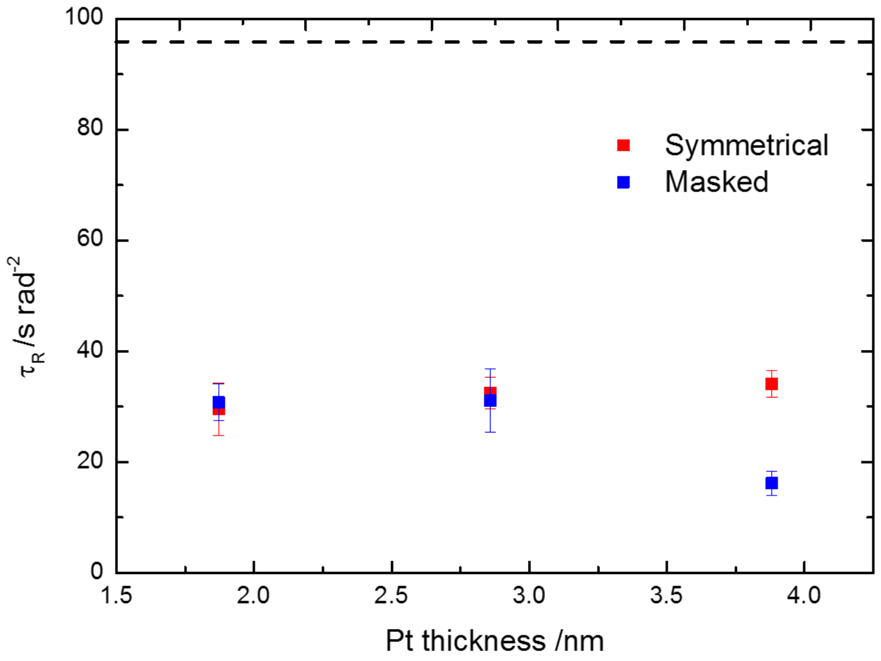

Figure 6.22. Rotational diffusion times for the symmetrical and masked Kisker colloids with grown platinum layer. The theoretical value is highlighted by a black dashed line at 95.4 radians^2 per seconds.

6.4 Conclusions

Colloids coated in platinum by sputter deposition have catalytically active sections greater than the hemispherical 50% coverage deposited by e-beam evaporation. The deposition of platinum on the underside, out of the line of sight displays a diminishing thickness gradient towards 0 nm at the interface between the colloid and the supporting substrate. An unexpected spike in platinum thickness is found around the base of the bead, likely due to an unusual diffusion pattern of the sputtered metal atoms. Despite such a build-up in platinum on the opposing side of the bead no effect on the velocity could be definitively stated for the platinum coverage. Rather the roughness of the platinum had the strongest effect on the velocity. These results do not support the theoretical work stated by Kreissl *et al.* where a higher percentage coverage of the active layer would lead to a decrease in the efficiency of the active colloid[1].

In the study of the fully platinum coated, symmetrically active Kisker supplied colloids, displayed propulsive enhanced motion going against the theoretical models claiming that enhanced motion either could not occur, or that could only occur on extremely small time scales[1][5].

An interesting facet of the symmetrically active colloids is their rotational diffusion. For colloids with no morphological distinction between ‘forward’ and ‘backward’ both their persistence of motion and ability to turn is intriguing. While theoretical models may allow for spontaneous symmetry breaking in the fluid flow around isotopically active colloids, it does not appear to explain the propensity for symmetrically reactive colloids to turn in the same manner as Janus active colloids. This turning indicates a sense of defined colloidal orientation. What defines this orientation is unknown. The effect of rotation of the colloid has not been explored by theories predicting motion for symmetrical catalyst distribution and could be a course for future experiments in collaboration with theoreticians[6].

Furthermore, masking one hemisphere with inert and non-conductive SiO_2, to restore asymmetry, resulted only in a significant decrease in velocity. This again does not support the notion of efficiency stated by Kreissl *et al.*[1].

It should be stated that although this work does not support the idea of smaller active layer coverage being more efficient, nor does it rule it out. The increase in activity from greater coverage could simply outweigh any increased efficiency from reducing the active layer coverage.

Future work in this area would be to develop methods to better control the surface coverage of the active layer. In particular, producing smaller patches than hemispherical coverages.

Finally, the idea that asymmetry is not required for producing self-phoretic particles, in fact could simplify the synthesis of future devices without need for masking or directional coating to produced Janus functionality.

6.5 References

[1] P. Kreissl, C. Holm, and J. de Graaf, “The Efficiency of Self-Phoretic Propulsion Mechanisms with Surface Reaction Heterogeneity,” *J. Chem. Phys*. pp., 1–10, 2016.

[2] S. Michelin and E. Lauga, “Autophoretic locomotion from geometric asymmetry,” *Eur. Phys. J. E. Soft Matter*, vol. 38, no. 2, p. 91, 2015.

[3] N. Yoshinaga, “Spontaneous motion and deformation of a self-propelled droplet,” *Phys. Rev. E - Stat. Nonlinear, Soft Matter Phys.*, vol. 89, no. 1, 2014.

[4] E. Yariv, “Wall-induced self-diffusiophoresis of active isotropic colloids,” *Phys. Rev. Fluids*, vol. 1, no. 3, p. 032101, 2016.

[5] R. Golestanian, “Anomalous diffusion of symmetric and asymmetric active colloids,” *Phys. Rev. Lett.*, vol. 102, no. 18, pp. 1–4, 2009.

[6] S. Michelin, E. Lauga, and D. Bartolo, “Spontaneous autophoretic motion of isotropic particles,” *Phys. Fluids*, vol. 25, no. 6, pp. 1–7, 2013.

[7] S. Swann, “Magnetron sputtering,” *Phys. Technol.*, vol. 19, no. 6, pp. 67–75, 1988.

[8] and P. M. C. J.-Z. Xue, E. Herbolzheimer, M. A. Rutgers, W. B. Russel, “Diffusion, Dispersion, and Settling of Hard Spheres,” vol. 69, no. 11, pp. 1715–1718, 1992.

[9] W. F. Paxton, P. T. Baker, T. R. Kline, Y. Wang, T. E. Mallouk, and A. Sen, “Catalytically induced electrokinetics for motors and micropumps,” *J. Am. Chem. Soc.*, vol. 128, no. 46, pp. 14881–14888, 2006.

[10] S. Ebbens, D. A. Gregory, G. Dunderdale, J. R. Howse, Y. Ibrahim, T. B. Liverpool, and R. Golestanian, “Electrokinetic Effects in Catalytic Pt-Insulator Janus Swimmers,” *EPL.*, pp. 1–5, 2013.

[11] U. Choudhury, L. Soler, J. G. Gibbs, S. Sanchez, and P. Fischer, “Surface roughness-induced speed increase for active Janus micromotors.,” *Chem. Commun.*, vol. 51, no. 41, pp. 8660–3, 2015.

[12] G. Dunderdale, S. Ebbens, P. Fairclough, and J. Howse, “Importance of particle tracking and calculating the mean-squared displacement in distinguishing nanopropulsion from other processes.,” *Langmuir*, vol. 28, no. 30, pp. 10997–1006, Jul. 2012.

[13] S. J. Ebbens and J. R. Howse, “Direct Observation of the Direction of Motion for Spherical Catalytic Swimmers,” *Langmuir*, vol. 27, no. 20, pp. 12293–12296, 2011.

[14] J. Howse, R. Jones, A. Ryan, T. Gough, R. Vafabakhsh, and R. Golestanian, “Self-Motile Colloidal Particles: From Directed Propulsion to Random Walk,” *Phys. Rev. Lett.*, vol. 99, no. 4, p. 048102, Jul. 2007.

Chapter 7:

Conclusions and future work.

Chapter 7 - Conclusions and future work.

7.1 Overview

This thesis has been centrally focused on micron-scale, spherical, active Janus colloids. However within this field the work presented here has been broad, spanning investigations into the phoretic mechanism (chapter 3 and chapter 6), trajectory control (chapter 4) and new synthesis route (chapter 5) for active Janus colloids. For this reason it is helpful to break the conclusions down by their respective chapter.

A key component in pushing the field of active Janus colloids from interesting to useful will be the ability to build in environmentally responsive changes to their trajectories allowing them to perform

7.2 Influence of the inactive hemisphere on the velocity of active Janus colloids.

7.2.1 Conclusions

On the investigation on the Influence of the inactive hemisphere on the velocity of active Janus colloids, a weak positive correlation between increasing hydrophobicity and increasing velocity was found. No correlation was found between zeta potential and velocity. These results indicate that interaction between the non-catalytic face of the Janus colloid and the fluid plays a role in the phoretic mechanism.

7.2.2 Future work

Velocity modulation by the hydrophobicity of the non-catalytic face could be exploited. Ionisable surface functionality has been demonstrated to change the hydrophobicity of the surface with pH [1]. As the velocity has been shown to be modulated by the hydrophobicity, surface responsive groups could give rise to pH dependant velocity modulation.

7.3 Glancing angle deposition to control active layer shape

7.3.1 Conclusions

Chapter 4 demonstrated that through control of the active layer shape, control over the trajectory of active Janus colloids is possible. By breaking the radial symmetry of the active layer an angular velocity is introduced, the magnitude of which is proportional to the degree of change in the active layer. This method offers a high level of control over the inbuilt ratio between propulsive and angular velocity.

7.3.2 Future work

Adding additional angular velocity in the trajectories by unbalancing the force could also be achieved by means of a second catalytically reactive patch, deposited asymmetrically with respect to the first catalytic patch. If the second catalyst is only reactive with certain species or under certain conditions then a responsive angular velocity would be possible and could switch the active colloids from propulsive to spinning trajectories.

Active propulsion has been demonstrated through reaction between photocatalytic colloids and their aqueous environment[2]. Considering photocatalysis has been shown to be sufficiently reactive to produce motion, adding photocatalytic material asymmetrically with respect to the platinum active layer could potentially allow for a photo-induced angular velocity.

Another route to switchable angular velocity in the trajectories would be to add a second catalyst asymmetrically with respect to the platinum reactive layer. The second catalyst would have to be unreactive with respect to hydrogen peroxide and sufficiently reactive with respect to a second dissolved ‘fuel’.

7.4 Solution based synthesis of active Janus colloids

7.4.1 Conclusions

It has been shown in this work that active Janus colloids can be fabricated in a scalable solution based synthesis through Pickering emulsion masking. Active Janus colloids produced through solution based synthesis are comparative in motion to those produced through physical vapour deposition. In morphology, active Janus colloids prepared through solution based fabrication have a higher coverage of deposited catalyst. Solution prepared active Janus colloids exhibited higher velocities for the respective reaction rates than for the active colloids prepared through physical vapour deposition.

The high intolerance to dissolved ionic species is still present for active colloids prepared by solution based fabrication. From this we can conclude either that phoretic mechanism is electrophoretic but does not work as speculated by Ebbens *et al*. or that the mechanism is not electrophoretic and salt is having an inhibitory effect in an unknown mechanism[3].

7.4.2 Future work

The scaling up of active Janus colloid synthesis would allow high volume fraction work to be studied. Mathematical models have predicted self-organisation and clustering effects for solutions containing high volume fraction active colloids[4].

The solution based fabrication could also allow a route for deposition of other catalytic species including organic-metal complexs, which cannot be deposited through physical vapour deposition. Removing the reliance on platinum would represent a large step forwards in practical applications due to cost.

Further investigation into the effect of salt on the phoretic mechanism is needed. Overcoming the sensitivity to dissolved ionic species would represent a huge breakthrough, allowing active colloids to be utilised in wider range of applications, such as *in vivo*.

7.5 Influence of the active layer shape and coverage on the motion of active Janus colloids.

7.5.1 Conclusions

Symmetrically changing the distribution of platinum on active Janus colloids did not result in any distinct change in velocity. The surface roughness of the active layer was found to be the dominant effect on active colloid velocity.

Furthermore, propulsive motion was found in colloids fully coated in platinum, which had fully symmetrical reactivity. Masking one hemisphere with an inert material to restore the Janus activity only resulted in a reduction of the velocity.

It is concluded from these results that the extent of surface coverage of the catalytically active material has little effect and that Janus functionality does not appear to be necessity.

7.5.2 Future work.

Fully symmetrically active colloids made a smooth surface and no imperfections are required to make a firm conclusion as to whether asymmetry is required to produce enhanced motion in active colloids .The symmetrically active colloids presented in chapter 6 were prepared by a solution based synthesis. It could be argued that the rougher surfaces could inherently have heterogeneous activity leading to the required asymmetry. To fully support the arguments made in Chapter 6, that fully symmetrically active colloids are capable of displaying enhanced motion with sufficiently high reactivity, a fabrication method that produces smooth surfaces such as PVD is required. As PVD is an inherently directional technique that requires a substrate to support colloids to be coated, fabrication of uniform beads represents a challenge. In future work, methods reported to create bi-metallic Janus colloids by PVD through inverting the colloids after coating, could be modified to create uniformly coated, symmetrically active colloids [5]

7.6 References

[1] F. Rios and S. N. Smirnov, “pH Valve Based on Hydrophobicity Switching,” *Chem. Mater.*, vol. 23, no. 16, pp. 3601–3605, Aug. 2011.

[2] Y. Hong, M. Diaz, U. M. Córdova-Fteueroa, and A. Sen, “Light-driven titanium-dioxide-based reversible microfireworks and micromotor/micropump systems,” *Adv. Funct. Mater.*, vol. 20, no. 10, pp. 1568–1576, 2010.

[3] S. Ebbens, D. A. Gregory, G. Dunderdale, J. R. Howse, Y. Ibrahim, T. B. Liverpool, and R. Golestanian, “Electrokinetic Effects in Catalytic Pt-Insulator Janus Swimmers,” pp. 1–5, 2013.

[4] S. Saha, R. Golestanian, and S. Ramaswamy, “Clusters, asters, and collective oscillations in chemotactic colloids,” *Phys. Rev. E - Stat. Nonlinear, Soft Matter Phys.*, vol. 89, pp. 1–7, 2014.

[5] S. Ye and R. L. Carroll, “Design and fabrication of bimetallic colloidal ‘Janus’ particles.,” *ACS Appl. Mater. Interfaces*, vol. 2, no. 3, pp. 616–20, Mar. 2010.